5-1-2019

Two dimensional nano-structures

Herath Mudiyanselage Herath Mudiyanselage

TWO DIMENSIONAL NANO-STRUCTURES

by

H. M. THAKSHILA M. HERATH

Under the Direction of Vadym M. Apalkov, PhD

ABSTRACT

The properties of a step-like defect on the surface of ultrathin topological insulator nanofilm have been studied. The reflectance of an electron from such a defect for different parameters of the nanofilm and the different parameters of the defect has been calculated. An electron incident on a steplike defect not only produces reflected and transmitted waves but also generates the modes, which are localized at the steplike defect. Such modes result in an enhancement of electron density at the defect by $\approx 60\%$. The magnitude of the enhancement depends on the parameters of the nanofilm and the height of the step and is the largest in the case of total electron reflection. Next, the quantum dots in 2D materials such as topological insulator nanofilm, germanene and phosphorene were introduced. In topological insulator, We introduce a quantum dot as a bump at a surface of nanofilm. Such quantum dot can localize an electron if the size of the dot is large enough, $\sim$ 5 nm. The other type of quantum dot is created in germanene. The band gap of buckled graphene-like materials such as germanene, depends on the external electric field. Then a specially design profile of electric field can produce trapping potential for electrons. Another type of quantum dot can be designed using phosphorene. Phosphorene itself has a band gap. By considering the piece

of cylindrical phosphorene layer, an electron can be confined. We study the energy spectra of such defined quantum dots. The intraband and interband optical transitions within the dots have also been studied. The effects of the temperature and the substrate modify the model parameters and should not change the results considerably.

INDEX WORDS: Topological Insulators, Silicene, Germanene, Black phosphorous, Phosphorene, Quantum dot, Nanofilm, Band gap, Spin-orbit coupling, Interband, Intraband, Step-like defects

NANO STRUCTURES OF 2D MATERIALS

by

H. M. THAKSHILA M. HERATH

A Dissertation Submitted in Partial Fulfillment of the Requirements for the Degree of

Doctor of Philosophy

in the College of Arts and Sciences

Georgia State University

2019

NANO STRUCTURES OF 2D MATERIALS

by

H M THAKSHILA M HERATH

Committee Chair:	Vadym Apalkov
Committee:	Gennady Cymbalyuk
	Unil Perera
	Douglas Gies
	Alexander Kozhanov

Electronic Version Approved:

Office of Graduate Studies
College of Arts and Sciences
Georgia State University
January 2019

To

my father, H M Ubayawardana Herath

and

my mother, K M Rani Herath

ACKNOWLEDGEMENTS

I would like to thank my adviser, Prof. Vadym Apalkov for his guidance and enormous support throughout this period. I would not have even think of doing this without his help. Also I am very thankful for Dr. Unil Perera for giving me valuable advice whenever sought. He never asks to make appointments whenever I want to get some advice. Moreover I thank and do appreciate all the members of the committee for their valuable time reading my dissertation and giving me their insightful comments and suggestions.

Also, in the last three years I have been working on a project in computational neuroscience. Dr. Gennady Cymbalyuk has been assisting and serving me as my co-adviser. Also, Dr. Suranga Edirisinghe is a collaborator in that project and helping me in learning and using high performance computing resources at Georgia State University and Open Science Grid. I am very thankful for Dr. Gennady Cymbalyuk and Dr. Suranga Edirisighe for their valuable time and support. We have still been working on that project and there is no component from that project in this thesis. However, due to that project I have gained many professional skills and personal skills, especially 'never give up'. We expect to have some outcomes in the future.

I thank Carola Butler for her support coordinating and assigning the laboratory classes. I also wish to thank all the faculty and staff of Physics and Astronomy Department at GSU for their constant support through out these years.

Also, I am very grateful for my parents for trusting me and letting me do everything as I wish. I would also like to thank all my teachers and friends who I met so far in my life. I would not come this far without any of you.

Again, I am deeply grateful for my adviser for giving me a peaceful, valuable and wonderful time during my PhD program. I cannot ask for a better adviser than him!

TABLE OF CONTENTS

LIST OF FIGURES

LIST OF ABBREVIATIONS

- QHS - Quantum Hall System
- QSH - Quantum Spin Hall
- QSHE - Quantum Spin Hall Effect
- TI - topological insulator
- 2DTI - two dimensional topological insulator
- QD - quantum dot
- CB - conduction band
- VB - valence band
- SOC - spin orbit coupling
- IB - interband
- BP - Black Phosphorus
- BTE - Boltzman transport equation

CHAPTER 1

INTRODUCTION

1.1 Overview

Discovery of new 2D materials has emerged thanks to graphene's exciting electronic, optical, thermal and mechanical properties. Subsequently, graphene-like materials such as silicene, germanene and phosphorene were discovered. Moreover ultrathin topological insulator nanofilm has been identified as another 2D material which has remarkable properties.

In this thesis, I study the energy spectra and optical properties of nano-structures in ultrathin TI nanofilms, graphene like-materials, and phosphorene monolayer. First a one-dimensional step-like defect on TI nanofilm is considered and the electron transport along the surface of TI nanofilm is studied. Then the energy spectra and optical transitions of a confined Dirac electron in TI nanofilm, graphene-like materials such as silicene and germanene and phosphorene are studied. To confine an electron in Dirac materials, a band gap needs to be opened. For TI nanofilms, such a gap can be opened through hybridization of the states at two opposite surfaces of the nanofilm. The band gap of graphene-like materials, such as silicene or germanene, can be tuned by applying an electric field perpendicular to silicene or germanene sheet. Monolayer or few layers of black phosphorus (BP) has an intrinsic band gap and it can be controlled with the thickness of the BP sheet. In the next section I discuss the general properties of quantum dots. Then the properties of TIs and TI nanofilms, silicene/germanene and black phosphorus are studied. In Chapter 2, the electron propagation along the step-like defect on TI nanofilm is considered. The results are published in Physical Review B [1]. In Chapters 3, 4, and 5 I discuss the electronic and optical properties of a confined Dirac electron in TI nanofilm, silicene/germanene and phosphorene quantum dots, respectively. The results in Chapters 3 and 4 are published in Journal of Physics : Condensed Matter [2, 3] respectively.

1.2 Quantum dots

Quantum dots are nanocrystals and often referred to as artificial atoms because the confining potential replaces the potential of a nucleus. Usually a quantum dot can trap 2-200 electrons and the dot size varies from 10nm to 100nm [4]. Unique properties of quantum dots are determined by their discrete energy spectrum, which can be tuned externally through the nature and the strength of the confinement potential [5]. Such zero dimensional systems show both specific electron transport with nonlinear features and controllable optical properties. The main interest in quantum dots is related to their potential for applications, ranging from novel lasers, light-emitting diodes, diode lasers, and photodetectors to quantum information processing.

In conventional semiconductor systems, quantum dots are introduced either by placing one nano-sized material into another material, e.g., by the Stranski-Krastanow growth technique, or by applying specially designed electrostatic confinement potential to low-dimensional systems. In both cases a confinement potential is introduced, which results in electron localization within the quantum dot region. The key concept here is to localize an electron through a confinement potential. Recently, a new type of quantum dots, graphene quantum dots [6–8] with electrostatic confinement potential, were considered. The electrons in graphene behave as massless Dirac fermions. In graphene quantum dots due to Klein paradox (Fig. 1.1), the electrons cannot be localized but can be only trapped for a long time [7]. The longest trapping time is realized in a confinement potential with smooth boundaries [8]. Such non-conventional behaviour of electrons in graphene is determined by their unique low-energy dispersion, which is gapless and relativistic, while the corresponding states are chiral [9, 10].

Other systems which have a dispersion law similar to graphene and corresponding localization properties are 3D topological insulators (TI) [11–17], Bi_xSb_{1-x}, Bi_2Te_3, Sb_2Te_3, and Bi_2Se_3 materials. The unique features of 3D TIs are gapless surface states with low-energy dispersion, which is similar to the dispersion law of a massless Dirac fermion. More details

will be presented in the next section.

Similar to graphene, the conventional quantum dots, which can localize an electron, cannot be realized in TIs through electrostatic confinement potential. To introduce a quantum dot in TI, one can consider a TI of a finite nano-scale size [18, 19] or introduce a gap in the dispersion law of coupled surface states of TI nanofilm [1, 20, 21]..Due to the finite extension of the surface states into the bulk, the surface states at two surfaces of TI nanofilm are coupled. Such coupling introduces a gap in the energy dispersion law. The magnitude of the gap depends on the film thickness. Thus the trapping potential in this case can be realized through modulation of the film thickness [2], which results in modulation of the band gap. The schematic illustration of quantum dot in TI nanofilm is shown in Fig. 1.2. Since TI nanofilm itself has a bandgap, an electron, confined in TI nanofilm QD, has no energy states in the continuum to escape from the quantum dot.

In Chapter 3, we consider a quantum dot in TI nanofilm. A quantum dot is introduced as a finite region of TI nanofilm with a larger thickness. Due to a gapped structure of the energy dispersion in TI nanofilm, such quantum dot can localize an electron. We consider only a single electron problem and for a single electron, both the energy spectra and the optical transitions within TI quantum dot were calculated.

Other Dirac 2D materials, in which the gap can be opened, are buckled graphene-like materials, such as silicene and germanene [22–30]. The main difference between silicene/germanene and graphene is that due to a larger radius of a Si/Ge atom compared to a C atom, the corresponding hexagon lattice in silicene/germnene has *buckled* structure [27] consisting of two sublattices that are displaced vertically by a finite distance $L_z \sim 0.5$ Å. As a result, silicene has large spin-orbit(SO) interaction, which opens up band gaps at the Dirac points (the band gap is $\approx 1.55 - 7.9$ meV for silicene [31, 32] and $\approx 24 - 93$ meV for germanene [31, 32]). For graphene, the corresponding spin-orbit-induced gap is very small, 25 μeV [33]. The buckled structure of silicene/germanene lattice allows the band gap to be tuned almost linearly by an external electric field applied perpendicular to the film [34]. Therefore in the case of silicene/germanene, application of nonuniform perpendicular electric field results in

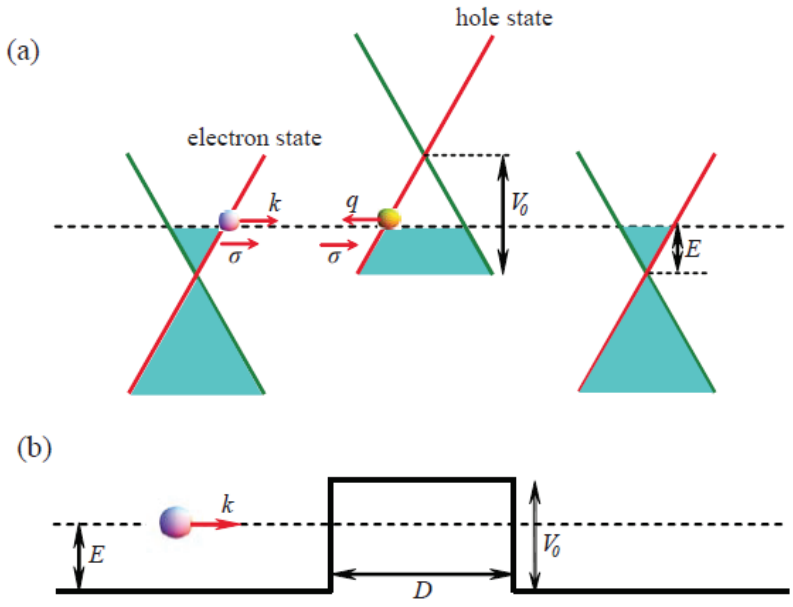

Figure (1.1) Tunnelling through potential barrier in graphene. The dashed line represents the Fermi energy level, E. Here $V_0(> E)$ is the height of the potential barrier. σ is the pseudospin. (a) The gapless linear dispersion of graphene is shown here. The blue filled areas indicate the occupied states. k and q are wave vectors of the electron outside and inside of the potential barrier respectively. (b) D is the width of the potential barrier. Outside the potential barrier, the electron is in the conduction band and inside it is in the valence band. The gapless states allows the electrons to be in any quantum state regardless of the energy of the electron. Due to that, electron penetrates through the potential barrier which is known as Klein tunneling. Figure is taken from Ref. [35]

a spatially dependent bandgap, which can produce electron localization.

In chapter 4, we study silicene/germanene quantum dots, which have cylindrical symmetry and are characterized by radius R. Such quantum dots are produced by a special distribution of external perpendicular electric field, which has different values in two regions: $\rho < R$ and $\rho > R$ where ρ is the radial distance. The results are published in Ref. [3]

1.3 Evolution of topological insulators

Conventionally solid state materials can be divided into conductors, insulators, and semiconductors. Such classification is mainly based on transport properties of solids. Finding

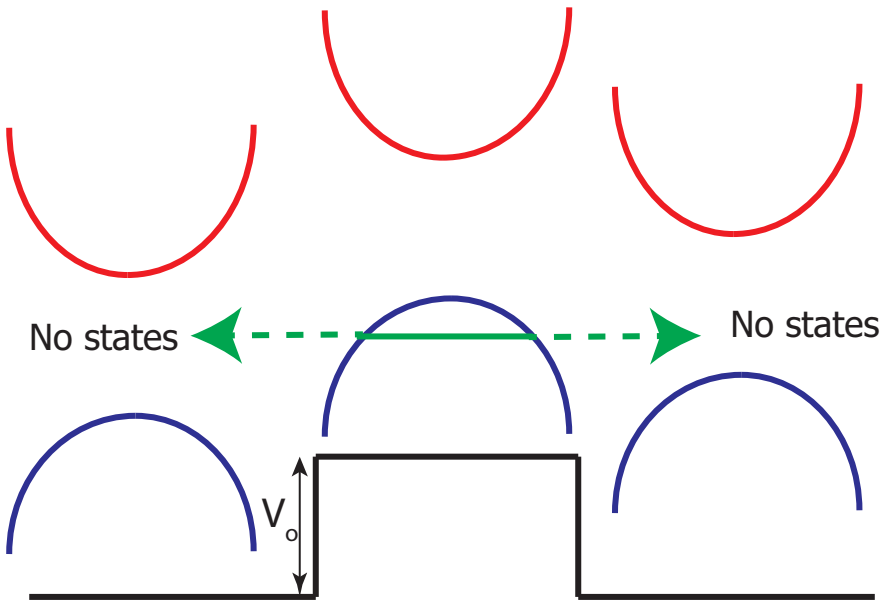

Figure (1.2) (color)Schematic illustration of quantum dot in topological insulator nanofilm. The red and blue color bands are conduction and valence band states respectively. TI nanofilm has gapped energy dispersion. V_0 is the potential barrier. Outside the potential barrier, the electron's energy is in the conduction band. Inside the potential barrier, the electron has no energy states to transit from valance to conduction due to the gapped dispersion. The electron is trapped inside the TI nanofilm with potential barrier.

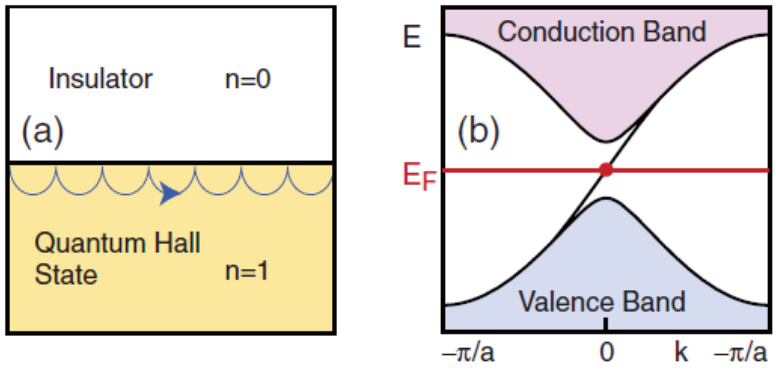

Figure (1.3) (a) Electron backs off from the edge and keeps moving in the same direction. The edge is in between the vacuum and the bulk which are insulators. (b) conduction band and valence band touch as edge state becomes metallic. Figure is taken from Ref. [38]

new quantum states of matter is one of the most attractive topics in condensed matter physics. Two-dimensional electron systems at low temperatures and high magnetic fields have metallic edge states and insulating bulk properties. This new quantum state was discovered in 1980 and is called the quantum Hall (QH) state [36]. In this QH state, electrons in the bulk follow quantized circular orbits due to the strong magnetic field. However, electrons on the edge cannot complete a circular orbit. They hit the boundary, reflect, and keep propagating along the edge. This is a drift motion, the direction of which depends on the direction of the magnetic field. The quantum Hall system(QHS) has gapless edge states and insulating bulk, see - Fig. 1.3. Only "one-way" edge state exists due to external magnetic field. The corresponding Hall conductivity is a multiple integer of e^2/h independent of material [37].

In Mathematics there is a branch called topology. If two objects can be smoothly transformed into each other through continuous deformation without changing their properties, they are called topologically equivalent, i.e., they are in the same topological class. For example, an orange and a ball are in one class as they both have zero number of holes or genus(g) and one object can be transformed into another one without changing the number of genus. Moreover, a doughnut and a coffee cup are in the same class. A doughnut can be

deformed into a coffee cup while preserving its property a number of genus, a single hole.

In quantum mechanics, the main object of topology is a Hamiltonian. The two quantum systems are called topologically equivalent if the Hamiltonian of the first system can be continuously transformed into the Hamiltonian of the second system without closing the bulk energy band gap. Similar to genus in Mathematics, topological classes in quantum mechanics can be distinguished by a topological invariant called the Chern invariant n. If the Chern invariant remains constant when the Hamiltonian is deformed, it is called topologically invariant. This is valid only for gapped materials such as insulators and gapped superconductors. Topological classes are protected by the symmetry of a system.

A new quantum state, which belongs to a new topological class of materials called 2D topological insulator (TI) or QSH state, has been theoretically predicted in 2006 [39] and experimentally observed in HgTe/CdTe quantum wells in 2007, base temperature $T < 30$mK [40]. 2DTI or QSH state is invariant under TR symmetry and has strong intrinsic spin-orbit coupling. Electrons with spin-up move in one direction and spin-down electrons move in the opposite direction and no backscattering is allowed - see Fig. 1.4. The QH system requires a magnetic field to create edge state while spin-orbit interaction plays the role of magnetic field in QSH. The energy dispersions of different quantum states are shown in Fig. 1.5. In QH system and QSH system, there is a 'one-way' edge current while the bulk material has a band gap. The difference in two systems is that QSH edge states are spin-split due to the spin-orbit coupling. This splitting is called the Rashba splitting.

The trivial insulator and 2D TI cannot be transformed into each other without closing a gap, i.e., they belong to two different topological classes. Let us consider the $HgTe/CdTe$ quantum well system. HgTe and CdTe are II-VI semiconductors which have strong spin-orbit interactions. In CdTe s-states on the group II atom contribute to the conduction band and p-states of VI atom contribute to the valence bands. In HgTe, p-states rise above s-states and 2D band inversion occurs. When HgTe is sandwiched in between CdTe layers, the 2D electron structure can be tuned with the quantum well thickness d - see Fig. 1.6. If $d < d_c = 6.3$nm the quantum well has the normal band structure. The band structure is inverted when

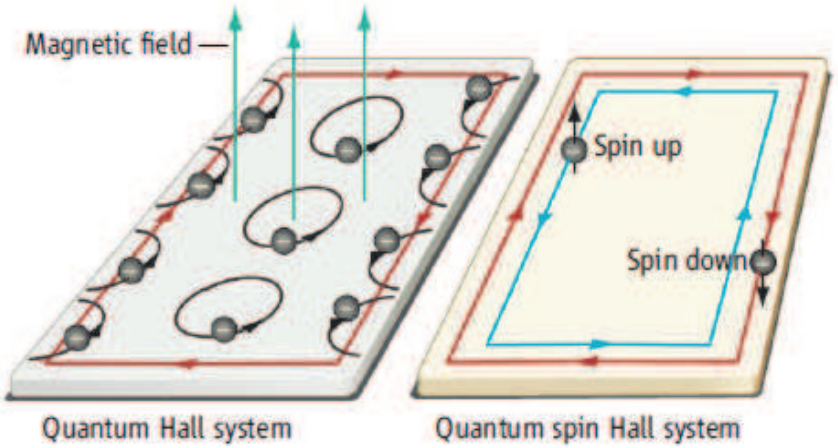

Figure (1.4) (a) Quantum Hall system : applied magnetic field makes electrons to flow around the edge of the material (b) Quantum Spin Hall system : The direction of the flow depends on the spin direction. Spin-orbit interaction induces spin dependent magnetic field here. Figure is taken from Ref. [41].

$d > d_c$. The band structure gets inverted as the well thickness increases. At $d = d_c$ the quantum well has a gapless band structure which indicates the phase transition from trivial insulator to quantum spin Hall insulator or 2D topological insulator. The experiments have shown that if $d > d_c$ the quantum hall system has helical edge states [39, 43]. The significant idea here is that a normal insulator becomes a topological insulator when the band structure is inverted, so that they do not belong to the same topological class.

Soon after the discovery of 2D TI, three-dimensional TIs were predicted theoretically and observed experimentally in Bi_xSb_{1-x}, Bi_2Te_3, Sb_2Te_3, and Bi_2Se_3 materials [11–17]. The unique feature of 3D TI is the gapless surface states with low-energy dispersion, which is similar to the dispersion law of massless Dirac fermions. Such a relativistic dispersion law has been observed experimentally by angle-resolved photoemission spectroscopy [13, 14, 16, 17, 44], oscillations in the local density of states [45], magnetoconductivity measurements[46], quantum oscillations of magnetization [47], Aharonov-Bohm oscillations in TI nanoribbons [48], Landau level spectroscopy [49, 50], optical processes [51, 52] and quantum Hall effect

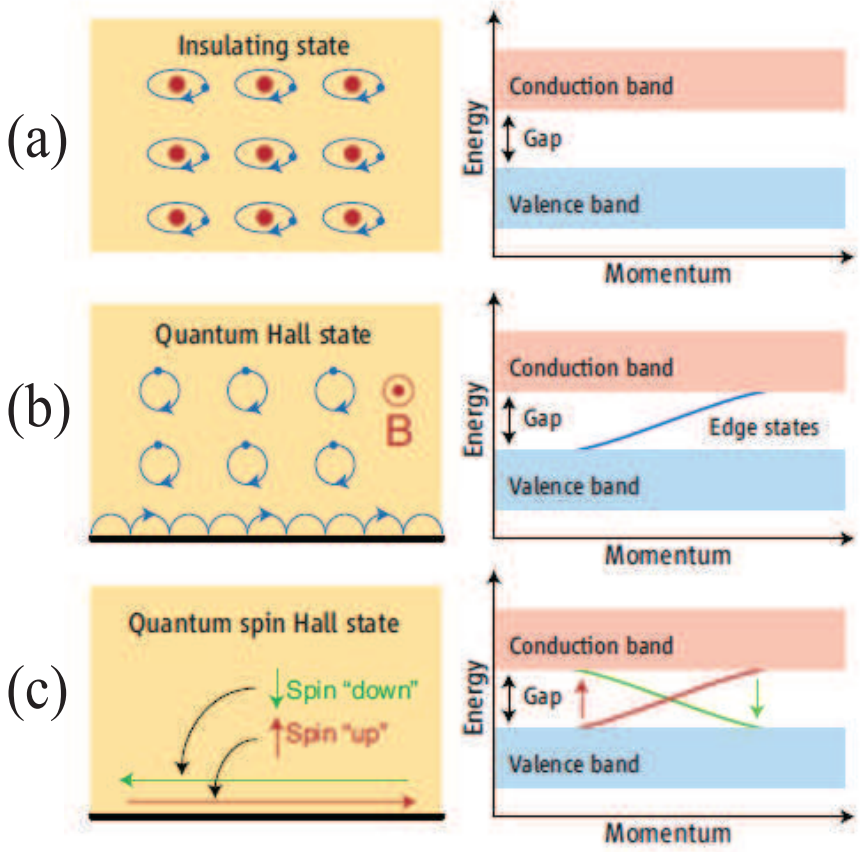

Figure (1.5) (a) Electrons are localized in the bulk of the material and there are gapped surface states. (b) Due to a magnetic field, electrons in the bulk move in quantized orbits. The electrons near the edge bounce off from the boundary as they are not able to complete circles. However they keep moving forward and result in edge states. (c) Due to spin degeneracy, electrons with spin up move in one direction and spin down electrons move in the opposite direction. Two edge states are gapless while the bulk has a finite gap. Figure is taken from Ref. [42].

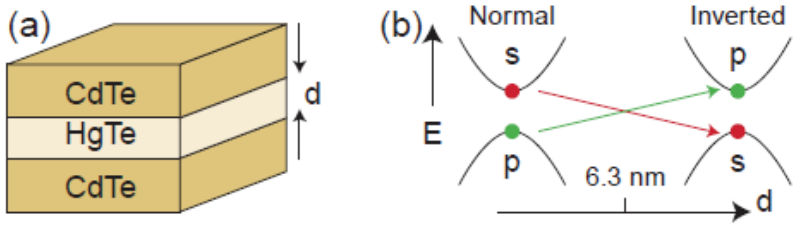

Figure (1.6) (a) HgTe quantum well structure. Here d is the thickness of the HgTe layer. (b) 2D band inversion is shown here as d increases. Figure is taken from Ref. [38].

[53].

Thus, topological insulators, 2D or 3D, should have strong spin-orbit interaction, which creates band inversion. The largest bulk gap of 3D TI is realized in Bi_2Se_3 TI with the bulk band gap of 0.3 eV. The crystal structure of well known real 3D topological insulator material, Bi_2Se_3, is shown in Fig. 1.7. The crystal structure has inversion symmetry I, three fold rotation symmetry C_3 along the z-axis and time-reversal symmetry T. There are five atoms in a unit cell. Five-atom layers stack on top of each other, and this combined layer is called a quintuple layer. A quintuple layer has two Bi layers, two Se layers and another Se layer which acts as an inversion center. Though there is a weak interaction between two quintuple layers, there is a strong SO coupling within a single quintuple layer. This strong SO coupling can invert bands near the Γ point which makes this material a topological insulator.

The growing interest in 3D TI systems is related to the unique relativistic massless energy dispersion law of their surface states. The surface states also have chiral spin texture, i.e., the direction of electron spin is correlated with direction of its momentum. The low energy dispersion is of relativistic Dirac type. In general TIs can have an odd number of Dirac cones, but in experimentally realized 3D TI systems, there is only one Dirac cone. Such a Dirac cone is described by an effective Hamiltonian of relativistic type.

The relativistic massless dispersion law is also realized in another system - graphene [54]. Although the low energy dispersions in TI and graphene are similar, there is a fundamental difference between these systems. Namely, TIs have only one Dirac cone (or odd number of Dirac cones), while graphene has two Dirac cones, corresponding to two valleys. The states of each Dirac cone in graphene are chiral, but chirality corresponds to pseudospin, not the real spin, while the states of TI are spin chiral, where the real electron spin is correlated with its momentum. Thus, each state in graphene has double spin degeneracy, whereas the states in TI have no spin degeneracy.

Another fundamental difference between graphene and TI is that the surface states in graphene are purely two-dimensional, whereas the surface states of TI are three-dimensional with finite spatial extension into the bulk of TI. The finite spatial width of the surface states

of TI brings additional features to TI systems. For example, for TI nanofilm of small thickness, the surface states at two boundaries of the nanofilm are coupled due to the 3D nature of TI surface states [20, 55, 56]. Such coupling of the states of two TI surfaces opens a gap in otherwise gapless surface relativistic dispersion, resulting in an energy dispersion similar to the dispersion of narrow-gap semiconductors. The value of the gap depends on the thickness of TI nanofilm. Studying surface states provides better understanding of TI nanofilm.

We consider Bi_2Se_3 TI thin film grown along z-direction. The atomic p orbitals of Bi($6s^26p^3$) and Se($4s^24p^4$) contribute to the Hamiltonian. Formation of the band structure of 3D TI is illustrated in Fig. 1.8 and can be explained as follows. (1) Coupling of Bi and Se layers makes Bi energy levels higher than Se energy levels due to the level repulsion. The p orbitals of Bi and Se are hybridized and result in new states $B_{x,y,z}$, $B'_{x,y,z}$, $S_{x,y,z}$, $S'_{x,y,z}$ and $SO^-_{x,y,z}$. (2) The bonding and anti-bonding states, $P1^{\pm}_{x,y,z}$ and $P2^{\pm}_{x,y,z}$ are created due to the inversion symmetry. (3) The crystal has a layered structure which results in energy splitting between p_z and $p_{x,y}$. (4) The coupling between spin and orbital angular momentum leads to crossing of the levels $P1^+_z$ and $P2^-_z$. It transforms the system into a topological insulator phase [57, 58]. So $P1^+_z,\uparrow(\downarrow)$ and $P2^-_z,\uparrow(\downarrow)$ are the closest energy levels to the Fermi level and are considered as the basis of the effective Hamiltonian. The corresponding basis states can be written as $[\varphi(A_1),0]^T$, $[0,\chi(-A_1)]^T$, $[\chi(A_1),0]^T$ and $[0,\varphi(-A_1)]^T$. With this basis states, we can write down the effective Hamiltonian for bulk Bi_2Se_3 following Ref. citeshan2010effective:

$$H(\mathbf{k}) = \epsilon_0(\mathbf{k})I_{4\times4} + \begin{bmatrix} \mathcal{M}(\mathbf{k}) & A_1k_z & 0 & A_2k_- \\ A_1k_z & -\mathcal{M}(\mathbf{k}) & A_2k_- & 0 \\ 0 & A_2k_+ & \mathcal{M}(\mathbf{k}) & -A_1k_z \\ A_2k_+ & 0 & -A_1k_z & -\mathcal{M}(\mathbf{k}), \end{bmatrix}, \tag{1.1}$$

where $I_{4\times4}$ is 4×4 unit matrix, $\epsilon_0(\mathbf{k}) = C + D_1k_z^2 + D_2k^2$, $\mathcal{M}(\mathbf{k}) = M - B_1k_z^2 - B_2k^2$, $k_\pm = k_x \pm ik_y$ and $k^2 = k_x^2 + k_y^2$. Here $\mathbf{k}$ is the finite wave vector. Model parameters can be found in Ref. [57] ; M = $0.28eV$, $A_1 = 2.2eV$Å, $A_2 = 4.1eV$Å, $B_1 = 10eV$Å^2,

$B_2 = 56.6eV\text{Å}^2$, $C = -0.0068eV$, $D_1 = 1.3eVmathrm\mathring{A}$, $D_2 = 19.6eVmathram\mathring{A}$.
We solve the eigenvalue problem following Ref. [21]

$$H(k, k_z)\psi = E\psi, \tag{1.2}$$

using the four component trial wave function $\psi = \psi_\lambda e^{\lambda z}$. The secular equation gives four solutions of $\lambda(E)$, $\pm\lambda_1$ and $\pm\lambda_2$. We label them as $\beta\lambda_\alpha(E)$ with $\alpha \in \{1, 2\}$ and $\beta \in \{+, -\}$.

$$\lambda_\alpha(E) = \left[-\frac{F}{2D_+D_-} + (-1)^{\alpha-1}\frac{\sqrt{R}}{2D_+D_-} \right]^{1/2}, \tag{1.3}$$

where

$$\begin{aligned}
F &= A_1^2 + D_+(E - L_1) + D_-(E - L_2), \\
R &= F^2 - 4D_+D_-[(E - L_1)(E - L_2) - A_2^2 k_+ k_-], \\
D_\pm &= D_1 \pm B_1, \\
L_1 &= C + M + (D_2 - B_2)k^2, \\
L_2 &= C - M + (D_2 + B_2)k^2.
\end{aligned}$$

Due to the double degeneracy each wave function can be written as

$$\psi_{\alpha\beta1} = \begin{bmatrix} D_+\lambda_\alpha^2 + L_2 + E \\ -iA_1(\beta\lambda_\alpha) \\ 0 \\ A_2 k_+ \end{bmatrix}, \tag{1.4}$$

$$\psi_{\alpha\beta2} = \begin{bmatrix} A_2 k_- \\ 0 \\ iA_1(\beta\lambda_\alpha) \\ D_-\lambda_\alpha^2 - L_1 + E \end{bmatrix}. \tag{1.5}$$

The general wave function is a linear combination of these eight functions

$$\Psi(E,k,z)=\sum_{\alpha=1,2}\sum_{\beta=\pm\gamma}\sum_{\gamma=1,2}C_{\alpha\beta\gamma}\psi_{\alpha\beta\gamma}e^{\beta\lambda_\alpha z}, \tag{1.6}$$

where $C_{\alpha\beta\gamma}$ is the superposition coefficient. Using the semi infinite boundary conditions $\Psi(z=0)=0$ and $\Psi(z\to+\infty)=0$, the energy dispersion of the surface states can be written as

$$E_\pm=C+\frac{D_1M}{B_1}\pm A_2\sqrt{1-(\frac{D_1}{B_1})^2}k+(D_2-\frac{B_2D_1}{B_1})k^2. \tag{1.7}$$

The Fermi velocity near the Γ point is,

$$v_F=\frac{1}{\hbar}\frac{dE}{dk} \tag{1.8}$$

$$=(A_2/\hbar)\sqrt{1-(D_1/B_1)^2}. \tag{1.9}$$

For real roots $\lambda_{1,2}$, the edge states decay near the surface ($z=0$) and the decay length is of the order of the characteristic length $1/\lambda_{1,2}$. For a film of finite thickness, if the thickness is $\sim 1/\lambda_{1,2}$, then two states at opposite surfaces are coupled and a finite energy gap is opened. If $\lambda_{1,2}$ is real, the gap $\Delta=E_+-E_-$ at the Dirac point can be approximated by

$$\Delta\simeq\frac{4|A_1D_+D_-M|}{\sqrt{B_1^3(A_1^2B_1+4D_+D_-M)}}e^{-\lambda_1L}, \tag{1.10}$$

with the finite-thickness boundary conditions $\Psi(z=\pm L/2)=0$ where two boundaries are located at $z=L/2$ and $z=-L/2$. If $\lambda_{1,2}$ are complex conjugates, then the gap can be written as [21]

$$\Delta\simeq\frac{8|A_1D_+D_-M|}{\sqrt{-B_1^3(A_1^2B_1+4D_+D_-M)}}e^{-aL}\sin bL, \tag{1.11}$$

where $\lambda_\pm=a\pm ib$ and

$$a\simeq\frac{A_1}{2\sqrt{-D_+D_-}}, \tag{1.12}$$

$$b\simeq\sqrt{\frac{M}{B_1}+\frac{A_1^2}{4D_+D_-}}. \tag{1.13}$$

The energy band gap decays exponentially as a function of the thickness of TI film. If the thickness of the nanofilm is small, i.e., $L \ll 1/\lambda$, then

$$\tanh(\frac{\lambda_1 L}{2}) = 0 \Longrightarrow \lambda_1 = i\frac{\pi}{L}, \tag{1.14}$$

and

$$\mathcal{H} = D_1\frac{\pi^2}{L^2} + D_2\frac{\hat{p}^2}{\hbar^2} + \frac{A_2}{\hbar}(\hat{\sigma}_x\hat{p}_y - \hat{\sigma}_y\hat{p}_x) + (B_1\frac{\pi^2}{L^2} + B_2\frac{\hat{p}^2}{\hbar^2})\hat{\tau}_z \otimes \hat{\sigma}_z. \tag{1.15}$$

where $\hat{\sigma}_i$ $(i = x, y, z)$ are Pauli matrices corresponding to spin degrees of freedom, and $\hat{\tau}_z(= \pm 1)$ is the Pauli matrix corresponding to electron pseudospin. We use this effective continuous Hamiltonian in Chapter 2.

In Chapter 2, we introduce the step-like defect by changing the thickness of the nanofilm. The thickness of the film changes the energy band gap. We study how electron reflectance and transmittance depend on the parameters of the step-like defect and properties of TI nanofilm. The results are published in Ref. [1]

1.4 Graphene like materials : Silicene/Germanene

Graphene is a monolayer of Carbon(C) atoms. The unique properties of graphene lead scientists to study other elements in the same group of periodic table. As a result, other monolayer materials such as Silicene and Germanene have been discovered [22–27]. Silicene and Germanene are single layers of Si and Ge atoms, respectively. The main difference between silicene/germanene and graphene is that due to a larger radius of a Si/Ge atom compared to a C atom, the corresponding hexagonal lattice in silicene/germanene has a *buckled* structure [27], consisting of two sublattices that are displaced vertically by a finite distance $l \sim 0.5$ Å Fig. 1.10. As a result, silicene has a large spin-orbit interaction, which opens up a band gap at the Dirac points ($\Delta_{\text{so}} \approx 1.55 - 7.9$ meV for silicene and $\Delta_{\text{so}} \approx 24 - 93$ meV for germanene [31, 32]). For graphene, the corresponding spin-orbit-induced gap is very small, 25 μeV [33]. This buckled nature brings interesting electronic properties and many attractive applications. Silicon based electronic devices are everywhere and it is convenient

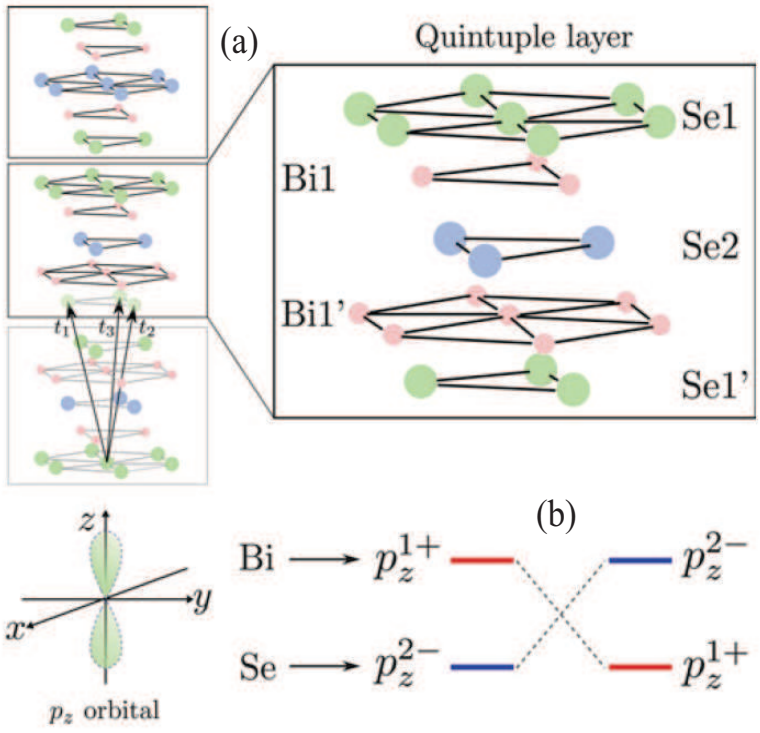

Figure (1.7) (a) Crystal structure of Bi_2Se_3 topological insulator. The inset shows the enlarged version of an quintuple layer. (b) Band inversion of Bi and Se atoms. Figure is copied from [59].

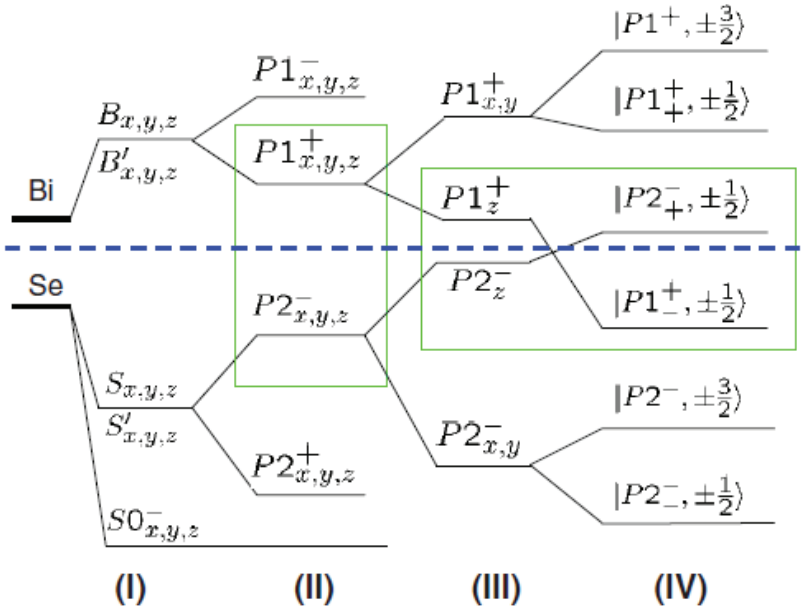

Figure (1.8) Band structure formation of Bi_2Se_3. (I) Coupling of Bi and Se layers. (II) Creation of bonding and anti-bonding states (III) Energy splitting between p orbitals. (IV) Crossing of the levels due to spin orbit interaction. Figure is copied from Ref. [58].

to incorporate silicene/germanene into current devices and to create new spintronic devices. The growth temperature for silicene on a Ag(1 1 1) surface ranges from 220 to 260°C [60]. Germanene can be grown on Au(1 1 1) at ∼200°C [29].

The lattice geometry of low-buckled monolayers of Silicene and Germanene is shown in Fig. 1.9. The low-buckled structure with sp^3-like hybridization is stable.

Silicene/Germanene are expected to be topological insulators as they have strong intrinsic spin-orbit coupling. Additionally these materials have properties similar to graphene as they reside in the same group IV. First-principle calculations demonstrated QSHE in Silicene/Germanene and showed a gap opening at the Dirac points due to spin-orbit coupling [61].

The low energy effective Hamiltonian with SOC of planar silicene at the Dirac point K has the following form

$$H_{eff}^{[K]} \approx \begin{pmatrix} -\xi\sigma_z & v_F\big(k_x + ik_y\big) \\ v_F\big(k_x - ik_y\big) & \xi\sigma_z \end{pmatrix}, \tag{1.16}$$

where v_F is the Fermi velocity near the Dirac point and σ_z is the Pauli matrix. The effective SOC ξ for the planar silicene is [61]

$$\xi \approx 2\xi_0^2|\Delta_\epsilon|/\big(9V_{sp\sigma}^2\big),$$

where Δ_ϵ is the energy difference between the $3s$ and $3p$ orbitals, ξ_0 is half the intrinsic spin-orbit coupling, and $V_{sp\sigma}$ is the parameter that corresponds to the σ bond. The σ bond is created by the $3s$ and $3p$ orbits. The energy spectrum can be obtained from Eq. (1.16) as

$$E(\overrightarrow{k}) = \pm\sqrt{(v_F k)^2 + \xi^2}. \tag{1.17}$$

The energy gap is 2ξ at the Dirac points. Due to its fascinating buckled structure, the charge will be transferred from one sub-lattice to the other sub-lattice and will open the band gap. By applying an electric field normal to the silicene/germanene sheet the band

gap can be controlled. When we apply electric field, E_z normal to silicene/germanene sheet, the low-energy effective Hamiltonian is

$$H_\eta = \hbar v_F(k_x\tau_x - \eta k_y\tau_y) + \eta\tau_z h_{11} + lE_z\tau_z, \tag{1.18}$$

where

$$h_{11} = -\lambda_{SO}\sigma_z - a\lambda_R(k_y\sigma_x - \eta k_x\sigma_y). \tag{1.19}$$

$v_F = \frac{\sqrt{3}}{2}at = 5.5 \times 10^5 \mathrm{ms}^{-1}$ is the Fermi velocity, $a = 3.86$ Åis the lattice constant of the sublattice and τ_a is the Pauli matrix corresponding to pseudospin. The Hamiltonian (1.18) will be discussed more in Chapter 4. The energy dispersion corresponding to the Hamiltonian (1.18) is

$$\varepsilon_\eta = \pm\sqrt{(\hbar v_F k)^2 + (lE_z - s\sqrt{\lambda_{SO}^2 + (a\lambda_R k)^2})^2},$$

where $s = \eta s_z$ and $s_z = \pm 1$ is the electron spin and $\eta = \pm 1$ corresponds to the K or K' Dirac points. The energy band gap at the Dirac points is

$$\Delta(E_z) = 2|lE_z - \eta s_z \lambda_{SO}|. \tag{1.20}$$

According to Eq. (1.20) the gap closes at $E_z = \eta s_z E_c$ where $E_c = \lambda_{SO}/l$. At the critical electric field E_c, the gap closes and silicene becomes semimetal. Elsewhere the gap is opened and silicene is an insulator. If $|E_z| < E_c$ it is a topological insulator, while if $|E_z| > E_c$, silicene is a band insulator. Fig. 1.10 shows the change of the band gap as electric field increases. Therefore in the case of silicene/germanene, application of a nonuniform perpendicular electric field results in a spatially dependent bandgap. This property can be used to design silicene-based quantum dots.

In Chapter 4, we study silicene/germanene quantum dots, which have cylindrical symmetry. Such quantum dots are created by the spatial distribution of an external perpendicular electric field, which has different values in two regions: $\rho < R$ and $\rho > R$ where ρ is the radial distance and R is the radius of the quantum dot. We study both energy spectra and

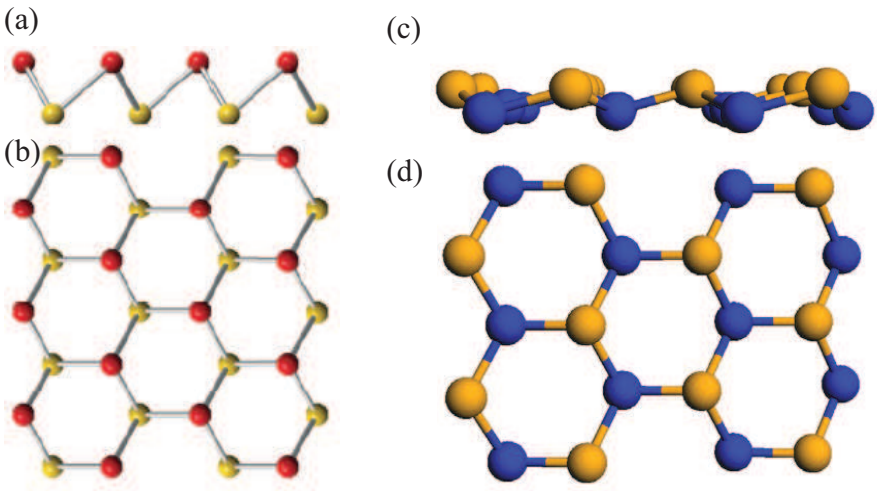

Figure (1.9) Crystal structure of low-buckled Silicene and Germanene. (a),(b) The side view and top view of Silicene. Atoms of two sublattices are denoted by red and yellow color.(c),(d) The side and top view of Ge. Yellow and blue color atoms are used to represent atoms in two sublattices. Figures are taken from Ref. [61, 62].

optical transitions of such silicene/germanene quantum dots. The results are published in Ref. [3].

1.5 Black Phosphorous

A well known phosphorus allotrope is white phosphorus (WP), P_4. The molecule has a tetrahedron structure with six single bonds and it has sp^3 hybridization. Each atom has 3 bonds with its neighbors. White phosphorus is not a stable material. When WP undergoes high pressure, it forms a tripod shape by breaking three bonds in P_4. Instead of becoming a fully flat layer, it has a puckered surface due to sp^3 hybridization. It is the most stable phosphorus allotrope which is called black phosphorus (BP). The structure of monolayer black phosphorus is shown in Fig. 1.11. Due to the puckered honeycomb structure, each phosphorene layer consists of two atomic layers which are separated by 2.244Åvertically. In BP the puckered layers are stacked on top of each other and stay together by weak van der Waals interactions. Phosphorene has two different orientations, namely "armchair" and

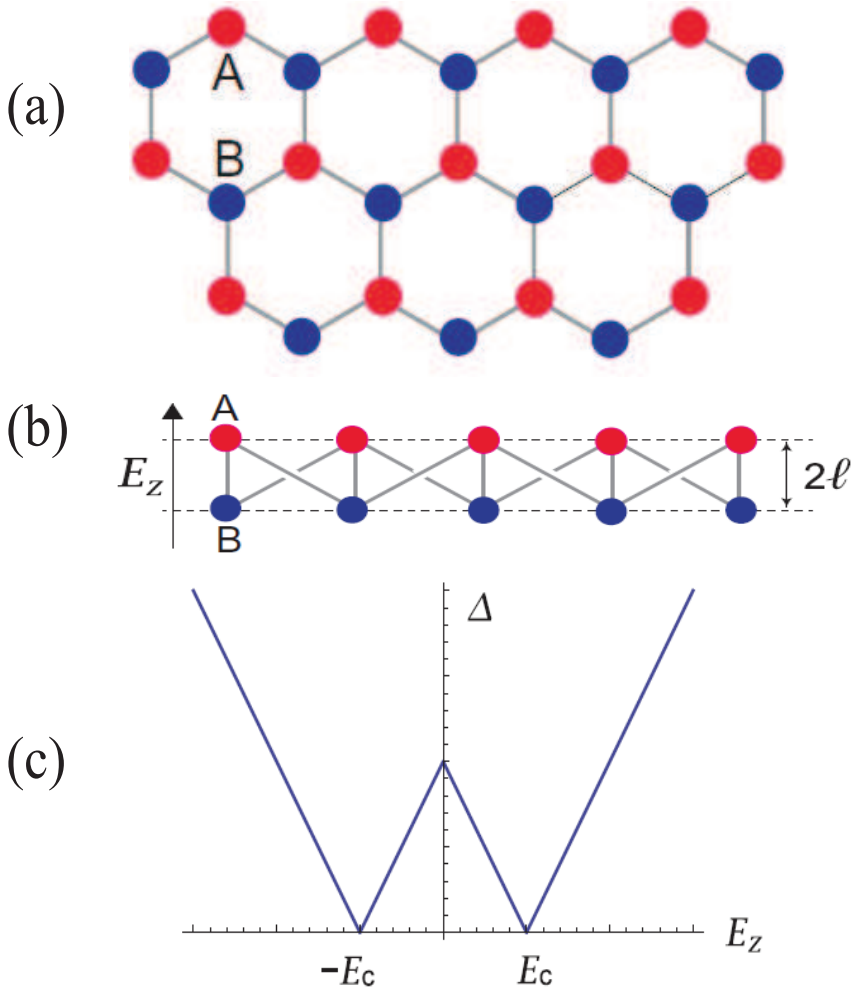

Figure (1.10) (a),(b) Top and side view of Silicene structure. A and B atoms are on two sublattices which separate by a perpendicular distance 2l. Electric field E_z is applied perpendicular to the sheet (c) The band gap Δ as a function of E_z. As E_z increases topological phase transition occurs between topological insulating phase to band insulating mode. Figure is taken from [34]

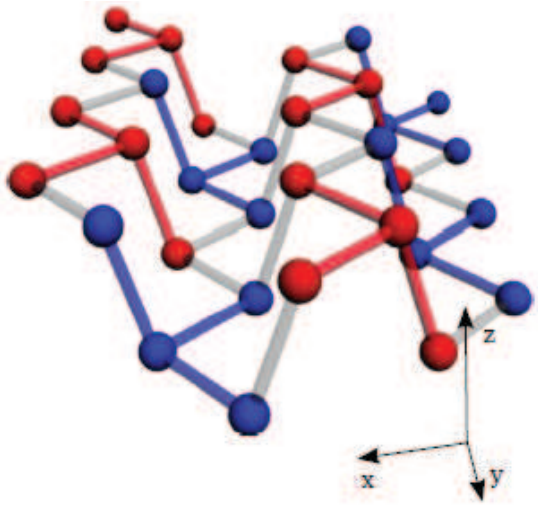

Figure (1.11) (Color) The 3D view of monolayer lattice structure of black phosphorous. A single layer consists of two sub lattices. Figure is copied from [69].

"zigzag" on two sides of the structure - see Fig. 1.12. Due to the different orientations, BP has highly anisotropic properties. BP has different Young's modulus and ultimate strain values for the armchair direction and zig-zag directions [63]. According to first principle calculations, Young's modulus along the armchair direction is 21.9N.m^{-1} while it is 56.3N.m^{-1} for the zig-zag direction. By solving the phonon Boltzman transport equation (BTE), the thermal conductivity at 300 K is $30.15\text{Wm}^{-1}\text{K}^{-1}$ in the zigzag direction and $13.65\text{Wm}^{-1}\text{K}^{-1}$ in the armchair direction [64]. Similar to graphene, the mechanical exfoliation method can be used to prepare a single to few BP layers [65–68]. Phosphorene is a 2D semiconcuctor with a finite band gap, while graphene is a semi-metal with zero band gap.

A monolayer BP has a gap of $1.5-2$ eV around the Γ point which is greater than the gap of 0.3 eV of bulk BP. This gap depends on the thickness of the BP layer [71]. In addition to the relatively large band gap, BP has other unique properties, such as carrier mobility up to $1000\text{cm}^2\text{V}^{-1}\text{s}^{-1}$. These properties can be tuned by the thickness of phosphorene. Moreover few-layer phosphorene can be used for field effect transistors at room temperature [67].

The effective low-energy Hamiltonian of phosphorene can be obtained from **k.p** theory

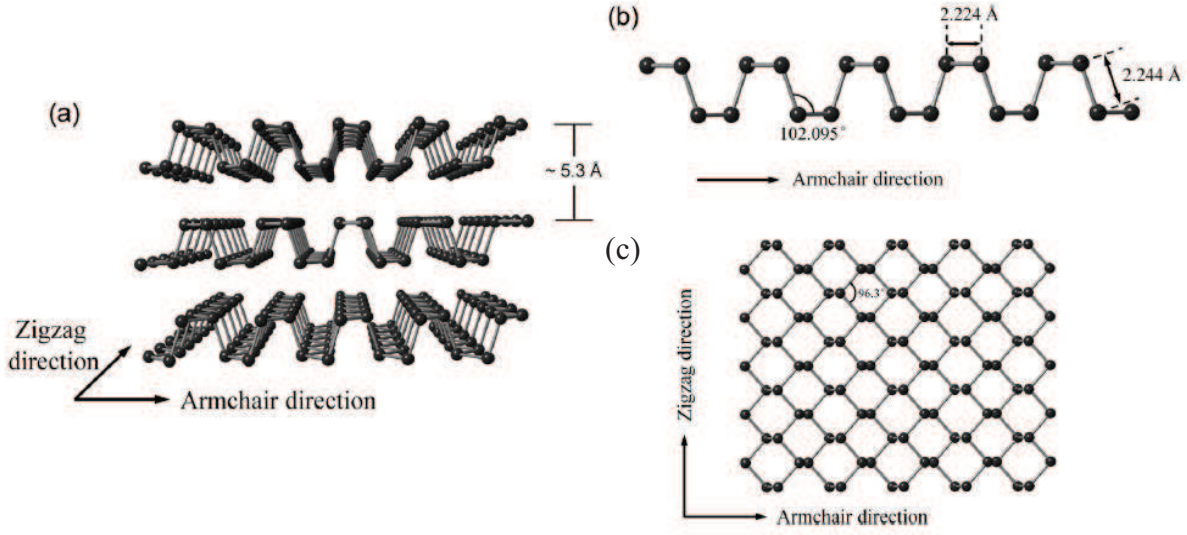

Figure (1.12) (a) Bulk BP consists with three stacked layers. (b) Side view shows the armchair orientation. (c) Top view of BP in x-y plane shows orientations of armchair and zigzag. Figure is copied from [70].

[69] and is in the following form [72]

$$\mathcal{H} = \begin{pmatrix} E_c + \eta_c k_x^2 + \nu_c k_y^2 & \gamma k_x + \beta k_y^2 \\ \gamma k_x + \beta k_y^2 & E_v - \eta_v k_x^2 - \nu_v k_y^2 \end{pmatrix}. \tag{1.21}$$

where E_c and E_v are the lowest energy of conduction band and the highest energy of valence band. Then the band gap is $\Delta = E_c - E_v \approx 2$ eV. The band parameters $\eta_{c,v}$ and $\nu_{c,v}$ are related to the in-plane effective masses and γ and β represent the coupling between the conduction and valence bands. The parameters have the following values [72]: $\eta_{c,v} = \hbar^2/0.4m_0 = 19.0763$ eV Å^2,$\nu_c = \hbar^2/1.4m_0 = 5.4504$eV Å^2,$\nu_v = \hbar^2/2.0m_0 = 3.8153$ eV Å^2,$\gamma = 4a/\pi = 2.8393$ eV Å, $\beta = 2a^2/\pi^2 = 1.0077$eVÅ^2 and $a = 2.23$ Å. Here m_0 is the free electron mass. From the Hamiltonian (1.21) we can find the corresponding energy dispersion for both the conduction and valence bands:

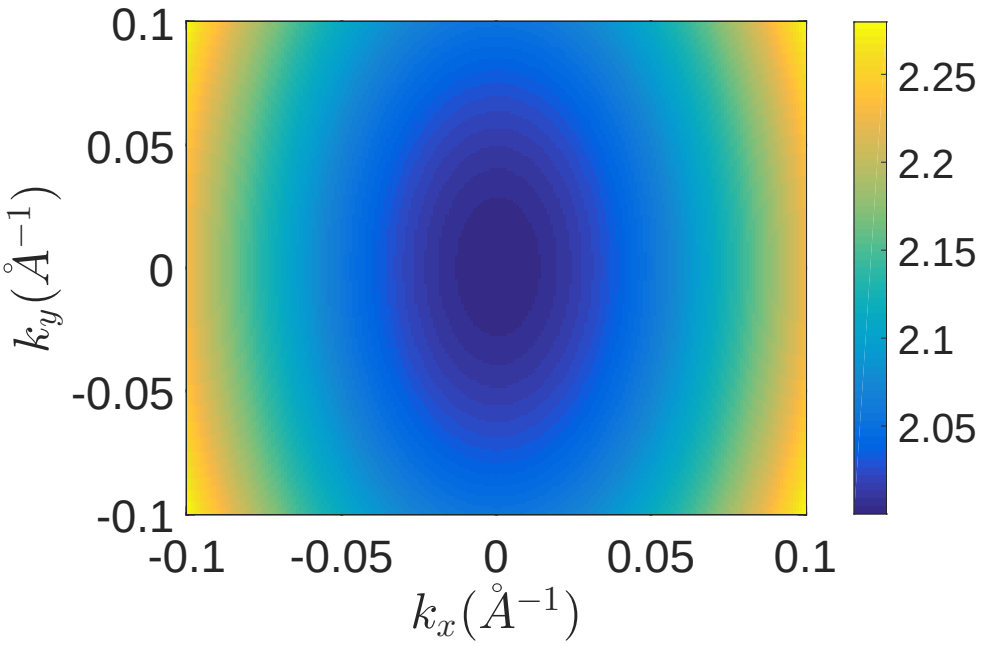

Figure (1.13) (Color) Energy dispersion of CB for phosphorene QD Eq. 1.22.

$$E_+ = \frac{1}{2}(p + \sqrt{p^2 - 4q}), \tag{1.22}$$

$$E_- = \frac{1}{2}(p - \sqrt{p^2 - 4q}), \tag{1.23}$$

where

$$\begin{aligned} p &= E_c + E_v + (\nu_c - \nu_v)k_y^2, \\ q &= (E_c + \eta_c k_x^2 + \nu_c k_y^2)(E_v - \eta_v k_x^2 - \nu_v k_y^2) - (\gamma k_x + \beta k_y^2)^2. \end{aligned}$$

The energy of the conduction band is shown in Fig. 1.13. We can see that the energy dispersion is highly anisotropic. We can create a finite phosphorene quantum dot by using a piece of phosphorene itself or by trapping potential. Here we consider a piece of phosphorene monolayer of a circular shape, which is characterized by radius R. In Chapter 5, first we find

the energy levels and the corresponding wave functions of such a quantum dot. Then we calculate the interband and intraband optical transitions within the quantum dot.

CHAPTER 2

ELECTRON SCATTERING BY STEP-LIKE DEFECT IN TOPOLOGICAL INSULATOR NANOFILM

By changing the thickness of the TI nanofilm one can control the gap in the dispersion law and introduce the defects into the system. The simplest defect is a step-like defect, which divides two regions of TI nanofilm with different thicknesses. Such type of defect with the height of a step ~ 30.5 Å was introduced on a surface of Bi_2Te_3 to study experimentally the oscillations of the local density of states due to the step defect. The step-like defect was also considered theoretically in Refs. [73, 74] within a 2D model of surface states of TI. The defect was introduced into the 2D effective Hamiltonian of the surface states as a δ-function potential.

Here we consider the properties of a one-dimensional step-like defect on a surface of TI nanofilm. An electron, propagating along the surface of TI nanofilm, can be scattered by the defect, which results in generation of reflected and transmitted electron waves. We study how electron reflectance and transmittance depend on the parameters of the defect. Although some properties of the electron reflection can be explained within a picture of reflection from a step-like barrier, there are properties which are specific to TI system. Namely, the scattering of an electron by a step-like defect generates not only reflected and transmitted electron waves, but also localized (evanescent) modes. Such modes are localized at the defect, which results in an increase of the electron density at the defect.

2.1 Model and Main Equations

We consider a TI nanofilm with a step-like singularity, which means that the TI nanofilm consists of two regions with different thicknesses – see Fig. 2.1(a). We assume that the linear step-like defect is described by an equation $x = 0$ with axis y parallel to the step-like defect

and axis z perpendicular to the nanofilm – see Fig. 2.1(a). In two regions, determined by the defect, the thickness of the nanofilm is L_1 at $x < 0$ (region 1) and L_2 at $x > 0$ (region 2). Below we consider both $L_1 < L_2$ and $L_1 > L_2$ cases.

We study the reflection (scattering) of an electron by the step-like defect. The electron, propagating in region 1 in the positive direction of axis x, is incident on the defect and is partially reflected (transmitted) by the defect. The specific feature of TI system is that the scattering of the incident electron by the defect produces not only the propagating (reflected and transmitted) electron waves but also the evanescent (localized) waves as schematically illustrated in Fig. 2.1(b).

To study the scattering of an electron by the step-like defect, we employ the effective low energy model of TI nanofilm, which is described by 4×4 matrix Hamiltonian of the following form [21]

$$\begin{aligned} \mathcal{H} &= \begin{pmatrix} \mathcal{H}_+ & 0 \\ 0 & \mathcal{H}_- \end{pmatrix} \\ &= D_1\frac{\pi^2}{L^2} + D_2\frac{\hat{p}^2}{\hbar^2} + \frac{A_2}{\hbar}\left(\hat{\sigma}_x\hat{p}_y - \hat{\sigma}_y\hat{p}_x\right) + (B_1\frac{\pi^2}{L^2} + B_2\frac{\hat{p}^2}{\hbar^2})\hat{\tau}_z \otimes \hat{\sigma}_z. \end{aligned} \tag{2.1}$$

where $\hat{\sigma}_i$ $(i = x, y, z)$ are Pauli matrices corresponding to spin degrees of freedom, and $\hat{\tau}_z$ is the Pauli matrix corresponding to electron pseudospin, which determines the block diagonal Hamiltonian matrix with $\mathcal{H}_+$ (for $\tau_z = 1$) and $\mathcal{H}_-$ (for $\tau_z = -1$). Here $\hat{p}_i = -\hbar\partial/\partial r_i$ $(i = x, y)$ is the electron 2D momentum, L is the thickness of the nanofilm, and A_2, B_1, B_2, D_1, D_2 are parameters of 3D model of TI. Below we consider Ti_2Se_3 TI, for which these parameters takes the following values [57] $A_2 = 4.1$ eV $\cdot$ Å, $B_1 = 10$ eV $\cdot$ Å^2 , $B_2 = 56.6$ eV $\cdot$ Å^2, $D_1 = 1.3$ eV $\cdot$ Å^2, $D_2 = 19.6$ eV $\cdot$ Å^2. The third term in Hamiltonian (2.1), which is determined by constant A_2, describes the spin-orbit interaction in the effective Hamiltonian of TI.

Since the electron dynamics for two components of pseudospin are decoupled, we consider scattering of an electron with only one component of pseudospin, for example, $\tau_z = 1$.

For such a component of pseudospin, the scattering is described by a 2×2 Hamiltonian, where the two components of the wave function correspond to two spin components, $\sigma_z = \pm 1$. The scattering amplitudes for pseudospin component $\tau_z = -1$ are the same as for $\tau_z = 1$.

Within each region (1 or 2) the nanofilm thickness is constant. Then the electron wave functions corresponding to Hamiltonian (2.1) have the plane wave form $\Psi \propto e^{i(k_x x + k_y y)}$, where (k_x, k_y) is an electron wave vector. The corresponding energy spectrum, which is given by expression

$$E_{\pm}(k, L) = \left(D_1 \frac{\pi^2}{L^2} + D_2 k^2 \right) \pm \sqrt{\left(B_1 \frac{\pi^2}{L^2} + B_2 k^2 \right)^2 + A_2^2 k^2}, \tag{2.2}$$

has a gap $\Delta_g(L) = 2B_1 \frac{\pi^2}{L^2}$, which is determined by the thickness of the nanofilm. Here $k = \sqrt{k_x^2 + k_y^2}$. For a given wave vector (k_x, k_y) there are two energy bands, $E_+(k)$ and $E_-(k)$, which can be identified as "conduction" and "valence" bands of TI nanofilm. The two component wave function, corresponding to wave vector (k_x, k_y) and energy $E_{\pm}(k_x, k_y)$ have the following form

$$\hat{\Psi}_{k_x, k_y, L} = \frac{1}{\sqrt{A_2^2 |k|^2 + \left(F_1 + N_1 k^2 - E_{\pm} \right)^2}} \times \begin{pmatrix} -A_2 (i k_x + k_y) \\ F_1 + N_1 k^2 - E_{\pm}(k, L) \end{pmatrix} e^{i(k_x x + k_y y)}. \tag{2.3}$$

where we introduced the following notations $F_1 = \big(D_1 + B_1\big)\pi^2/L^2$ and $N_1 = \big(D_2 + B_2\big)$.

For the reflection (elastic electron scattering) problem, we need to identify the reflected and transmitted states for a given incident electron wave. Such states are determined by the condition that the energy of the reflected (transmitted) electron is equal to the energy of the incident electron.

A specific feature of TI system is the existence of four different wave vectors, k, which have the same energy. Namely, at a given energy E there are four solutions of an equation

$E = E_{\pm}(k)$. These solutions are given by the following expressions

$$k_{1,\pm}(E,L) = \pm\sqrt{\frac{\beta+\sqrt{\beta^2+4\alpha\gamma}}{2\alpha}}, \tag{2.4}$$

$$k_{2,\pm}(E,L) = \pm\sqrt{\frac{\beta-\sqrt{\beta^2+4\alpha\gamma}}{2\alpha}}, \tag{2.5}$$

where $\alpha = B_2^2 - D_2^2$, $\beta = \big(B_1B_2 - D_1D_2\big)\frac{2\pi^2}{L^2} + 2ED_2 + A_2^2$, $\gamma = E\big(E - D_1\frac{2\pi^2}{L^2}\big) + (D_1^2 - B_1^2)\frac{\pi^4}{L^4}$. If energy E is not in the energy gap of TI nanofilm, then wave vectors $k_{1,\pm}$ are real and correspond to two propagating waves, whereas the wave vectors $k_{2,\pm}$ are purely imaginary and describe decaying and growing modes. If energy E is in the gap, i.e., $E_-(k=0) < E < E_+(k=0)$, then all solutions, $k_{1,\pm}$ and $k_{2,\pm}$, are imaginary, which means that there are no in-gap propagating modes and all the modes are either decaying or growing modes.

The existence of four different wave vectors with the same energy introduces an additional features in electron scattering by a defect in TI nanofilm. For a step-like defect the problem of scattering (reflection) is formulated as follows. An electron with wave vector $(k_x > 0, k_y)$ and energy $E_{\pm}(k)$ is propagating in the positive direction of axis x and is incident on the step-like defect. The direction of electron propagation is characterized by the angle of incidence, $\pi/2 \geq \varphi \geq 0$, defined as $\tan\varphi = k_y/k_x$. The scattering of an electron by the defect results in generation of two reflected and two transmitted propagating or evanescent waves, see Fig. 2.1(b). Such waves are determined by the condition that the energy of the reflected or transmitted wave is equal to the energy of the incident electron and the y component of the wave vector, k_y, of the incident electron is equal to the y component of the transmitted and reflected waves. Here for the reflected (transmitted) waves we need to choose the waves, which propagate or decay in the negative (positive) direction of axis x.

The corresponding wave functions are described by Eq. (2.3) and are characterized by the following parameters:

(i) the incident wave is $\hat{\Psi}_{k_x,k_y,L_1}$, where $k = k_{1,+}(E,L_1)$ and E is the energy of the incident electron,

(ii) the reflected waves are $\hat{\Psi}_{-k_x,k_y,L_1}$ (propagating wave) and $\hat{\Psi}_{-i\lambda,k_y,L_1}$ (evanescent wave), where $\lambda > 0$ and $-\lambda^2 + k_y^2 = [k_{2,+}(E, L_1)]^2$.
(iii) transmitted waves are $\hat{\Psi}_{k'_x,k_y,L_2}$ (propagating or evanescent wave) and $\hat{\Psi}_{i\lambda',k_y,L_2}$ (evanescent wave), where $(k'_x)^2 + k_y^2 = [k_{1,+}(E, L_2)]^2$, $\lambda' > 0$, and $-(\lambda')^2 + k_y^2 = [k_{2,+}(E, L_2)]^2$.

Then the electron wave function is

$$\hat{\Psi}_0 = \begin{cases} \hat{\Psi}_{k_x,k_y,L_1} + r_1\hat{\Psi}_{-k_x,k_y,L_1} + r_2\hat{\Psi}_{-i\lambda,k_y,L_1}, & x < 0, \\ t_1\hat{\Psi}_{k'_x,k_y,L_2} + t_2\hat{\Psi}_{i\lambda',k_y,L_2}, & x > 0, \end{cases} \tag{2.6}$$

where r_1, r_2 are amplitudes of the reflected waves and t_1, t_2 are amplitudes of the transmitted waves. The amplitudes r_1, r_2, t_1, and t_2 are found from the boundary condition, i.e., continuity of the wave function, $\hat{\Psi}_0$, and its derivative, $\partial_x\hat{\Psi}_0$, at $x = 0$, which is equivalent to continuity of the current (electron flux). Then the reflection and transmission coefficients are $R = |r_1^2|$ and $T = 1 - R$, respectively. Since the evanescent modes do not contribute to electron current, there is no contribution of the evanescent modes into the reflectance and transmittance.

2.2 Results and Discussion

2.2.1 Reflectance

Since the evanescent waves produce zero current, only the propagating waves contribute to the electron reflectance. Thus, if the energy of the incident electron, which is in the region 1 of the nanofilm with thickness L_1, is in the energy gap of the TI nanofilm in region 2 with thickness L_2, then there are no propagating transmitted waves and the transmittance in this case is 0, i.e., the reflectance is exactly 1. Such total internal reflection can be realized only if $\Delta_g(L_1) = 2B_1\frac{\pi^2}{L_1^2} < \Delta_g(L_2) = 2B_1\frac{\pi^2}{L_2^2}$, i.e. $L_1 > L_2$.

If the energy of the incident electron is not in the gap of TI nanofilm in region 2 then there is a finite reflectance of the incident electron. In Fig. 2.2 the reflectance is shown as a function of thickness L_2 [see Fig. 2.1(a)] for different wave vectors k of the incident

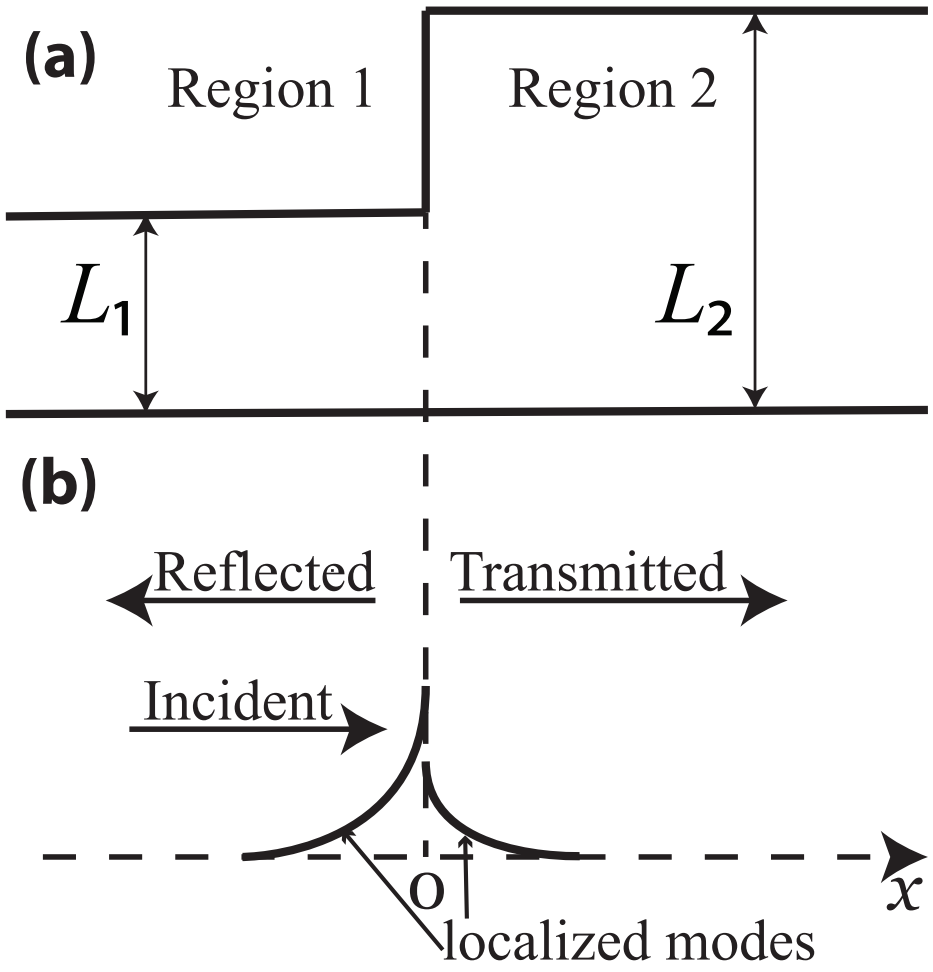

Figure (2.1) (a) Schematic illustration of a step-like defect on a surface of topological insulator nanofilm. The step-like defect at $x = 0$ divides TI nanofilm into two regions: region 1 with nanofilm thickness L_1 and region 2 with nanofilm thickness L_2. (b) Schematic illustration of electron reflection from the step-like defect. Incident, reflected, and transmitted propagating waves are shown by arrows. The localized modes, generated by electron reflection, are also shown. The modes are localized at the defect.

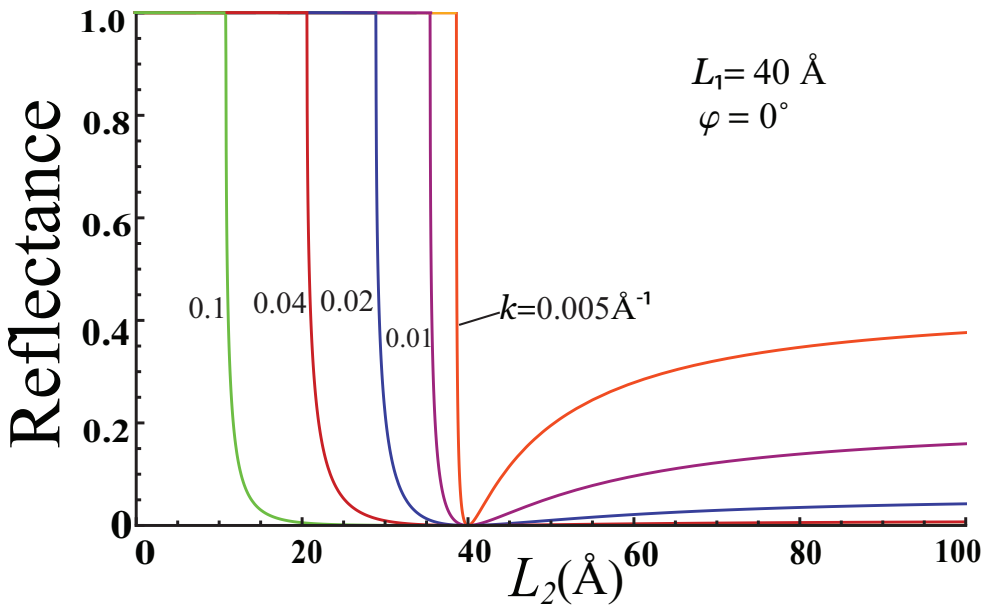

Figure (2.2) Electron reflectance is shown as a function of the thickness L_2 (see Fig. 2.1) of nanofilm in region 2 for different values of electron energy. The thickness of TI nanofilm in region 1 is $L_1 = 40$ Å and the angle of incidence is $\varphi = 0$. The numbers next to the lines are the wave vectors of the incident electron in units of Å^{-1}.

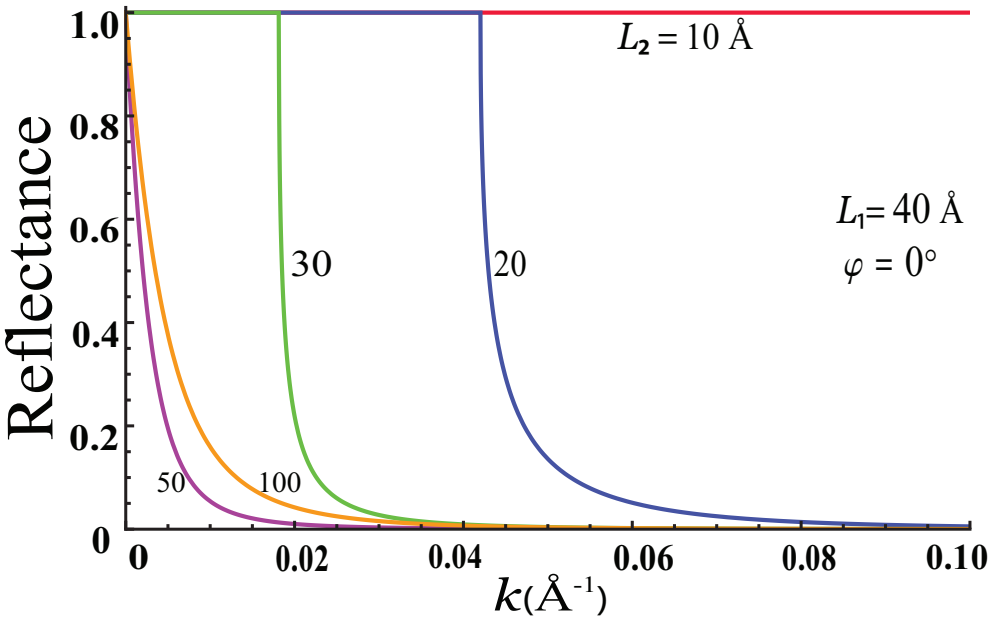

Figure (2.3) Electron reflectance is shown as a function of the wave vector, k, of the incident electron for different thicknesses L_2 of TI nanofilm in region 2. The thickness of TI nanofilm in region 1 is $L_1 = 40$ Å and the angle of incidence is $\varphi = 0$. The numbers next to the lines are the values of the thickness L_2.

electron, i.e., for different energies of the incident electron. The thickness of the nanofilm in region 1 is fixed and is equal to $L_1 = 40$ Å. The reflectance is zero at $L_2 = L_1 = 40$ Å, which corresponds to homogeneous TI nanofilm with constant thickness. At $L_2 \neq L_1$ the reflectance is not zero, but it shows different behaviours for $L_2 > L_1$ and $L_2 < L_1$. At $L_2 > L_1$ the reflectance monotonically increases with L_2, reaching some asymptotic values at large L_2, which are around 20% - 40 % depending on the electron energy.

At $L_2 < L_1$, within a narrow interval of thickness L_2, the reflectance shows very strong dependence on L_2. At each value of electron energy (or wave vector), there is a critical thickness $L_2^{(cr)}$ so that at $L_2 \leq L_2^{(cr)}$ an electron experiences total internal reflection with reflectance equal to one. This corresponds to the condition that the electron energy E is in the energy gap of TI nanofilm in region 2. The critical thickness is determined by an equation $E_+(0, L_2^{(cr)}) = E$, which gives $L_2^{(cr)} = \sqrt{\pi^2(D_1 + B_1)/E}$. Near the critical thickness the reflectance shows very strong dependence on L_2 with sharp increase from zero to one

within a narrow interval of thicknesses L_2.

The reflectance as a function of electron wave vector (energy) is shown in Fig. 2.3 for different values of L_2. At $L_2 > L_1 = 40$ Å, the reflectance is large within narrow interval of wave vectors near $k = 0$ and becomes one at $k = 0$. At $L_2 < L_1$, there a range of wave vectors, which satisfy the condition of total reflection, i.e. the energy E is in the gap of nanofilm of thickness L_2. The total reflection occurs at small wave vectors (small energies), i.e., at $k < k^{(cr)}(L_2)$. The critical wave vector is determined by the condition that the electron energy is exactly at the edge of the "conduction" band dispersion for the nanofilm of region 2. Thus, the critical wave vector satisfies an equation $E = E_+(k^{(cr)}, L_2)$. The dependence of the reflectance on the wave vector (energy) is strong near the critical value, $k \approx k^{(cr)}$. Within a good accuracy, one can say that the reflectance is one within a finite range of wave vectors, $k < k^{(cr)}(L_2)$, and zero at $k > k^{(cr)}(L_2)$.

This property can be used to design an electron filter to select electrons within a given range of energies. Namely, if an electron beam with a broad energy distribution is incident on a step-like singularity with the known values of L_1 and $L_2 < L_1$, then only the electrons with $k < k^{(cr)}(L_2)$ will be totally reflected.

In Fig. 2.4 we show the dependence of the reflectance on the angle of incidence, φ, for different wave vectors (energies) of the incident electron and different thicknesses, L_2, of TI nanofilm in region 2. The total internal reflection, which can be realized only at $L_2 < L_1$, occurs at $\varphi > \varphi^{(cr)}$. The critical angle is determined by condition $E = E_+(k \sin\varphi^{(cr)}, L_2)$, i.e., k_x in region 2 is zero at the critical angle and the y component of the wave vector is $k \sin\varphi^{(cr)}$. Comparing small [Fig. 2.4(a)] and large electron energies [Fig. 2.4(b)], one can see that the critical angle $\varphi^{(cr)}$ increases with electron energy. The critical angle also increases with the thickness L_2. If the thickness L_2 of the nanofilm in region 2 satisfies an inequality $E_+(0, L_2) \leq E$, then even at zero angle of incidence the electron experiences total reflection. In this case for all angles there is total internal reflection of the incident electron [see $L_2 = 10$ and 20 Å in Fig. 2.4(a) and $L_2 = 10$ Å in Fig. 2.4(b)]. Near the critical angle $\varphi \approx \varphi^{(cr)}$ (at $L_2 < L_1$), the reflectance shows strong dependence on the angle φ with sharp increase from

zero to one within small interval of angles. Comparing the results for $L_2 = 100$ Å in Fig. 2.4(a) and Fig. 2.4(b), one can conclude that the dependence of the reflectance on the angle becomes stronger with increasing electron energy. At $L_2 > L_1$, the total internal reflection cannot be realized and the reflectance shows a monotonic dependence on the angle φ.
The above data on the reflectance from the step-like defect show that the total reflection can be realized only at $L_2 < L_1$. At such values of nanofilm thickness L_2, by varying parameters of the system, e.g., angle of incidence or electron energy, one can change the reflectance from small value (almost zero) to one within narrow interval of parameters. Thus, the reflectance shows strong dependence on the parameters of the system near their critical values.

2.2.2 Evanescent modes

The scattering of an electron by a step-like defect generates localized evanescent modes. Such modes are shown schematically in Fig. 2.1(b). The evanescent modes are localized at the step-like defect and exponentially decay in both directions away from the defect (in both negative and positive directions of axis x) – see Fig. 2.1(b). The evanescent modes do not directly contribute to electron reflectance, but they increase the electron density near the step-like defect.

The amplitudes of the evanescent modes are strongly correlated with electron reflectance. The amplitudes of the evanescent modes are large only when the electron experiences total reflection, otherwise the amplitudes are relatively small. Typical spatial distributions of electron density in the evanescent modes are shown in Fig. 2.5 for different values of electron wave vector (electron energy) and different thicknesses L_2 of nanofilm in region 2. Here ρ_1 and ρ_2 in Fig. 2.5 correspond to two components of the electron wave function in TI nanofilm – see Eq. (2.3). The two components of the wave function correspond to two directions of electron spin, i.e., spin-up and spin-down. The figure illustrates two cases: weak reflection [Fig. 2.5(a) and (c)] and strong total reflection [Fig. 2.5(b) and (d)].

For weak reflection, the amplitudes of the evanescent modes are small. The corresponding increase of the local electron density near the step-like defect is less than 1 %. The wave

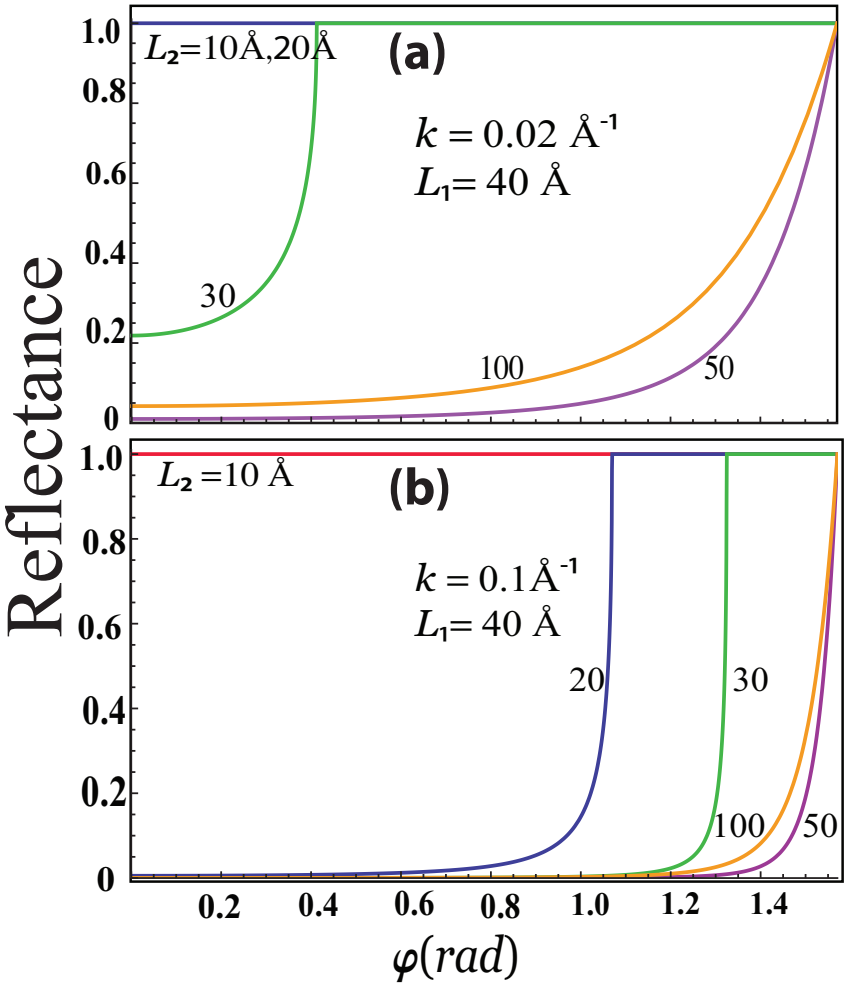

Figure (2.4) Electron reflectance is shown as a function of angle of incidence, φ, for different values of the nanofilm thickness, L_2, in region 2. The thickness of the nanofilm in region 1 is $L_1 = 40$ Å and the wave vector of the incident electron is (a) $k = 0.02$ Å^{-1} and (b) $k = 0.1$ Å^{-1}. The numbers next to the lines are the values of the thickness L_2. In panel (a), the electron reflectance is exactly one at $L_2 = 10$ Å and 20 Å.

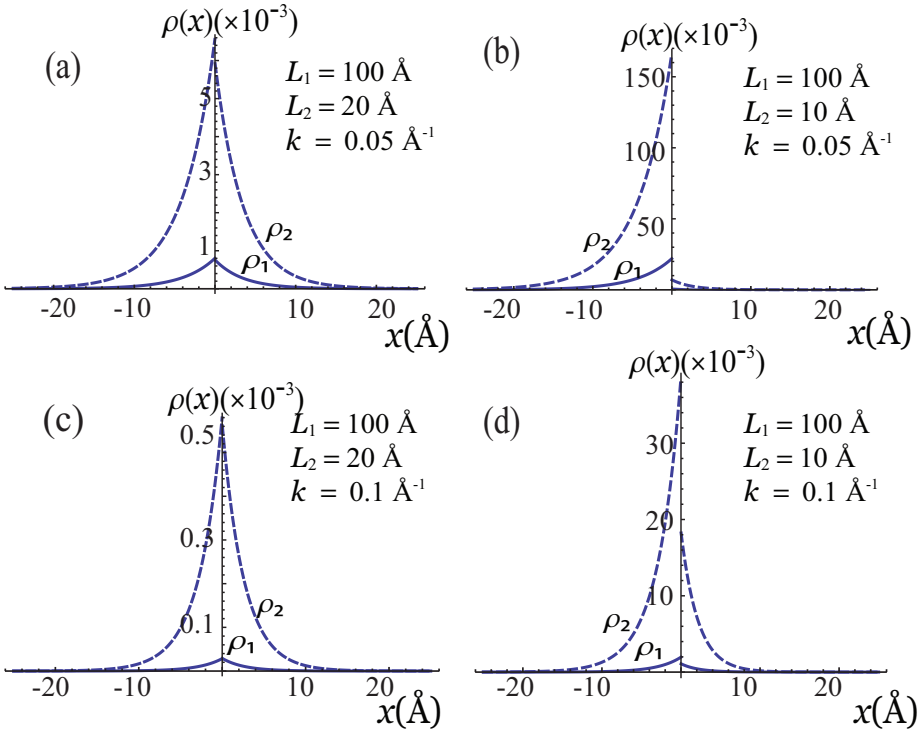

Figure (2.5) Spatial distribution of electron density in the evanescent (localized) modes is shown for different parameters of the nanofilm and different electron energies (wave vectors). Two densities ρ_1 and ρ_2 correspond to two components of the wave function. The parameters of the system (thicknesses L_1 and L_2 and electron wave vector k) are shown in corresponding panels.

function of the evanescence modes is almost continuous function of the position – see Fig. 2.5(a) and (c), where the density of the evanescent mode is continuous at $x = 0$.

For total reflection [see Fig. 2.5(b) and (d)], the typical amplitude of the evanescent mode is large, which results in strong increase, by up to 60 %, of local electron density near the defect. The amplitudes of the evanescent modes are large in region 1 only, whereas they are small in region 2. The localization length of the evanescent modes is around 10 Å. The wave function, which describes the localized evanescent mode, is discontinuous at $x = 0$. Note, that the continuity of the electron wave function is satisfied for the total wave function, which includes both propagating and evanescent modes. Figures 2.5(b) and (d) also show that with decreasing electron energy, i.e., when the energy becomes further away from the edge of the "conduction" band, the amplitude of the evanescent mode increases.

Under the condition of total reflection, the density ρ_1 (or ρ_2) of the evanescent modes is the largest in the region 1, whereas the density in region 2 is almost order of magnitude smaller. Below we describe the evanescent modes in terms of their densities at the step-like defect in region 1, i.e., at point $x = 0_-$.

In Fig. 2.6, two components of electron density of evanescent modes at $x = 0_-$ are shown as the functions of nonofilm thickness, L_2, in region 2. The electron density in evanescent mode is large for small thickness L_2 and monotonically decreases with L_2. Both in Fig. 2.6 (a) and (b) there are singularities in the dependence of electron density on thickness L_2. These singularities occur at $L_2 \approx 19$ Å in Fig. 2.6 (a) and at $L_2 \approx 11$ Å in Fig. 2.6 (b) and correspond to critical points of transition from total reflection at small L_2 to weak reflection at large L_2 – see Fig. 2.2. Thus, the data, shown in Fig. 2.6, illustrate that large amplitudes of evanescent modes are realized only in the case of total electron reflection. The farther the system from the critical point, i.e., the transition point from total reflection to small reflection, the larger the amplitudes of evanescent modes.

In Fig. 2.7 the densities of evanescent modes, $\rho_1(0_-)$ and $\rho_2(0_-)$, are shown as the functions of the angle of incidence, φ. The system is in the regime of total reflection. The densities of evanescent modes have nonmonotonic dependence on the angle φ with maximum

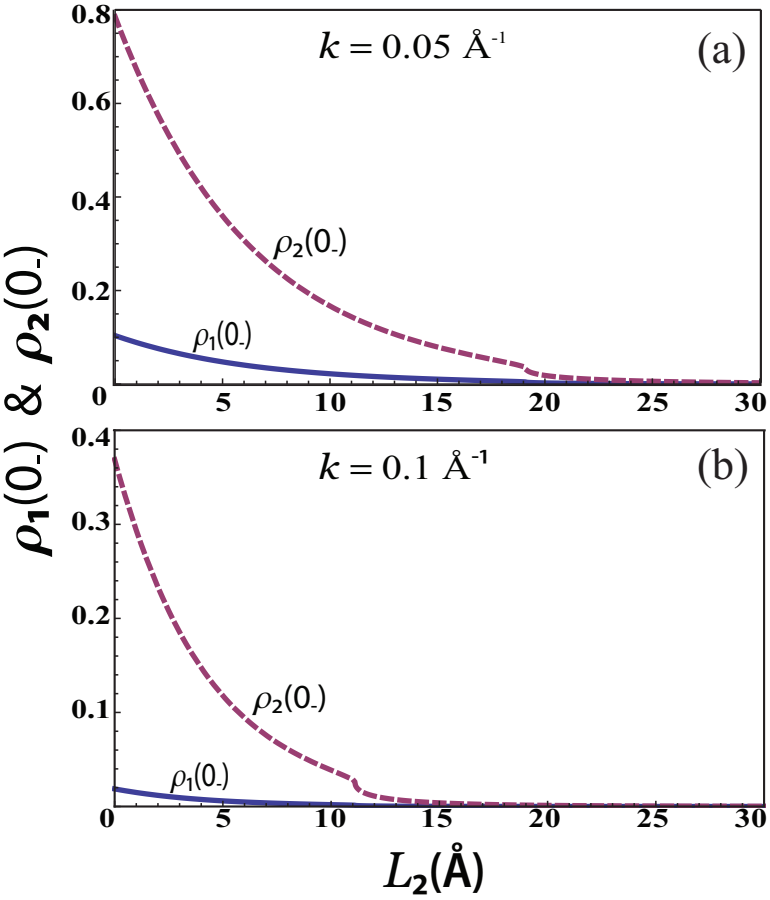

Figure (2.6) The electron density in the evanescent mode near the step-like defect in region 1, i.e. at $x = 0_-$, is shown as a function of the nanofilm thickness L_2 in region 2. Two densities ρ_1 and ρ_2 correspond to two components of the wave function. The nanofilm thickness in region 1 is $L_1 = 40$ Å and the wave vector of the incident electron is (a) $k = 0.05$ Å^{-1} and (b) $k = 0.1$ Å^{-1}. Singularities in the graphs at $L_2 \approx 18$ Å [panel (a)] and $L_2 = 12$ Å [panel (b)] correspond to transition from total electron reflection at small L_2 to small reflection at large L_2.

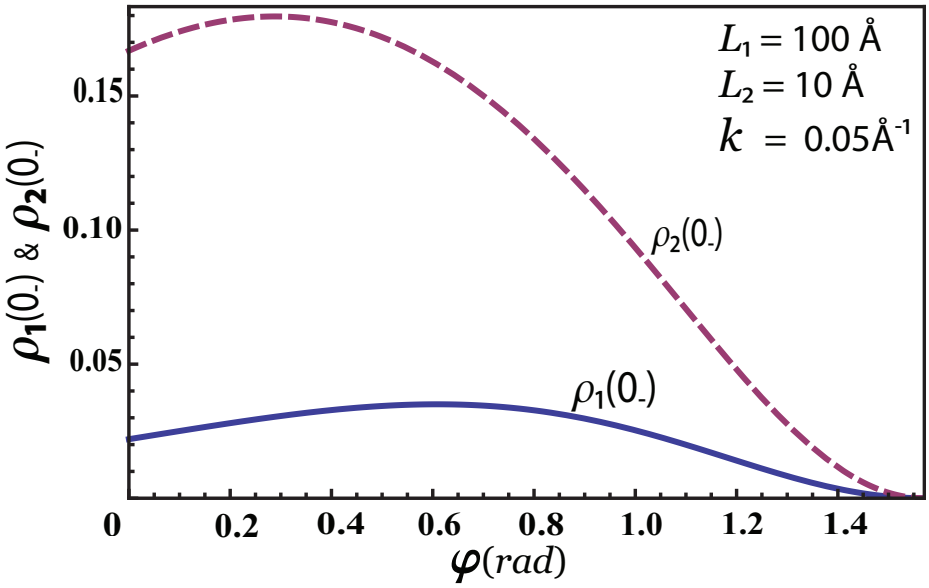

Figure (2.7) The electron density in the evanescent mode near the step-like defect in region 1, i.e. at $x = 0_-$, is shown as a function of the angle of incidence. Two densities ρ_1 and ρ_2 correspond to two components of the wave function. The nanofilm thicknesses in region 1 is $L_1 = 100$ Å and in region 2 is $L_2 = 10$ Å. The wave vector of the incident electron is $k = 0.05$ Å^{-1}.

values at some finite values of φ, e.g., ρ_2 has maximum at $\varphi \approx 18^0$. At $\varphi = 90^0$, i.e., an electron is propagating parallel to the defect, the reflectance is 1 (see Fig. 2.4) and no evanescent mode is generated at the defect.

The above results are shown for pseudospin $\tau_z = 1$. In this case the densities ρ_1 and ρ_2 correspond to up and down directions of electron spin, respectively. For pseudospin $\tau_z = -1$, the results for electron reflectance and transmittance, and intensity of evanescent modes will be exactly the same as for $\tau_z = 1$ with only difference that for $\tau_z = -1$ the densities ρ_1 and ρ_2 correspond to down and up directions of electron spin.

The decaying states at the surface of 3D TI near the linear defect have been discussed in Refs. [75–77], where the decaying modes are due to warping terms in the effective TI Hamiltonian.

2.3 Conclusion

Scattering of an electron propagating on a surface of TI nanofilm is determined by specific energy dispersion law of TI system. Namely, the electron dispersion in TI nanofilm has a gap, the magnitude of which depends on the thickness of TI nanofilm, $\Delta_g \propto L^{-2}$. The gapped structure of electron energy dispersion introduces two types of electron states on a surface of TI nanofilm. If electron energy is in the energy gap, then there are only decaying (evanescent) and growing electron modes in the nanofilm. Whereas if electron energy is not in the energy gap, then there are both propagating and evanescent (and growing) modes. Coexistence of both propagating and evanescent modes is a specific feature of TI nanofilm. Due to such coexistence of different types of modes, the scattering of an electron by a step-like defect produces not only reflected and transmitted electron waves, but also modes, which are localized at the defect.

The amplitude of the reflected electron wave strongly depends on the position of electron energy relative to the energy gap in region 2 of the nanofilm, i.e., in the transmitted region. If electron energy is in the energy gap of region 2, then the reflectance is exactly one, which corresponds to total internal reflection. If the electron energy is not in the energy gap, then the reflectance is small and the electron is almost totally transmitted to region 2. The critical points, dividing these two regimes, are defined by the condition that the electron energy is at the band edge of energy dispersion in region 2. Near the critical points, the dependence of the electron reflectance on the parameters of the system, such as thickness of the nanofilm or electron energy, is strong. The reflectance changes from one (total reflection) to zero (small reflection) within a narrow interval of parameters.

The amplitudes of the generated evanescent modes, which are localized at the step-like defect, are large in the case of total internal reflection and small if the reflectance is small. Thus, if an electron with a given energy E is incident on a region of TI nanofilm, which does not support electron propagating waves at energy E, then there is a strong enhancement of local electron density near the boundary of such region. The electron density near the

boundary (defect) increases by up to 60 %. Such strong increase of the local electron density can be observable in many electron system, when the scattering of many electrons by the defect is studied. The inter-electron interactions combined with the local increase of the electron density near the defect can introduce additional scattering potential near the step-like defect. Such additional potential can modify the scattering properties of many electron systems.

In the analysis of electron scattering from a step-like defect we assumed that the width w of the step is infinitely small. For a finite width of the step, the above results are valid as long as the width is much smaller than the electron wavelength, i.e., $kw \ll 1$. For example, for $k = 0.05$ Å^{-1} the limitations on the width of the step is $w \ll 20$ Å. For larger values of $w \geq 20$ Å, the scattering amplitude and formation of evanescent modes are expected to be suppressed.

CHAPTER 3

QUANTUM DOT IN TOPOLOGICAL INSULATOR NANOFILM

In this chapter we consider a quantum dot in TI nanofilm. We introduce a quantum dot as a finite region of TI nanofilm with a larger thickness. Due to a gapped structure of the energy dispersion in TI nanofilm, such a quantum dot can localize an electron. We consider only a single electron problem and for a single electron calculate both the energy spectra and the optical transitions within a TI quantum dot. The main results in this chapter has been published in Journal of Physics : Condensed Matter [2]

3.1 Model and Main equations

We employ a TI nanofilm, which is characterized by nanoscale thickness L, to design a TI quantum dot. A quantum dot in such nanofilm is introduced as a region of the nanofilm of larger thickness. We assume that the quantum dot has cylindrical symmetry and is characterized by its height h and radius R – see Fig. (3.1). Thus the quantum dot can be described as topological insulator nanofilm with thickness L at $\rho > R$ and thickness $L+h$ at $\rho < R$, where ρ is the 2D distance from the center of the quantum dot. Below we consider only one set of thicknesses of the system, i.e., $L = 20$ Å and $h = 20$ Å, and we vary the radius R of the quantum dot.

To find the energy spectrum of the quantum dot system and corresponding optical transitions, we introduce a 4×4 matrix Hamiltonian which represents the effective low energy model of topological insulator nanofilm. The Hamiltonian describes the 2D in-plane

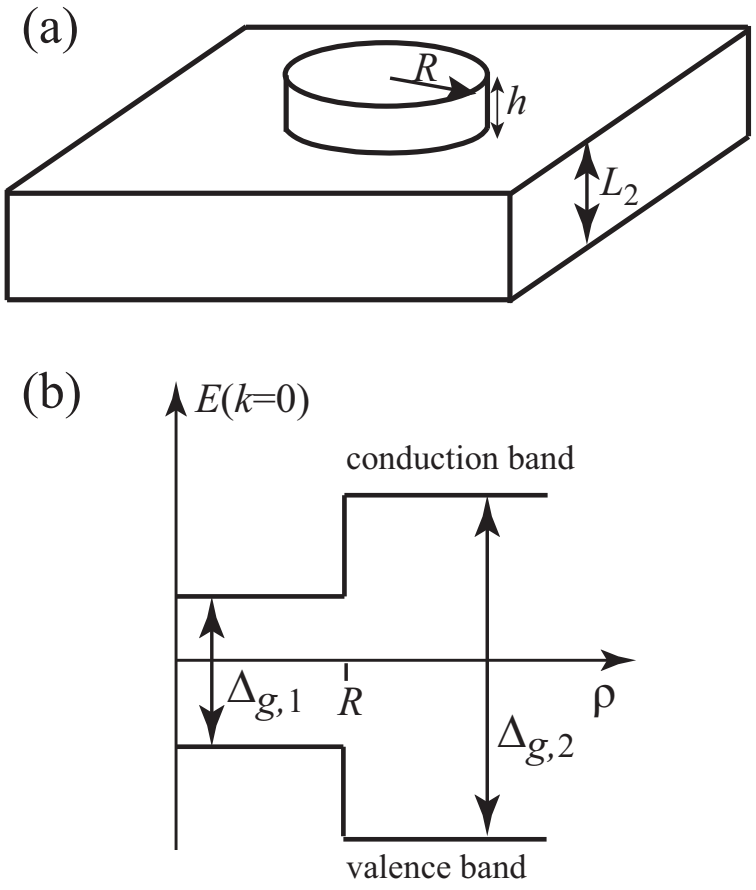

Figure (3.1) (a)Schematic illustration of TI quantum dot of cylindrical symmetry. The TI nanofilm has a thickness L_2. The quantum dot is introduced as region of nanofilm with thickness L_1 and is characterized by its height $h = L_1 - L_2$ and radius R. (b) Band edge profile of TI quantum dot is shown schematically for conduction and valence bands of the system. The bandgaps $\Delta_{g,1}$ and $\Delta_{g,2}$ are the bandgaps of TI nanofilm with thickness L_1 and L_2, respectively.

electron dynamics in TI nanofilm and has the following form [21]

$$\begin{aligned}\mathcal{H} &= \begin{pmatrix} \mathcal{H}_+ & 0 \\ 0 & \mathcal{H}_- \end{pmatrix} \\ &= D_1\frac{\pi^2}{L^2} + D_2\frac{\hat{p}^2}{\hbar^2} + \frac{A_2}{\hbar}\left(\hat{\sigma}_x\hat{p}_y - \hat{\sigma}_y\hat{p}_x\right) + \left(B_1\frac{\pi^2}{L^2} + B_2\frac{\hat{p}^2}{\hbar^2}\right)\hat{\tau}_z \otimes \hat{\sigma}_z. \end{aligned} \tag{3.1}$$

where $\hat{\sigma}_i$ $(i = x, y, z)$ are Pauli matrices corresponding to spin degrees of freedom, and $\hat{\tau}_z$ is the Pauli matrix corresponding to electron pseudospin, which describes the block diagonal Hamiltonian matrix with $\mathcal{H}_+$ (for $\tau_z = 1$) and $\mathcal{H}_-$ (for $\tau_z = -1$). Here $\hat{p}_i = -\hbar\partial/\partial r_i$ $(i = x, y)$ is the electron 2D momentum, L is the thickness of the nanofilm, and A_2, B_1, B_2, D_1, D_2 are parameters of 3D model of TI. Below we consider Ti_2Se_3 TI, for which these parameters are [57] $A_2 = 4.1$ eV $\cdot$ Å, $B_1 = 10$ eV $\cdot$ Å^2 , $B_2 = 56.6$ eV $\cdot$ Å^2, $D_1 = 1.3$ eV $\cdot$ Å^2, $D_2 = 19.6$ eV $\cdot$ Å^2.

For homogeneous TI nanofilm, the electron states are characterized by a 2D wave vector, $(k_x, k_y) = (p_x, p_y)/\hbar$, and the corresponding energy spectrum,

$$E_\pm(k, L) = \left(D_1\frac{\pi^2}{L^2} + D_2k^2\right) \pm \sqrt{\left(B_1\frac{\pi^2}{L^2} + B_2k^2\right)^2 + A_2^2k^2}, \tag{3.2}$$

has two bands (branches): (i) "conduction" band with energy E_+ and positive effective mass at $p = 0$ and (ii) "valence" band with energy E_- and negative effective mass. The band edges for TI nanofilm of thickness L are at $E_c(L) = (D_1 + B_1)\frac{\pi^2}{L^2}$ for conduction band and at $E_v(L) = (D_1 - B_1)\frac{\pi^2}{L^2}$ for valence band. The corresponding bandgap is $\Delta_g = 2B_1\frac{\pi^2}{L^2}$. Thus the variable thickness of TI nanofilm [Fig. (3.1)] introduces variation of the conduction and valence band edges, which generates confinement potential for both conduction and valence bands – see Fig. (3.1)b.

To find the energy spectrum of a quantum dot we determine at a given energy E the general solution of the Schrödinger equation with Hamiltonian (3.1) in two regions $\rho < R$ and $\rho > R$. Then the continuity condition at the boundary $\rho = R$ determines the discrete energy

spectrum of the quantum dot. From the eigenvalue equation, derived from the matrix Hamiltonian (3.1), one can obtain that for a given energy E there are four values of wave vectors, corresponding to decaying and propagating waves in the nanofilm of a given thickness. These wave vectors are

$$k_{1,\pm}(E,L) = \pm\sqrt{\frac{\beta+\sqrt{\beta^2+4\alpha\gamma}}{2\alpha}}, \tag{3.3}$$

$$k_{2,\pm}(E,L) = \pm\sqrt{\frac{\beta-\sqrt{\beta^2+4\alpha\gamma}}{2\alpha}}, \tag{3.4}$$

where $\alpha = B_2^2 - D_2^2$, $\beta = \big(B_1B_2 - D_1D_2\big)\frac{2\pi^2}{L^2} + 2ED_2 + A_2^2$, $\gamma = E\big(E - D_1\frac{2\pi^2}{L^2}\big) + (D_1^2 - B_1^2)\frac{\pi^4}{L^4}$. If $E > E_+$ or $E < E_-$, i.e., the energy is not in the energy gap of TI nanofilm, then $k_{1,\pm}$ are real and correspond to two propagating waves, whereas $k_{2,\pm}$ are purely imaginary and determine decaying and growing modes. If $E_+ > E > E_-$, i.e., the energy is in the band gap, then all solutions, $k_{1,\pm}$ and $k_{2,\pm}$, are imaginary and describe either decaying or growing modes.

The localized modes of a quantum dot exist only in the following energy range $E_-(L+h) > E > E_-(L)$ (valence band states) and $E_+(L) > E > E_+(L+h)$ (conduction band states). In this energy range, the wave vector $k_{1,\pm}(E, L+h)$ is real and corresponds to a propagating mode inside the quantum dot, while $k_{2,\pm}(E, L+h)$, $k_{1,\pm}(E,L)$, $k_{2,\pm}(E,L)$ are imaginary and correspond to decaying modes both inside and outside the quantum dot. A specific feature of TI quantum dot is that inside quantum dot there are both propagating and decaying modes simultaneously.

Due to a double pseudospin degeneracy of electronic states, below we calculate the energy spectra of TI quantum dot for one component, e.g., $\tau_z = 1$, of pseudospin only. In two regions ($\rho < R$ and $\rho > R$) the electron wave function with z-component of angular momentum m has the following form

$$\psi(\rho < R) = \begin{pmatrix} a_1Q_1J_m(\kappa\rho) + a_2M_1I_m(q\rho)e^{im\varphi} \\ a_1Q_2J_{m+1}(\kappa\rho) + a_2M_2I_{m+1}(q\rho)e^{im\varphi} \end{pmatrix}, \tag{3.5}$$

for $\rho < R$ and

$$\psi(\rho > R) = \begin{pmatrix} a_3\Lambda_1 K_m(q_1\rho) + a_4 F_1 K_m(q_2\rho)e^{im\varphi} \\ a_3\Lambda_2 K_{m+1}(q_1\rho) + a_4 F_2 K_{m+1}(q_2\rho)e^{i(m+1)\varphi} \end{pmatrix}, \tag{3.6}$$

for $\rho > R$, where the constants a_j, $j = 1, \ldots, 4$, are determined from continuity of the wave function and its derivative and from a normalization condition. Here $\kappa = k_{1,+}(E, L+h)$, $q = k_{2,+}(E, L+h)/i$, $q_1 = k_{1,+}(E, L)/i$, and $q_2 = k_{2,+}(E, L)/i$. We also introduced the following notations

$$\begin{aligned}
Q_1 &= -A_2\kappa, \\
Q_2 &= (D_1 + B_1)\pi^2/(L+h)^2 + (D_2 + B_2)\kappa^2 - E, \\
M_1 &= -A_2 q, \\
M_2 &= (D_1 + B_1)\pi^2/(L+h)^2 - (D_2 + B_2)q^2 - E, \\
\Lambda_1 &= A_2 q_1, \\
\Lambda_2 &= (D_1 + B_1)\pi^2/L^2 - (D_2 + B_2)q_1^2 - E, \\
F_1 &= A_2 q_2, \\
F_2 &= (D_1 + B_1)\pi^2/L^2 - (D_2 + B_2)q_2^2 - E.
\end{aligned}$$

In Eqs. (3.5)-(3.6), J_m is the Bessel function of the first kind, I_m and K_m are modified Bessel functions of the first and the second kind, respectively.

The energy spectrum is determined by the boundary conditions, which are the continuity of wave function and that of its derivative at the boundary of the quantum dot, i.e.,

$$\psi\,|_{\rho=R+0} = \psi\,|_{\rho=R-0}, \tag{3.7}$$

$$\left.\frac{\partial\psi}{\partial\rho}\right|_{\rho=R+0} = \left.\frac{\partial\psi}{\partial\rho}\right|_{\rho=R-0}. \tag{3.8}$$

From these conditions we obtain the matrix equation, $\mathcal{M}(E)\mathbf{a} = 0$, on coefficients a_j, where

$\mathcal{M}(E)$ is a 4×4 matrix, the elements of which depend on energy E. Then the energy spectrum is determined from numerical solution of nonlinear equation $\det \mathcal{M}(E) = 0$.

The optical transitions between the localized states of the quantum dot are determined by a velocity operator, $v_i \propto \partial\mathcal{H}/\partial p_i$, which, for example, for y-polarized light has the form

$$v_y = \begin{bmatrix} -2N_1 k_y & -A_2 \\ -A_2 & -2N_2 k_y \end{bmatrix}, \tag{3.9}$$

where we consider only one component of the pseudospin, τ_z. Then the intensity of optical transitions between the initial state i and the final state f is

$$I_{if} \propto | < \psi_i | v_y | \psi_f > |^2. \tag{3.10}$$

This expression determines the intensities of both interband and intraband optical transitions. The above expressions (3.9)-(3.10) also define the selection rule for optical transitions, which is

$$\Delta m = m_f - m_i = \pm 1, \tag{3.11}$$

where m_i is the angular momentum of an electron in the initial state and m_f is the angular momentum of an electron in the final state. The selection rule (3.11) is the same for both interband and intraband transitions.

3.2 Results and Discussion

3.2.1 Energy spectrum

Below we consider only a single particle energy spectrum. For many electron systems in the quantum dot, this means that we disregard the electron-electron interactions. At a given radius R, a TI quantum dot has a finite number of localized energy levels in the conduction and valence bands. The number of levels in the quantum dot increases with radius R. In Fig. 3.2 the energy levels with angular momentum $m = 0$, 1, and 2 are shown as functions

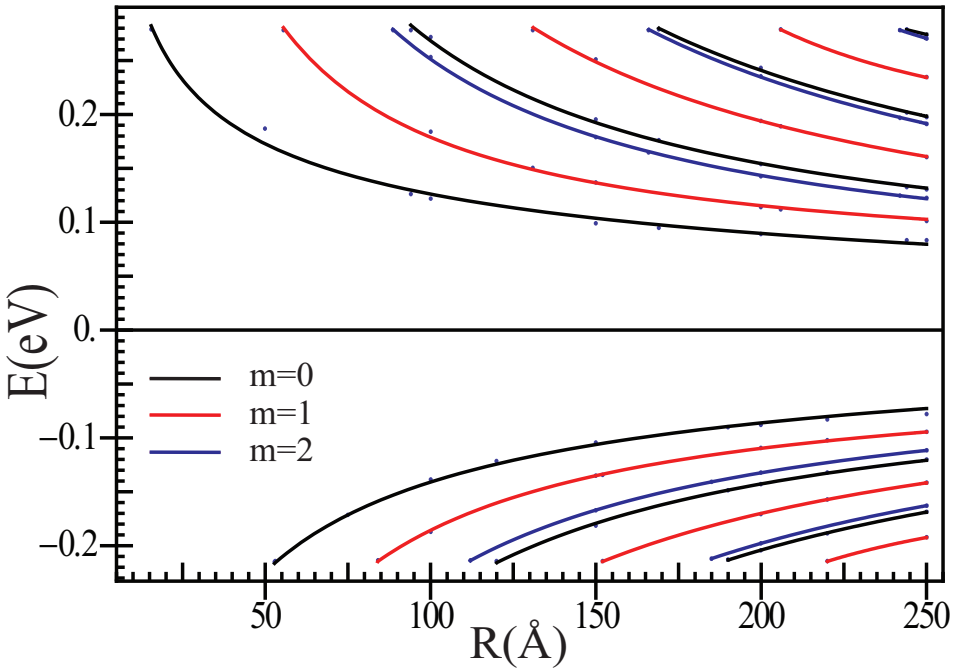

Figure (3.2) Energy levels of conduction band (positive energies) and valence band (negative energies) are shown as a function of quantum dot radius R. Only the levels with angular momentum $m = 0$, 1, and 2 are shown.

of quantum dot radius. The energy levels follow the general tendency: with increasing R the absolute value of level's energy decreases. The interlevel energy separation also decreases with increasing R.

For a given angular momentum m there is a critical size of the quantum dot $R_m^{(cr)}$, so that the energy levels with angular momentum m exist only if the radius of the dot is larger than the critical one, $R > R_m^{(cr)}$. For the conduction band, the critical radii for angular momentum $m = 0$, 1, and 2 are $R_0^{(cr)} = 15$ Å, $R_1^{(cr)} = 55$ Å, and $R_2^{(cr)} = 88.5$ Å. For the valence band, the corresponding critical radii are $R_0^{(cr)} = 53$ Å, $R_1^{(cr)} = 84$ Å, and $R_2^{(cr)} = 111.5$ Å.

The data shown in Fig. 3.2 illustrate that the quantum dot system does not have symmetry between the conduction and valence band energy spectra. The critical radii for conduction and valence band are also different.

In Fig. 3.3 the whole energy spectra are shown for four radii of TI quantum dot: 50

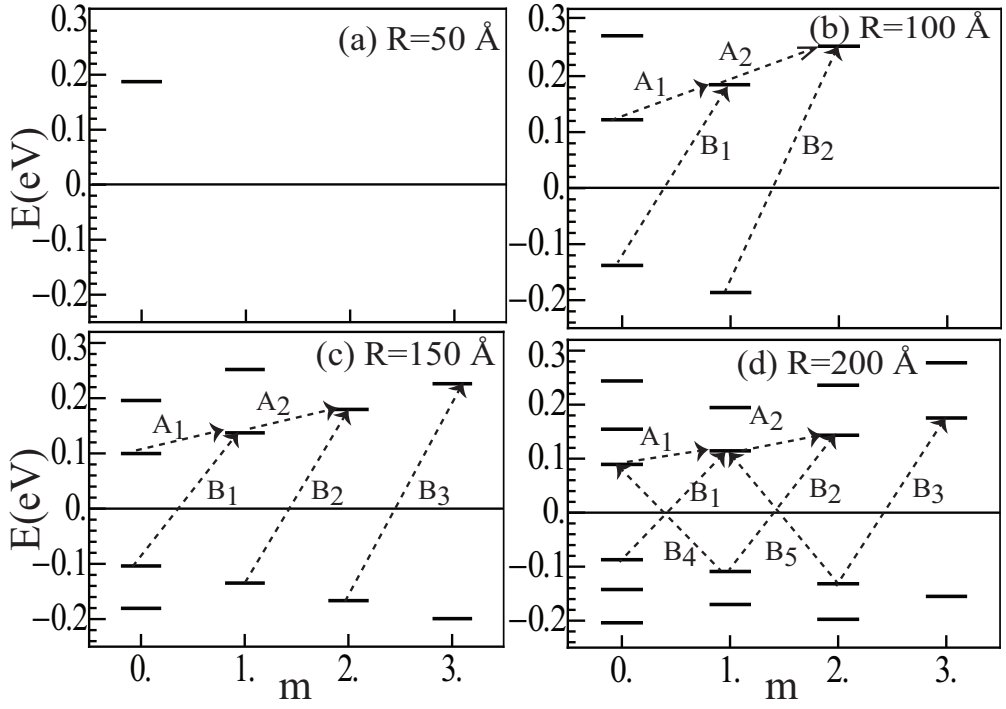

Figure (3.3) Energy spectra of TI quantum dot are shown as a function of angular momentum m for different radii R of quantum dot: (a) 50 Å, (b) 100 Å, (c) 150 Å, and (d) 200 Å. At $R = 50$ Å there is only one energy level in the conduction band. The dotted lines with arrows show the main intraband (labels by letters "A") and interband (labeled by letters "B") optical transitions.

Å, 100 Å, 150 Å and 200 Å. For a small quantum dot, $R = 50$ Å, there is only one energy level. This level belongs to the conduction band and has angular momentum $m = 0$, while no energy levels exist in the valence band. With increasing the size of the dot more levels appear both in the conduction band and in the valence band.

3.2.2 Optical transitions

We consider two types of optical transitions: (i) interband transitions between the states of valence and conduction bands and (ii) intraband optical transitions between the states of conduction band. In both cases we consider a non-interacting electron system, i.e., the TI quantum dot is occupied by a single electron, which can be in different initial (valence or conduction band) state. For interband and intraband optical transitions the selection rule, which is given by Eq. (3.11), is the same.

The main optical transitions with the largest intensities are shown by dashed lines in Fig. 3.3 for TI quantum dots of different radii. The interband transitions are labeled by letter A, while intraband transitions are labeled by letter B. The optical transitions mainly occur between the lowest energy states at a given angular momentum. Although other optical transitions are allowed by the selection rule, their intensities are small.

In Fig. 3.4 interband optical spectra are shown for different sizes of TI quantum dot. The spectra show multi-peak structure. The main transitions occur from the highest energy states at a given angular momentum, m_i, in the valence band to the lowest energy state at momentum $m_f = m_i + 1$ in the conduction band. The number of the peaks is equal to the number of different angular momentum cases in the valence band. For example, at $R = 100$ Å, the states in the valence band exist at only two different angular momentum, $m_i = 0$ and 1. In this case there are two main peaks B_1 and B_2 in the interband absorption spectra. Similarly, at $R = 200$ Å, there are three main peaks B_1, B_2, and B_3. There are also peaks B_4 and B_5, which have almost the same frequency as B_1 and B_2 but smaller intensity. The intensities of the peaks of the multi-peak absorption spectra decrease with increasing angular momentum of the initial state.

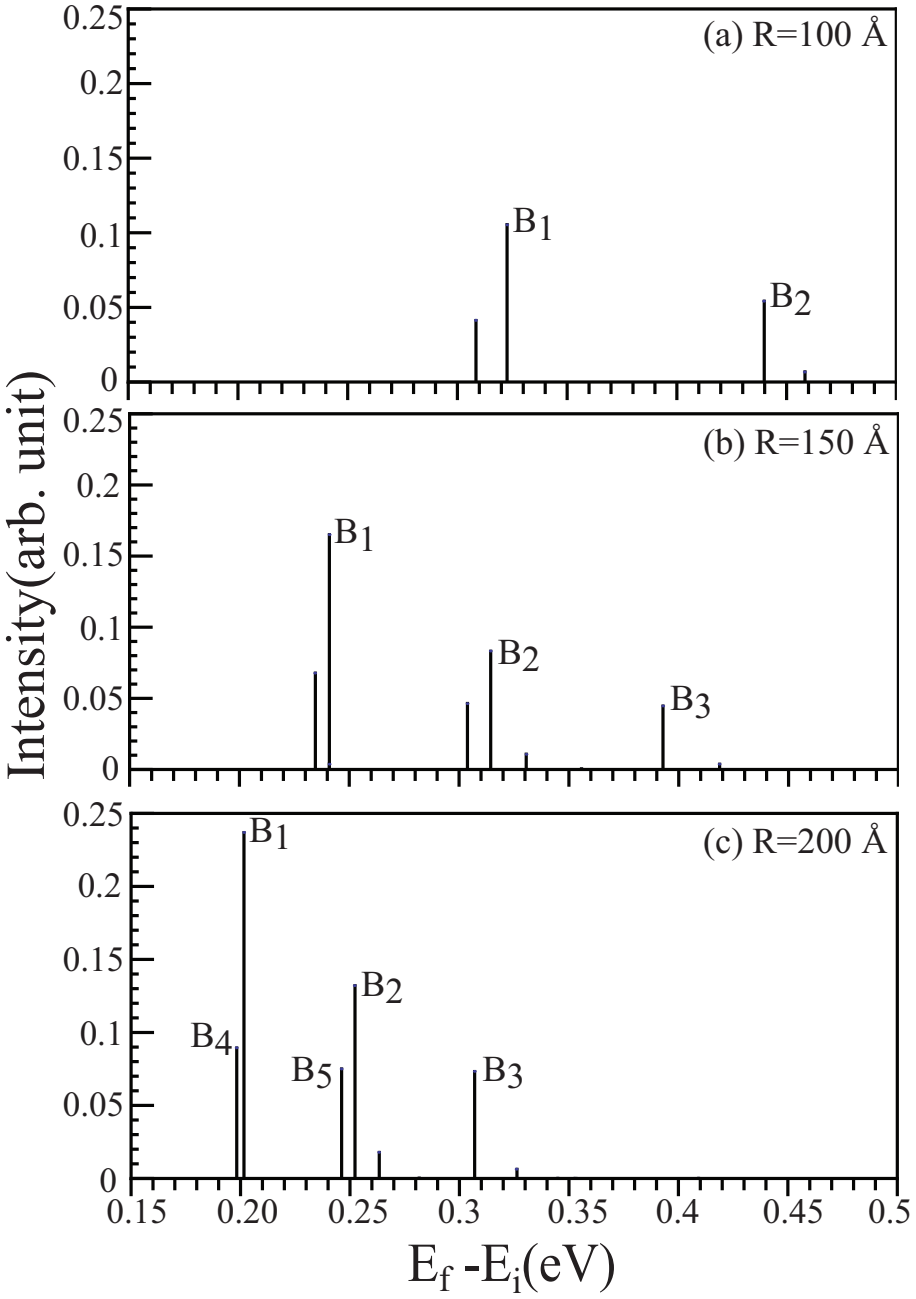

Figure (3.4) Absorption interband optical spectra are shown for different radii R of quantum dot: (a) 100 Å, (b) 150 Å, and (c) 200 Å. The labels of optical lines correspond to the labels of transitions in Fig. 3.3. The optical spectra have multi-peak structure.

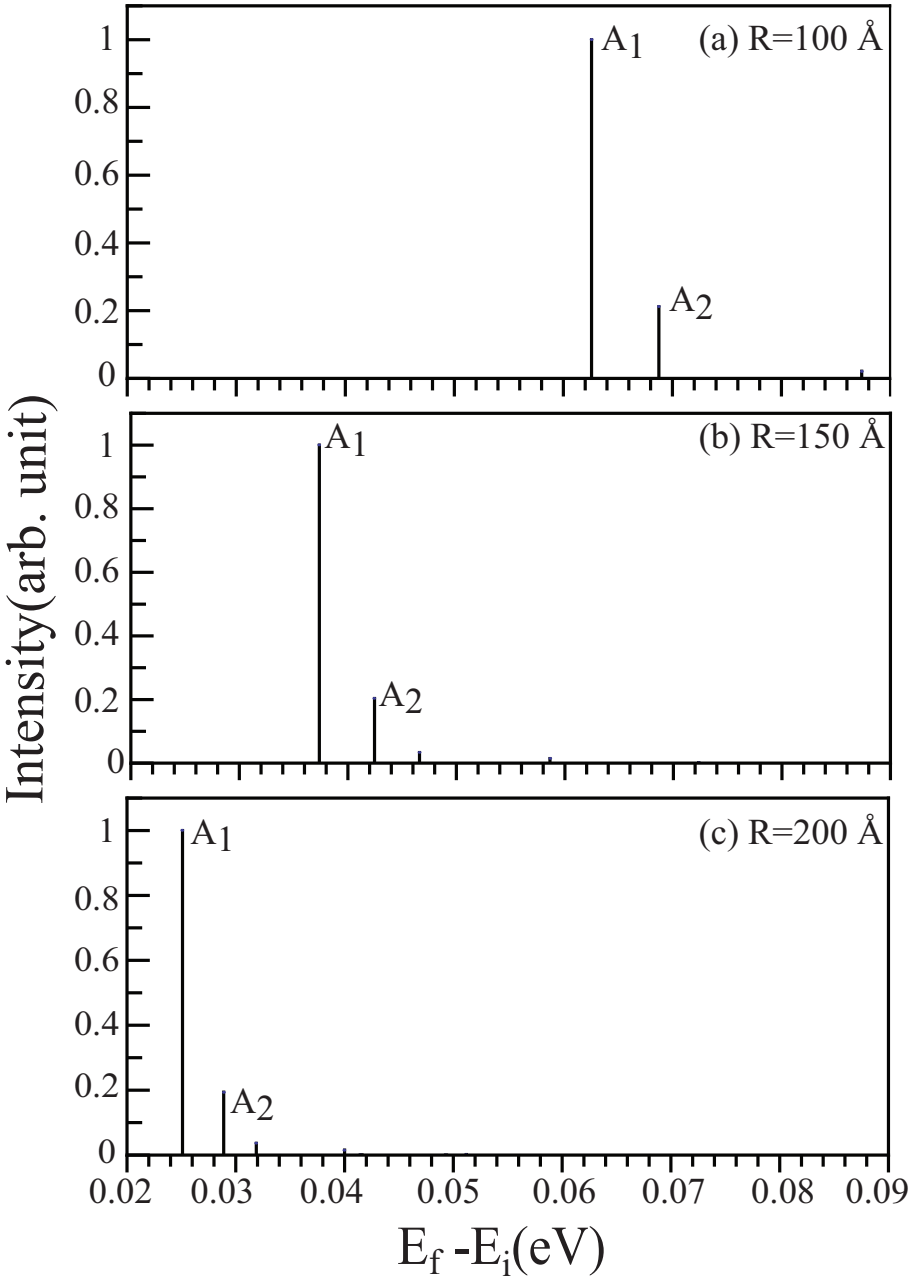

Figure (3.5) Absorption intraband optical spectra are shown for different radii R of quantum dot: (a) 100 Å, (b) 150 Å, and (c) 200 Å. The labels of optical lines correspond to the labels of transitions in Fig. 3.3. The optical spectra have one strong line with small satellites.

In Fig. 3.5 the intraband optical spectra are shown for three different quantum dot sizes 100 Å, 150 Åand 200 Å. The optical spectra consist of one main peak A_1, which corresponds to the transition from the lowest state in the conduction band with angular momentum $m_i = 0$ to the lowest state in the conduction band with angular momentum $m_f = 1$. There is also a higher energy satellite optical line A_2 with low intensity, which corresponds to the transition from the lowest state with $m_i = 1$ to the lowest state with $m_f = 2$. Thus, the intraband optical spectra have mainly a single peak structure with the frequency, which varies with the radius of quantum dot and is in the range of 30 - 70 meV.

3.2.3 Electron density

At a given value of pseudospin, for example, $\tau_z = 1$, the electron wave functions in TI quantum dot have two components, $\psi(\rho) = [\phi_1(\rho), \phi_2(\rho)]$ – see Eqs. (3.5)-(3.6). These two components correspond to two directions of electron spin, e.g., spin-up and spin-down. In this case we can introduce two characteristics of the wave function: spatial distributions of charge density and spin density. They are defined through the following expressions :

$$\Xi_{\text{charge}}(\rho) = |\psi_1(\rho)|^2 + |\psi_2(\rho)|^2, \tag{3.12}$$

for electron charge density and

$$\Xi_{\text{spin}}(\rho) = |\psi_1(\rho)|^2 - |\psi_2(\rho)|^2, \tag{3.13}$$

for electron spin density.

The electron charge density for a quantum dot of radius $R = 150$ Å is shown in Fig. 3.6 for the states with angular momentum $m = 0$ and 1. For each angular momentum the charge density is shown for two lowest energy states of the conduction band. The density profile shows the general tendency, which is expected for localized modes of semiconductor quantum dots. The density is finite at $\rho = 0$ only for the states with $m = 0$, while for $m > 0$ the electron density is zero at $\rho = 0$. With increasing energy of the state, the electron density

shows more oscillations and an electron becomes more localized near the center ($\rho = 0$) of the quantum dot.

The specific feature of a TI quantum dot is the existence of two waves in region $\rho < R$: propagating waves with a real wave vector and decaying waves with an imaginary wave vector. Similarly, in region $\rho > R$ there are also two waves, both of them are decaying waves. For the reflection of electron wave from a step-like defect at the surface of TI nanofilm, the existence of two types of waves results in enhancement of electron density near the step-like defect[1]. For the localized modes in TI quantum dots, as follows from Fig. 3.6, there is no any enhancement or any singularity near the boundary of quantum dot.

In regular semiconductor quantum dots without spin-orbit interaction, the charge and spin densities are equal to each other, $\Xi_{\text{charge}}(\rho) = \Xi_{\text{spin}}(\rho)$. With spin-orbit interaction the charge and spin densities are different [78, 79]. In topological insulators, it is a strong spin-orbit interaction that results in such unique gapless surface states. Therefore, in TI quantum dots, the spin-orbit interaction, which is already included implicitly in the effective Hamiltonian (3.1), is expected to be strong. In this case, the electron charge density and spin density should be strongly different. In Fig. 3.7 the electron spin density is shown for quantum dot of radius $R = 150$ Å for two lowest energy levels of conduction band with angular momentum $m = 0$. In Fig. 3.7(a) and (b) the electron spin density is shown for spin-up and spin-down, respectively. The data show that the electron density with spin-down is almost 6 times smaller than the corresponding density with spin-up. The spin density, which is shown in Fig. 3.7(c), is positive at almost all ρ points. Thus, in a TI quantum dot the spin-orbit interaction does not affect strongly the electron spin, and the electron has almost the same orientation of spin at all points within quantum dot. The spin density is also close to the charge density [see Fig. 3.6(a)].

3.3 Conclusion

The gap in the energy dispersion of surface states of TI can be opened for a TI nanofilm. The coupling of surface states at opposite boundaries of TI nanofilm introduces conduction

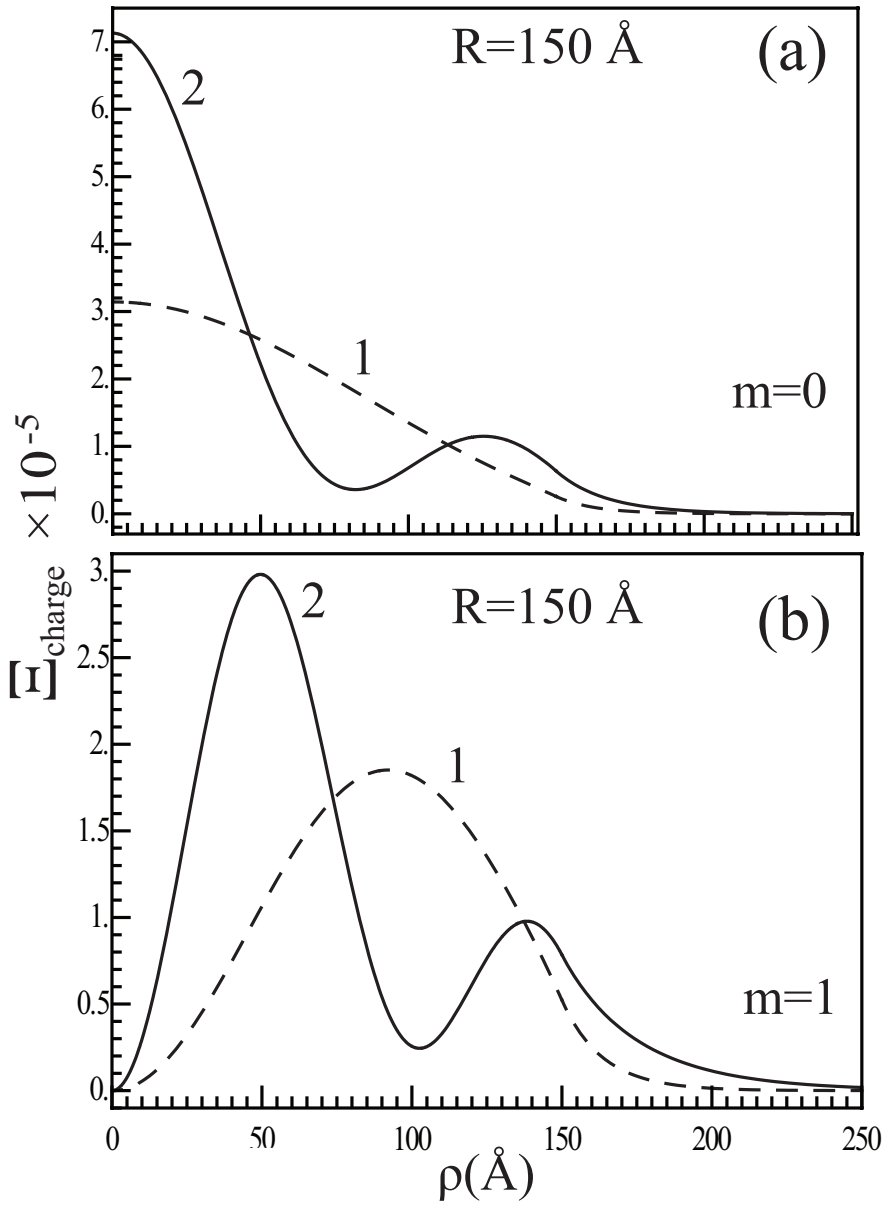

Figure (3.6) The electron charge density distribution is shown for quantum dot of radius 150 Å. The density is shown for conduction band states with angular momentum (a) $m = 0$ and (b) $m = 1$. The numbers "1" and "2" next to the lines correspond to the lowest energy state and the first excited state with a given angular momentum, respectively.

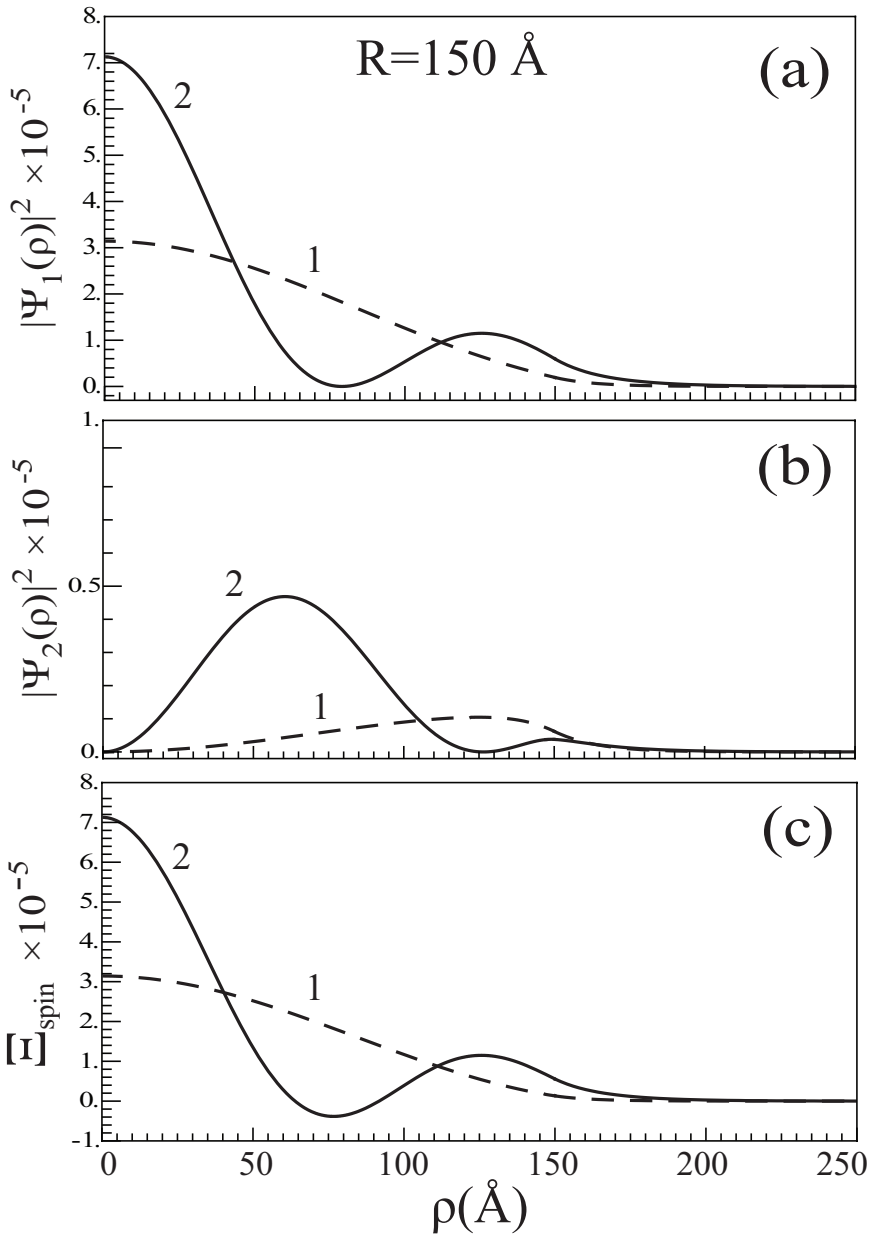

Figure (3.7) The electron density distribution is shown for quantum dot of radius 150 Å for two states with angular momentum $m = 0$. The numbers "1" and "2" next to the lines correspond to the lowest energy state and the first excited state, respectively. (a) The density of electron with spin-up, $|\psi_1(\rho)|^2$; (b) the density of electron with spin-down, $|\psi_2(\rho)|^2$; c) the electron spin density, $\Xi_{\text{spin}}(\rho)$.

and valence bands in the energy spectrum of TI nanofilm. The bands are separated by a bandgap, which is proportional to $1/L^2$. In this case the quantum dot can be realized as a region of nanofilm of a larger thickness. Such a quantum dot is characterized by its height and radius. The quantum dot can be grown experimentally by the droplet epitaxy method [80], which allows one to design nanostructures of different types. We calculated, within an effective model of TI nanofilm, an energy spectrum and optical transitions in a single-electron system of TI quantum dot.

The electron states are characterized by z-component of angular momentum, m. For each value of m, there is a critical size (radius) of quantum dot, which depends on the height of the quantum dot, so that the states with angular momentum m exist only in quantum dots with radius larger than the critical radius, $R^{(cr)}$.

The selection rule for the optical transitions is $\Delta m = \pm 1$, which is the same rule for both interband and intraband transitions. The interband optical absorption occur mainly between the lowest energy states of the valence and conduction bands with increasing angular momentum by 1. The interband absorption spectra have multi-peak structure with the number of peaks equal to the number of different angular momentum cases at which the states in the valence band exist.

The intraband absorption spectra consist of one main peak and small high frequency satellites. The main peak corresponds to optical transition between the lowest energy state with angular momentum $m = 0$ and the lowest energy state with angular momentum $m = 1$.

The charge and spin density distributions for electron states in a TI quantum dot show that electron spin has almost the same direction at all points inside the quantum dot. Thus the spin density almost coincides with the charge density.

CHAPTER 4

QUANTUM DOTS IN BUCKLED GRAPHENE-LIKE MATERIALS

The band gap of buckled graphene-like materials, such as silicene and germanene, depends on the external perpendicular electric field. Then specially design profile of electric field can produce trapping potential for electrons. We study theoretically the energy spectrum and optical transitions for such designed quantum dots in graphene-like materials. The energy spectra depend on the size of the quantum dot and applied electric field in the region of the quantum dot. The number of the states in the quantum dot increases with increasing the size of the dot and the energies of the states have almost linear dependence on the applied electric field with the slope which increases with increasing the dot size. The optical properties of the quantum dots are characterized by two type of absorption spectra: interband (optical transitions between the states of the valence and conduction bands) and intraband (transitions between the states of conduction/valence band). The interband absorption spectra have triple-peak structure with peak separation around 10 meV, while intraband absorption spectra, which depend on the number of electrons in the dot, have double-peak structure. The results are published in Journal of Physics : Condensed matter [3].

4.1 Model and Main equations

We design a silicene/germanene quantum dot by applying nonhomogeneous electric field perpendicular to silicene/germanene sheet. The quantum dot has cylindrical symmetry and its size is determined by radius R – see Fig. (4.1). Constant perpendicular electric field, E_{zi}, is applied to the inner region of the quantum dot, $\rho < R$, where $\rho = \sqrt{x^2 + y^2}$. Outside of this region, a weaker electric field, E_{zo} is applied. As illustrated in Fig. (4.1), if $E_{zo} < E_{zi}$, then such distribution of electric field generates a trapping potential, which can localize an

electron within the QD region, $\rho < R$. For concreteness, below we use the parameters of germanene [34] and study the germanene QDs. Qualitatively similar results are expected for selecene QDs.

The honeycomb lattice of germanene has a buckled structure, which consists of two sublattices A and B that are displaced vertically by finite distance l. Similar to graphene, the low energy spectrum of germanene is localized near two non-equivalent valleys, K and K'. Strong spin-orbit interaction in germanene opens a gap at K and K' points. Below we consider the energy spectrum and corresponding optical transitions for one valley, e.g., valley K, only. The results for valley K' will be exactly the same, i.e., the energy levels have double degeneracy and the intensities of all optical transitions should be multiplied by 2.

In the basis $(\phi_{A,\uparrow}, \phi_{B,\uparrow}, \phi_{A,\downarrow}, \phi_{B,\downarrow})$, where $\phi_{\eta,s}$ is the electron state of sublattice $\eta = A, B$ with spin $s =\uparrow, \downarrow$, the effective low energy model of germanene near the K valley is described by a 4×4 matrix Hamiltonian, which has the following form [32, 34]

$$\mathcal{H} = \begin{pmatrix} -\lambda_{so} + lE_z & \upsilon_F k_+ & ia\lambda_R k_- & 0 \\ \upsilon_F k_- & \lambda_{so} - lE_z & 0 & -ia\lambda_R k_- \\ -ia\lambda_R k_+ & 0 & \lambda_{so} + lE_z & \upsilon_F k_+ \\ 0 & ia\lambda_R k_+ & \upsilon_F k_- & -\lambda_{so} - lE_z \end{pmatrix}, \tag{4.1}$$

where $k_\pm = k_x \pm ik_y = e^{\pm i\varphi}(\pm\frac{1}{\rho}\partial_\varphi - i\partial_\rho)$ is the electron wave vector, expressed in polar coordinate system (ρ, φ), $\upsilon_F = \frac{\sqrt{3}}{2}at$ is the Fermi velocity, which can be expressed in terms of lattice constant $a = 4.13$Åand nearest neighbor transfer integral $t = 1.3 \times 10^3$meV. The transfer integral describes the hopping between the nearest neighbor sites of two sublattices A and B. Due to buckled structure of germanene, there is finite spin-orbit coupling, which is characterized by two constants $\lambda_{so} = 43$meV and $\lambda_R = 10.7$meV, where λ_R describes the spin-orbit interaction of Rashba type. Due to the finite relative shift of two sublattices A and B by distance $l = 0.33$Åin the z direction, there is sensitivity of the system to the perpendicular electric field E_z.

The energy spectrum of a germanene QD can be found from the solution of the

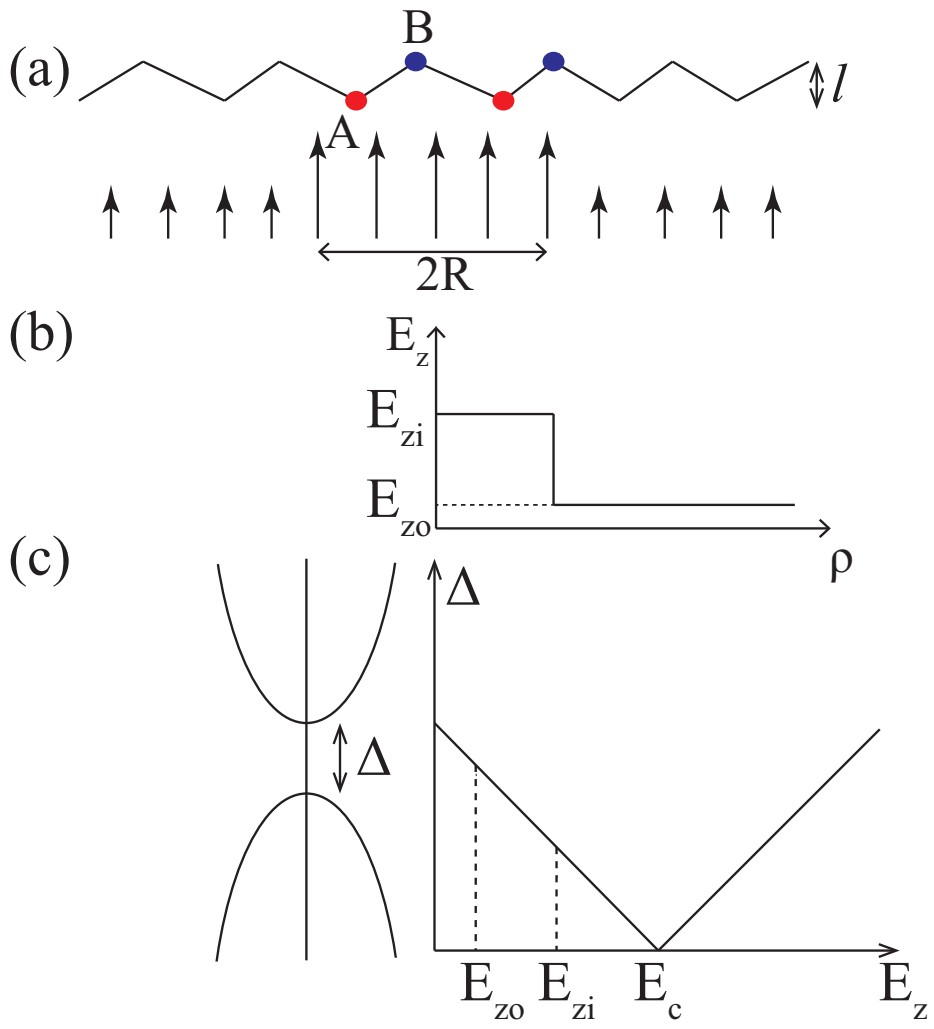

Figure (4.1) (a) Schematic illustration of silicene/germanene quantum dot. Two sublattices A and B of silicene/germanene are shifted in z-direction by distance l. The quantum dot has a shape of a circle with radius R. The quantum dot is created by applying nonhomogeneous electric field, which has different strength inside ($\rho < R$) and outside ($\rho > R$) quantum dot. Arrows show the direction and magnitude of applied electric field. (b) Magnitude of applied electric field as a function of polar coordinate ρ. (c) Band diagram of silicene/germanen monolayer. The band gap, Δ, depends on z component of electric field, E_z. Such dependence is shown schematically.

Schrödinger equation corresponding to the Hamiltonian (4.1) with electric field $E_z = E_{zi}$ at $\rho < R$ (region I) and $E_z = E_{zo}$ at $\rho > R$ (region II). Due to cylindrical symmetry of the system, the states of the QD are characterized by angular momentum m and the corresponding wavefunctions have the following form

$$\psi_\kappa = \begin{pmatrix} C_1(\kappa)J_m(\kappa\rho)e^{im\varphi} \\ C_2(\kappa)J_{m-1}(\kappa\rho)e^{i(m-1)\varphi} \\ C_3(\kappa)J_{m+1}(\kappa\rho)e^{i(m+1)\varphi} \\ C_4(\kappa)J_m(\kappa\rho)e^{im\varphi} \end{pmatrix}, \tag{4.2}$$

where C_1, C_2, C_3, C_4 are constant coefficients, the radial part of the wavefunction is expressed in terms of the Bessel functions of the first kind, J_m, and κ is the radial component of the wave vector. The radial component of the wave vector satisfies the following equation

$$\kappa^4\left(v^2+\lambda^2a^2\right)^2 + 2\kappa^2\left[(v^2+a^2\lambda^2)(\lambda_{SO}^2-E^2)+E_z^2l^2(v^2-a^2\lambda^2)\right] = E_z^4l^4 - 2E^2\lambda_{SO}^2 - (E^2-E_z^2l^2)^2 - (\lambda_{SO}^2+E_z^2l^2)^2 \tag{4.3}$$

where E is the energy of the state. At a given energy, E, there are 4 solutions of Eq. (4.3), i.e., 4 different values of wave vector κ. If the energy E is in the band gap, then all 4 wave vectors are imaginary, while if energy E is either in the conduction band or in the valence band then there are 2 real and 2 imaginary wave vectors κ. We are looking for electron states, which are localized within the QD region. In this case the energies of such states should be within the conduction or valence bands in region $\rho < R$ and within the band gap in region $\rho > R$. Under this condition, solution of the Schrödinger equation with eigenenergy E takes the following form

$$\Psi_{in}(\rho) = A_1\psi_{\kappa_1} + A_2\psi_{\kappa_2}, \tag{4.4}$$

in region $\rho < R$ and

$$\Psi_{out}(\rho) = B_1\psi_{\tilde{\kappa}_1} + B_2\psi_{\tilde{\kappa}_2}, \tag{4.5}$$

in region $\rho > R$. Here κ_1 is real and κ_2 is imaginary, while $\tilde{\kappa}_1$ and $\tilde{\kappa}_2$ are both imaginary. In the case of imaginary κ, the Bessel functions in Eq. (4.2) becomes modified Bessel functions of the second kind.

The continuity of the wavefunction (4.4)-(4.5), at $\rho = R$, i.e.,

$$\Psi_{in} \mid_{\rho=R_{+0}} = \Psi_{out} \mid_{\rho=R_{-0}}, \tag{4.6}$$

determines the energy spectrum of germanene QDs and corresponding coefficients A_1, A_2, B_1, and B_2. Below we study the dependence of QD energy spectrum on electric field E_{zi} (in region $\rho < R$) keeping electric field E_{zo} (in region $\rho > R$) constant.

In addition to energy spectra, we also study the interband (between the states of valence and conduction bands) and intraband (between the states of conduction band) optical transitions. For the light polarized along y-direction, the intensity of optical transitions between the states Ψ_i and Ψ_f is determined by the following expression

$$I_{if} \propto | < \Psi_i | \hat{v}_y | \Psi_f > |^2, \tag{4.7}$$

where the velocity operator, $\hat{v}_y$, defined as $v_y = \hbar^{-1} \partial \mathcal{H} / \partial k_y$ has the matrix form

$$\hat{v}_y = \begin{pmatrix} 0 & iv_F & a\lambda_R & 0 \\ -iv_F & 0 & 0 & -a\lambda_R \\ a\lambda_R & 0 & 0 & iv_F \\ 0 & -a\lambda_R & -iv_F & 0 \end{pmatrix}. \tag{4.8}$$

Selection rules for the optical transitions are

$$\Delta m = m_f - m_i = \pm 1, \tag{4.9}$$

where m_i and m_f are the angular momenta of states Ψ_i and Ψ_f, respectively. The selection rule (4.9) is valid for both interband and intraband optical transitions.

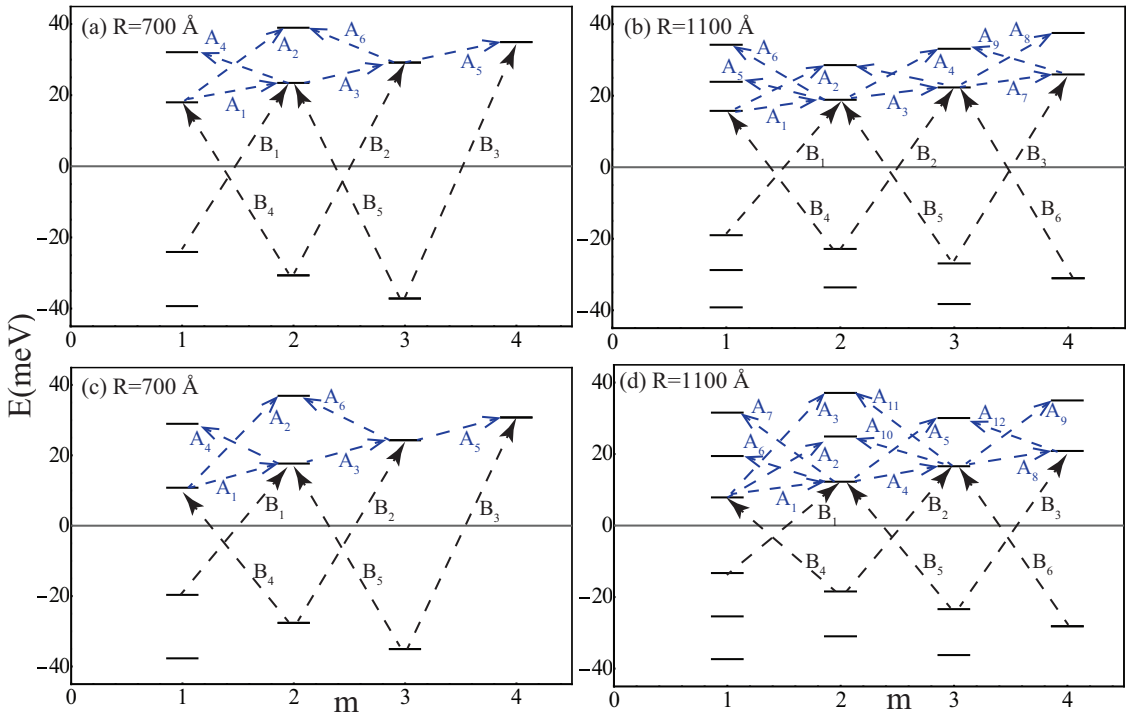

Figure (4.2) Energy spectra of the conduction (positive energies) band and the valence band (negative energies) of germanene quantum dot. The states are characterized by angular momentum m. The energy spectra are shown for different values of electric field in the region of quantum dot, E_{zi}, and different sizes of the quantum dot, R: (a) $R = 700$ Å, $E_{zi} = 90$ meVÅ^{-1}; (b) $R = 1100$ Å, $E_{zi} = 90$ meVÅ^{-1}; (c) $R = 700$ Å, $E_{zi} = 120$ meVÅ^{-1}; (d) $R = 1100$ Å, $E_{zi} = 120$ meVÅ^{-1}. The electric field outside quantum dot is $E_{zo} = 10$ meVÅ^{-1}. The arrows, labeled as A_i, show allowed intraband optical transitions between the states of the conduction band. The arrows, labeled as B_i, show allowed interband optical transitions between the states of the valence and conduction bands.

4.2 Results and Discussion

4.2.1 Energy spectrum

We fixed the electric field in the region outside the QD, i.e., $\rho > R$, at the value $E_{zo} = 10$ meV$\mathring{A}^{-1}$. Such a small electric field corresponds to large bandgap, 79.4 meV. At fixed E_{zo} we study the dependence of the energy spectrum both on electric field E_{zi} in the region of the QD, i.e., at $\rho < R$, and on the size of the QD. The corresponding electron states are characterized by electron angular momentum, m. The energy spectra corresponding to angular momentum $m = 1, 2, 3$ and 4 are shown in Fig.4.2 for two values of QD size, R, and two values of electric field E_{zi}.

The number of QD levels increases with increasing the size of the dot - see e.g. Fig.4.2(a) and (b), which is a general tendency of any nanoscale system. The number of localized states in the QD decreases with increasing electron angular momentum, which is due to the fact that localization region effectively decreases with increasing the angular momentum.

With increasing electric field E_{zi}, the band gap decreases, which increases the energy interval within which the electron state can be localized. In this case the number of QD states increases with E_{zi} - see Fig.4.2(b) and (d). The corresponding wave functions become also more localized with increasing E_{zi}. The energies of the corresponding levels also depend on the magnitude of E_{zi}. With increasing E_{zi} the energies decrease. The dependence of the energies on E_{zi} is shown in Fig. 4.3 for $m = 1$ states and different sizes of QD. The energies of the states decrease almost linearly with electric field E_{zi}. This dependence can be characterized by effective spreading of the wavefunction in z-direction. Such spreading is due to buckled structure of germanene with two sublattices shifted in z-direction by distance $l_z = 0.33$ Å. The wave functions of localized electron states in QD occupy two sublattices, resulting in spreading of the state in z-direction. The maximum spreading corresponds to inter-sublattice distance in z-direction, i.e. l_z. The width, l_{eff}, of the wave function in z-direction can be characterized by the value of the slope of energy of the state as a function of electric field, E_{zi}. In Fig. 4.3 the corresponding length, l_{eff}, is shown for different states

of the QD. The length, l_{eff}, changes from 0.12 Åto 0.31 Åand increases with decreasing the energy of the state. With increasing the QD size, R, the slope, i.e., characteristic length l_{eff}, increases, approaching asymptotically the value 0.33 Å, corresponding to intersubband separation in z-direction (see Fig. 4.3). For example, for the lowest energy state, length l_{eff} increases from 0.25 Åat $R = 400$ Åto 0.31 Åat $R = 1000$ Å.

For larger values of angular momentum (see Fig. 4.4, where the results for $m = 2$ are shown) the dependence of energies on electric field E_{zi} becomes weaker. The corresponding slope and characteristic length l_{eff} become smaller. For example, at $R = 700$ Å, while for $m = 1$ [see Fig. 4.3(c)] length l_{eff} is 0.26 Åfor the lowest energy states, it becomes 0.25 Åfor $m = 2$. Similar tendency is observed for other QD sizes, R.

4.2.2 Optical transitions

In Fig. 4.5 we shown the optical absorption spectra corresponding to interband optical transitions, assuming that in the initial state all the valence band states are occupied and all the conduction band states are empty. The selection rules for optical transitions are $m_f = m_i \pm 1$. The allowed optical transitions with the largest intensities are shown in Fig. 4.2 and labeled as B_i. The corresponding intensities of the optical absorption lines are shown in Fig. 4.5. The lines B_1, B_2, and B_3, which satisfy selection rule $m_f = m_i + 1$ (see Fig. 4.2), have the largest intensities. The typical energy of inter band optical transitions is around 50 meV.

The absorption spectra have a clear three-peak structure with inter-peak separation around 10 meV. The arrangement of the peaks by intensity changes with increasing the size of QD. At small QD radius, $R = 700$ nm [Fig. 4.5(a,c)], the high energy peak has the largest intensity, while at large QD radius, $R = 1000$ nm [Fig. 4.5(b,d)], the lowest energy peak has the largest intensity. The whole absorption spectrum is red-shifted with increasing the QD size. The inter-peak separation also decreases with increasing the dot radius.

The interband optical spectra show also the dependence on electric field E_{zi}, which is the field in the region of the QD. The spectra as whole are strongly red-shifted with increasing

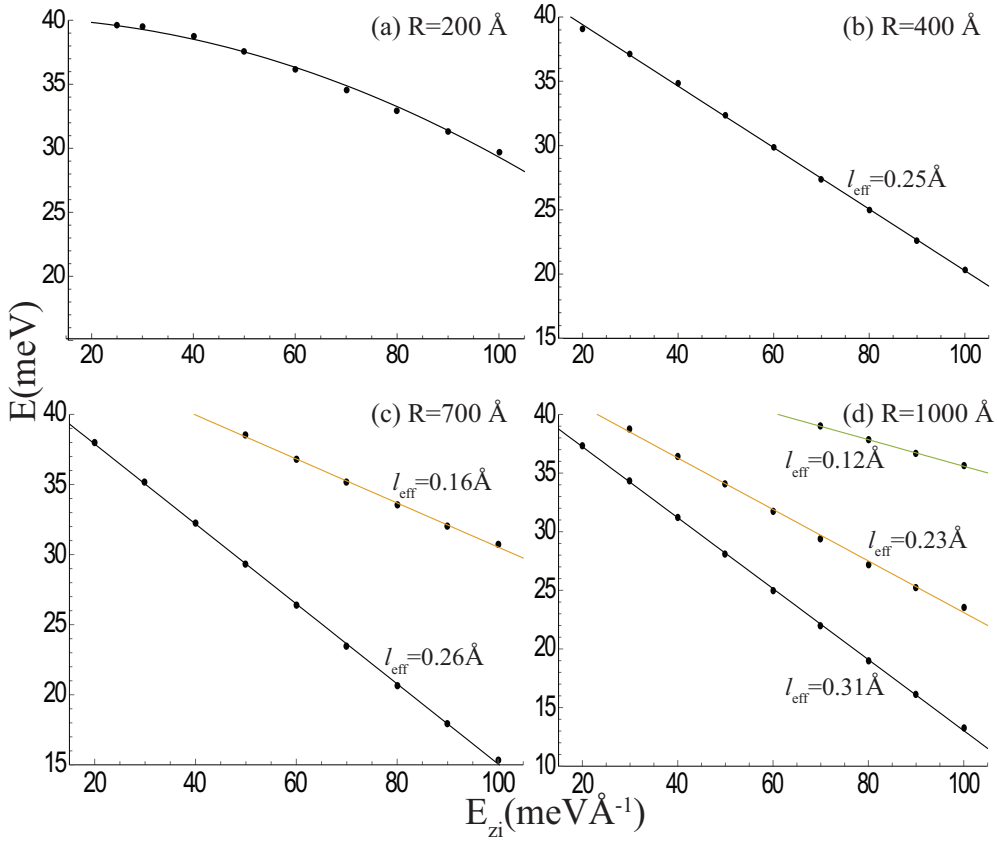

Figure (4.3) Energies of $m = 1$ levels as function of applied electric field E_{zi} in the region of quantum dot. The size of the quantum dot is (a) $R = 200$ Å, (b) $R = 400$ Å, (c) $R = 700$ Å, and (d) $R = 1000$ Å. The effective distance, l_{eff}, characterizes the slope of the corresponding line. The electric field in the region of the quantum dot is $E_{zi} = 90$ meVÅ^{-1}. The electric field outside quantum dot is $E_{zo} = 10$ meVÅ^{-1}.

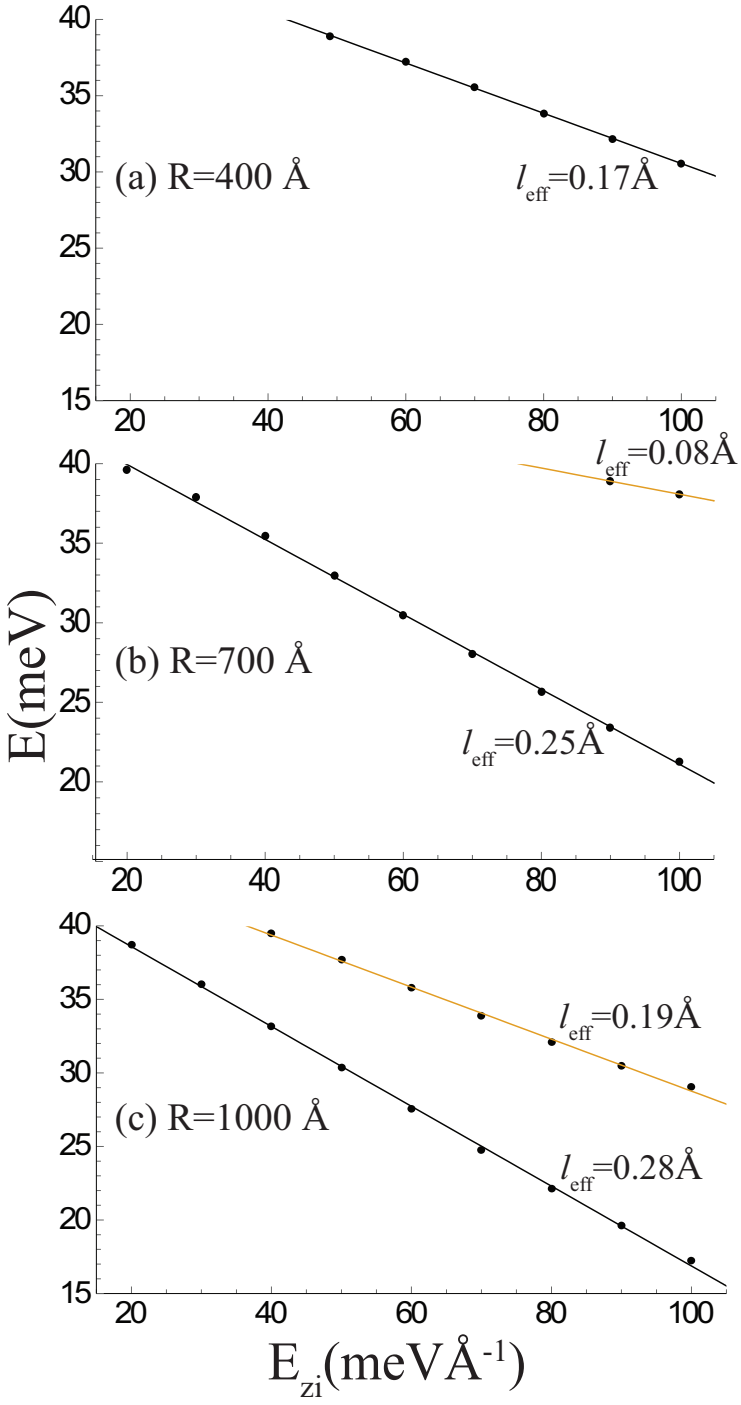

Figure (4.4) Energies of $m = 2$ levels as function of applied electric field E_{zi} in the region of quantum dot. The size of the quantum dot is (a) $R = 400$ Å, (b) $R = 700$ Å, and (c) $R = 1000$ Å. The effective distance, l_{eff}, characterizes the slope of the corresponding line. The electric field in the region of the quantum dot is $E_{zi} = 90$ meVÅ^{-1}. The electric field outside quantum dot is $E_{zo} = 10$ meVÅ^{-1}.

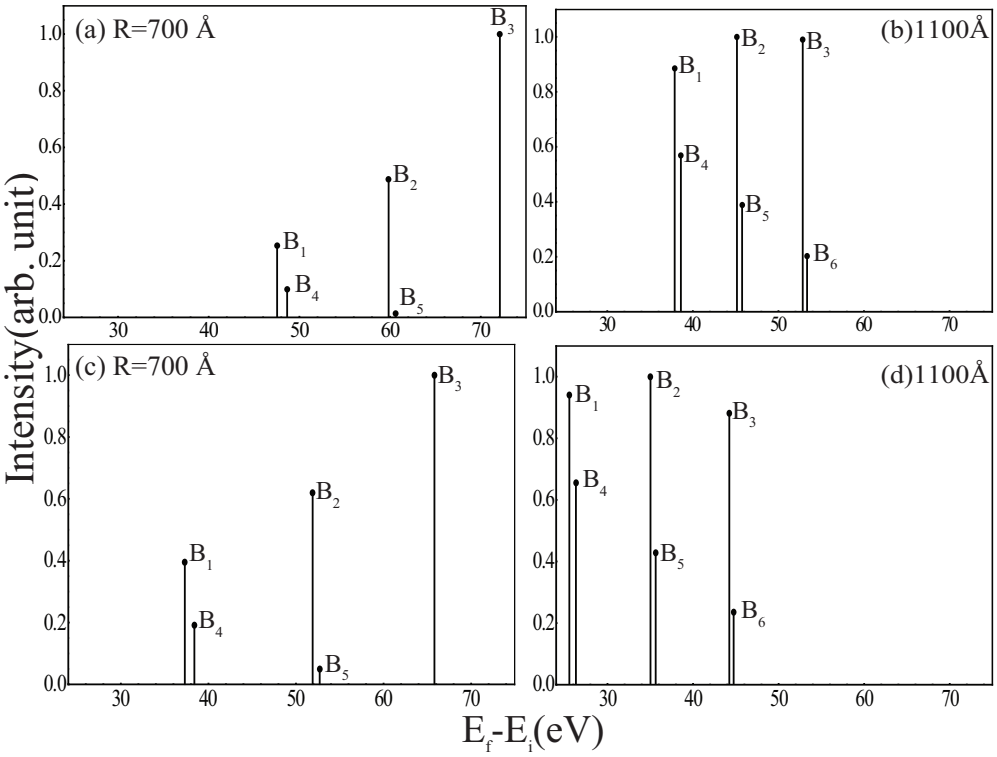

Figure (4.5) Absorption interband optical spectra. The radius, R, of the quantum dot the electric field, E_{zi}, in the region of the quantum dot are: (a) $R = 700$ Å, $E_{zi} = 90meV\mathring{A}^{-1}$ (b) $R = 1100$ Å, $E_{zi} = 90$ meVÅ^{-1} (c) $R = 700$ Å, $E_{zi} = 120$ meVÅ^{-1}, and (d) $R = 1100$ Å, $E_{zi} = 120$ meVÅ^{-1}. The electric field outside quantum dot is $E_{zo} = 10$meVÅ^{-1}. The labels, B_i, near the optical lines correspond to the labels of transitions shown in Fig. 4.2.

electric field E_{zi}, which is consistent with the behavior of the energy spectra shown in Fig. 4.2. Although the position of the spectra strongly depends on electric field E_{zi}, its structure, e.g., energy separations between peaks [see Fig. 4.5], has a weak dependence on E_{zi}.

In the case when the conduction band of the QD is partially occupied by electrons, there are also intraband optical transitions within the conduction band states. The allowed optical transitions, which have selection rule $m_f = m_i \pm 1$, are shown in Fig. 4.2. They are labeled as A_i. The actual absorption spectrum (optical transitions by Pauli exclusion principle) is determined by the number of electrons present in the QD, i.e., by the number of occupied states. For concreteness we consider only one spin polarization and assume that the QD can be occupied by $N_e = 1$, 2 or 3 electrons.

The corresponding absorption spectra are shown in Fig. 4.6 for two sizes of QD: $R = 700$ Åand 1100 Å. The electric field in the QD region is $E_{zi} = 120$ meV/Å. The typical frequency of intraband optical transitions is around 10-20 meV. The absorption spectra show a two-peak structure with separation between the peaks ≈ 15 meV. With increasing the size of the QD, the absorption spectra become red-shifted, while the energy separation between the peaks becomes smaller, i.e., the width of the absorption spectra decreases with increasing the dot size. With increasing the number of electrons in the QD, more absorption lines appear in the optical spectrum.

The above analysis of germanene QDs has been done for an ideal circular shape of the QD and a step-like profile of electric field. Deviation from such ideal structure results in shift of the optical lines or, in the system of many quantum dots, in finite broadening of the absorption lines. For example, for a germanene QD of radius 1100 Å, the variation of the dot size by 5% changes the energy of the intraband optical transitions by ≈ 2 meV (or introduces broadening of the absorption lines by ≈ 5 meV). For the interband transitions, the variation of the dot radius by 5% changes the position of the optical lines by ≈ 3 meV or introduces the broadening of the lines by 5%. This also means that if the boundary of the quantum dot is not sharp but smooth, i.e., the electric field changes from E_{zi} to E_{zo} within some range ΔR, then for $\Delta R/R \approx 0.05$ the position of the optical line changes from the sharp boundary value by ≈ 2 meV for intraband transitions and by ≈ 3 meV for interband transitions.

The electric field inside of the quantum dot is assumed to be constant. If the electric field E_{zi} is not a constant but varies within the dot, then the positions of the optical lines change compared to the case of constant electric field. For example, a 5% variation of the electric field shifts the intraband optical lines by ≈ 1.5 meV and interband optical lines by ≈ 4 meV.

Both graphene and silicene are grown on a substrate. The type of substrate determines the values of the parameters of the low energy Hamiltonian Eq.(4.1), i.e., the energy and optical spectra change quantitatively but not qualitatively with the type of substrate.

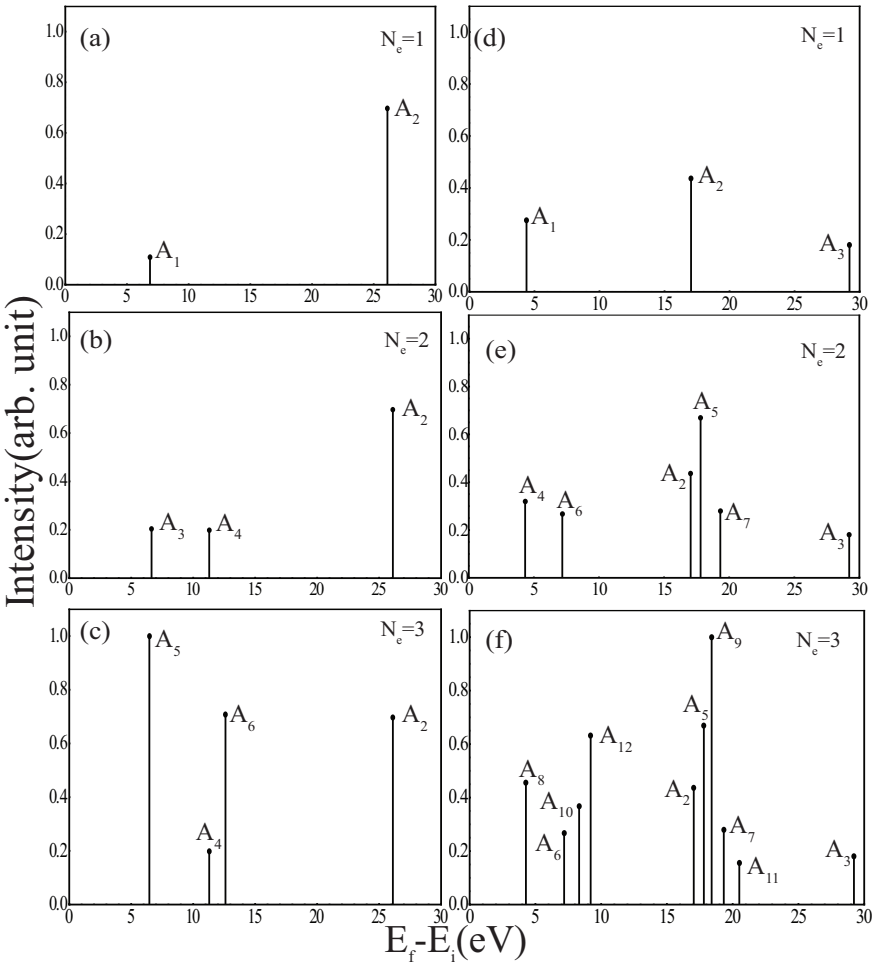

Figure (4.6) Absorption intraband optical spectra for different number of electrons in the quantum dot. The radius of the quantum dot is: (a),(b),(c) $R = 700$ Åand (d),(e),(f) $R = 1100$ Å. The electric field inside and outside quantum dot is $E_{zi} = 120$ meVÅ^{-1} and $E_{zo} = 10$ meVÅ^{-1}, respectively. N_e is the number of electrons in the quantum dot. The labels, A_i, near the optical lines correspond to the labels of transitions shown in Fig. 4.2.

4.3 Concluding remarks

The bandgap in buckled graphene-like materials, such as silicene and germanene, can be controlled by an external perpendicular electric field. In this case specially designed profile of electric field can produce a trapping potential, which forms a quantum dot of a finite size. The electrons are localized in the region of the QD. This is different from graphene monolayer, where the electron localization cannot be achieved for any confinement potential. In buckled graphene-like materials, if the electric field outside of the quantum dot is less than the electric field in the region of the dot then the electron can be localized within the quantum dot region. For a circular QD with radius R, the electron states in the QD are characterized by angular momentum, m. The energy spectra of silicene/germanene QDs depend on the size of the dot and on the magnitude of the electric field applied in the region of the QD. With increasing the size of the dot the number of localized energy states increases and correspondingly the interlevel energy separation decreases. The energies of the localized levels of QD almost linearly decrease with increasing the magnitude of electric field applied in the QD region. The dependence is the strongest for the lower energy levels, which are near the band edge.

There are two types of optical transitions in silicene/germanene quantum dots: interband (transitions between the states of conduction and valence bands) and intraband (transitions between the states of conduction/valence band) transitions. For both types of transitions the selection rule is formulated in terms of the change of angular momentum as $\Delta m = \pm 1$. The interband absorption spectra have triple peak structure with separation between the peaks around 10 meV. With increasing the size of the dot and increasing the applied electric field in the dot region, the absorption spectra becomes red-shifted. The strongest absorption lines correspond to condition $\Delta m = 1$. The intraband absorption spectra depend on the number of electrons in the dot and have a double-peak structure with separation between the peaks around 15 meV. With increasing the size of the dot, the intraband absorption spectra become red-shifted.

CHAPTER 5

ELECTRON CONFINEMENT IN BLACK PHOSPHORUS

We consider a phosphorene QD as a piece of phosphorene of a circular shape of radius R, placed on a substrate, see Fig. 5.1. First we find the energy spectrum and corresponding wave functions of such a QD. The spectrum consists of both conduction and valence band states. Then we calculate the corresponding absorption spectra for such a QD. Such spectra consist of both intraband and interband transitions.

The effective low-energy Hamiltonian of phosphorene can be obtained from **k.p** theory [69]. We assume that $R \gg a$. i.e., $\gamma k_x \gg \beta k_y^2$ and we neglect βk_y^2 in the Hamiltonian Eq. (1.21). The new effective Hamiltonian has the following form

$$\mathcal{H} = \begin{pmatrix} E_c + \eta_c k_x^2 + \nu_c k_y^2 & \gamma k_x \\ \gamma k_x & E_v - \eta_v k_x^2 - \nu_v k_y^2 \end{pmatrix}, \tag{5.1}$$

where E_c and E_v are the lowest energy of the conduction band and the highest energy of the valence band, respectively. Then the band gap is $\Delta = E_c - E_v \approx 2$eV. The band parameters $\eta_{c,v}$ and $\nu_{c,v}$ are related to the in-plane effective masses, and γ represents the coupling between the conduction and the valence bands. The parameters have the following values [72] : $\eta_{c,v} = \hbar^2/0.4m_0 = 19.0763$ eV Å^2, $\nu_c = \hbar^2/1.4m_0 = 5.4504$ eV Å^2, $\nu_v = \hbar^2/2.0m_0 = 3.8153$ eV Å^2, $\gamma = 4a/\pi = 2.8393$ eV Åand $a = 2.23$ Å. Here m_0 is the free electron mass.

5.1 Energy spectrum

It is convenient to rewrite the Hamiltonian $\mathcal{H}$ as the sum of two terms, $\mathcal{H}_0$ and $\mathcal{H}_\mathcal{I}$:

$$\mathcal{H} = \mathcal{H}_0 + \mathcal{H}_I, \tag{5.2}$$

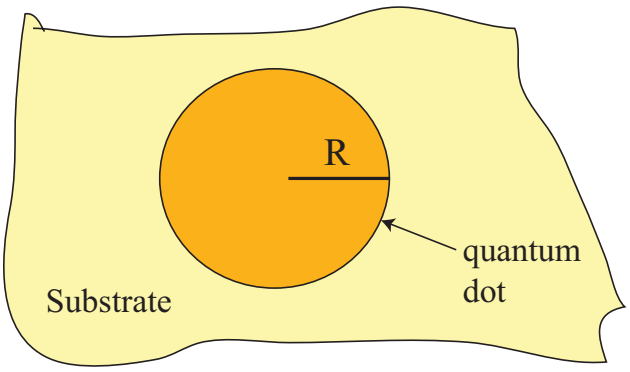

Figure (5.1) Monolayer black phosphorous quantum dot with radius R and thickness of one atomic layer.

where

$$\mathcal{H}_0 = \begin{pmatrix} E_c + \eta_c(k_x^2 + k_y^2) & 0 \\ 0 & E_v - \eta_v(k_x^2 + k_y^2) \end{pmatrix}, \tag{5.3}$$

and

$$\mathcal{H}_I = \begin{pmatrix} (\nu_c - \eta_c)k_y^2 & \gamma k_x \\ \gamma k_x & -(\nu_v - \eta_v)k_y^2 \end{pmatrix}. \tag{5.4}$$

First we find the eigenfunctions and eigenvalues of Hamiltonian $\mathcal{H}_0$:

$$\mathcal{H}_0\varphi_n = E_{0,n}\varphi_n. \tag{5.5}$$

The Hamiltonian $\mathcal{H}_0$ has azimuthal symmetry and the corresponding eigenfunctions φ_n can be characterized by the z-component of angular momentum. Using a finite number of φ_n as

a basis, we can expand eigenfunctions of the complete Hamiltonian $\mathcal{H}$ in terms of φ_n as

$$\begin{aligned} \psi_n &= \Sigma_j A_{nj}\varphi_j, & (5.6)\\ \text{Then}\mathcal{H}\psi_n &= E_n\psi_n, & (5.7)\\ (\mathcal{H}_0+\mathcal{H}_I)\Sigma_j A_{nj}\varphi_j &= E_n\Sigma_j A_{nj}\varphi_j. & (5.8) \end{aligned}$$

We multiply the right and left hand sides of Eq.(5.8) by φ_i and obtain

$$\begin{aligned} \varphi_i(\mathcal{H}_0+\mathcal{H}_I)\Sigma_j A_{nj}\varphi_j &= \varphi_i E_n\Sigma_j A_{nj}\varphi_j,\\ \varphi_i\mathcal{H}_0\Sigma_j A_{nj}\varphi_j+\varphi_i\mathcal{H}_I\Sigma_j A_{nj}\varphi_j &= \varphi_i E_n\Sigma_j A_{nj}\varphi_j,\\ \Sigma_j A_{nj}(E_0\delta_{i,j}+\mathcal{H}_{I,ij}) &= E_n A_{ni}, \end{aligned}$$

where $\mathcal{H}_{I,ij}=\varphi_i\mathcal{H}_I\varphi_j$.

Thus the Hamiltonian matrix in the basis of φ_i takes the form

$$\begin{aligned} H_{i,j} &= \varphi_j(\mathcal{H}_0+\mathcal{H}_I)\varphi_i\\ &= \varphi_j\mathcal{H}_0\varphi_i+\varphi_j\mathcal{H}_I\varphi_i\\ &= E_{0,i}\delta_{i,j}+H_{I,ij}. \end{aligned}$$

The eigenfunctions of the Hamiltonian $\mathcal{H}_0$ have the following form

$$\varphi_i^{(c)}(x,y)=\begin{pmatrix}\widetilde{\varphi}_{c,i}(x,y)\\ 0\end{pmatrix}, \qquad (5.9)$$

for conduction band states, and

$$\varphi_i^{(v)}(x,y)=\begin{pmatrix}0\\ \widetilde{\varphi}_{v,i}(x,y)\end{pmatrix}, \qquad (5.10)$$

for valance band states. The functions $\widetilde{\varphi}_{c,i}$ and $\widetilde{\varphi}_{v,i}$ satisfies the following eigenvalue equations

$$[E_c + \eta_c(k_x^2 + k_y^2)]\widetilde{\varphi}_{c,i}(x,y) = E_{c,i}\widetilde{\varphi}_{c,i}(x,y), \tag{5.11}$$

$$[E_v - \eta_v(k_x^2 + k_y^2)]\widetilde{\varphi}_{v,i}(x,y) = E_{v,i}\widetilde{\varphi}_{v,i}(x,y), \tag{5.12}$$

where $k_x^2 + k_y^2 = -\Delta = -\partial_x^2 - \partial_y^2$. In polar coordinates the above equations (5.11) and (5.12) become :

$$-\eta_c[\frac{1}{\rho}\frac{\partial}{\partial\rho}(\rho\frac{\partial}{\partial\rho}) + \frac{1}{\rho^2}\frac{\partial^2}{\partial\varphi^2}]\widetilde{\varphi}_{c,i}(\rho,\varphi) = (E_{c,i} - E_c)\widetilde{\varphi}_{c,i}(\rho,\varphi), \tag{5.13}$$

$$\eta_v[\frac{1}{\rho}\frac{\partial}{\partial\rho}(\rho\frac{\partial}{\partial\rho}) + \frac{1}{\rho^2}\frac{\partial^2}{\partial\varphi^2}]\widetilde{\varphi}_{v,i}(\rho,\varphi) = (E_{v,i} - E_v)\widetilde{\varphi}_{v,i}(\rho,\varphi). \tag{5.14}$$

We are looking for solutions of these equations in the form :

$$\widetilde{\varphi}_{c,i}(\rho,\varphi) = \chi_{c,i}(\rho)\mathrm{e}^{im\varphi}, \tag{5.15}$$

$$\widetilde{\varphi}_{v,i}(\rho,\varphi) = \chi_{v,i}(\rho)\mathrm{e}^{im\varphi}. \tag{5.16}$$

Then equations (5.13) and (5.14) become

$$\rho^2\frac{\partial^2\chi_{c,i}}{\partial\varphi^2} + \rho\frac{\partial\chi_{c,i}}{\partial\rho} + (\rho^2\kappa_{c,i}^2 - m^2)\chi_{c,i} = 0, \tag{5.17}$$

$$\rho^2\frac{\partial^2\chi_{v,i}}{\partial\varphi^2} + \rho\frac{\partial\chi_{v,i}}{\partial\rho} + (\rho^2\kappa_{v,i}^2 - m^2)\chi_{v,i} = 0, \tag{5.18}$$

where we introduce parameters $\kappa_{c,i}^2$ and $\kappa_{v,i}^2$ as

$$E_{c,i} = E_c + \eta_c\kappa_{c,i}^2,$$

$$E_{v,i} = E_v - \eta_v\kappa_{v,i}^2.$$

The solutions of Eqs.(5.17) and (5.18) are Bessel functions of the first kind :

$$\chi_{c,i}(\rho) \sim J_m(\kappa_{c,i}\rho), \tag{5.19}$$

$$\chi_{v,i}(\rho) \sim J_m(\kappa_{v,i}\rho). \tag{5.20}$$

We consider hard wall boundary conditions, which means that the wave function is zero at $\rho = R$. This leads to

$$J_m(\kappa_{c,i}R) = J_m(\kappa_{v,i}R) = 0. \tag{5.21}$$

Then

$$\kappa_{c,i} = \frac{\alpha_{m,i}}{R}, \tag{5.22}$$

$$\kappa_{v,i} = \frac{\alpha_{m,i}}{R}, \tag{5.23}$$

where $\alpha_{m,i}$ is the i-th zero of J_m, i.e., $J_m(\alpha_{m,i}) = 0$. For example, for $m = 0$, $\alpha_{0,i}$ are $2.40, 5.52, 8.65, 11.79, 14.93$ and so on. The first few zeros for $m = 1$ are at $3.83, 7.02, 10.17, 13.32, 16.47$. Then the wave function of the electron in the i-th energy state in the conduction and valance bands can be written as

$$\widetilde{\varphi}_{c,i} = C_i J_m(\kappa_{c,i}\rho)\exp(im\varphi), \tag{5.24}$$

$$\widetilde{\varphi}_{v,i} = C_i J_m(\kappa_{v,i}\rho)\exp(im\varphi), \tag{5.25}$$

where the C_is are normalization constants. Then the conduction band and the valence band energy spectra of the Hamiltonian $\mathcal{H}_0$ are

$$E_{c,i} = E_c + \eta_c(\frac{\alpha_{m,i}}{R})^2, \tag{5.26}$$

$$E_{v,i} = E_v - \eta_v(\frac{\alpha_{m,i}}{R})^2. \tag{5.27}$$

The energy band of phosphorene is $2eV$, then below we choose $E_c = 2$ eV and $E_v = 0$ eV. In our numerical analysis we consider the lowest 20 energy levels per each band. For a QD of radius 5 nm, they are in the energy range of [-1.3 eV,3.3 eV] and are shown in Fig. 5.2. This energy range varies with the quantum dot size. These lowest states form the basis in our calculations. Then, within this basis, we calculate the Hamiltonian matrix of the full Hamiltonian, $\mathcal{H}_0 + \mathcal{H}_I$. The Hamiltonian matrix has the following structure:

$$\mathcal{H} = \begin{pmatrix} H^{cc} & H^{cv} \\ H^{vc} & H^{vv} \end{pmatrix}, \tag{5.28}$$

where $H^{cc}, H^{cv}, H^{vc}, H^{vv}$ are 20×20 matrices and $H^{vc} = (H^{cv})^\dagger$. These matrices can be found from the following expressions:

$$\begin{aligned}
H^{cc}_{ii} &= E_{c,i}, \\
H^{cc}_{ij} &= \int_0^R \int_0^{2\pi} \varphi^*_{c,i}(\rho,\varphi)\mathcal{H}_I\varphi_{c,j}(\rho,\varphi)\, d\varphi\rho\, d\rho, \qquad i \neq j, \\
H^{vv}_{ii} &= E_{v,i} \\
H^{vv}_{ij} &= \int_0^R \int_0^{2\pi} \varphi^*_{v,i}(\rho,\varphi)\mathcal{H}_I\varphi_{v,j}(\rho,\varphi)\, d\varphi\rho\, d\rho, \qquad i \neq j, \\
H^{cv}_{ij} &= \int_0^R \int_0^{2\pi} \varphi^*_{c,i}(\rho,\varphi)\mathcal{H}_I\varphi_{v,j}(\rho,\varphi)\, d\varphi\rho\, d\rho.
\end{aligned}$$

The matrix elements between the energy levels of the conduction band, H^{cc}_{ij}, and levels of the valance band, H^{vv}_{ij}, are non-zero only if $m_j = m_i \pm 2$, where m_i and m_j are the angular momenta of states i and j, respectively. The matrix elements between the conduction band and the valance band states, H^{vc}_{ij}, are non-zero only if $m_j = m_i \pm 1$. Here m_i and m_j are the angular momenta of the i and j states in the conduction and valence bands, respectively. The Hamiltonian matrix elements H^{cc}_{ij} and H^{vv}_{ij} have the following form :

$$\begin{aligned}
H^{cc}_{ij} = & -C_iC_j\pi(\nu_c - \eta_c)\int_0^R J_{m_i}(\kappa_i\rho)\left[\frac{m_j}{\rho^2}(1\pm 1)J_{m_j}(\kappa_j\rho) - \frac{m_j^2}{\rho^2}(1\pm 1)J_{m_j}(\kappa_j\rho)\right. \\
& \left. -\frac{\kappa_{c,j}}{\rho}(1\mp m)J_{m_j+1}(\kappa_j\rho) + \frac{\kappa^2_{c,j}}{2}J_{m_j}(\kappa_j\rho)\right]\rho\, d\rho,
\end{aligned} \tag{5.29}$$

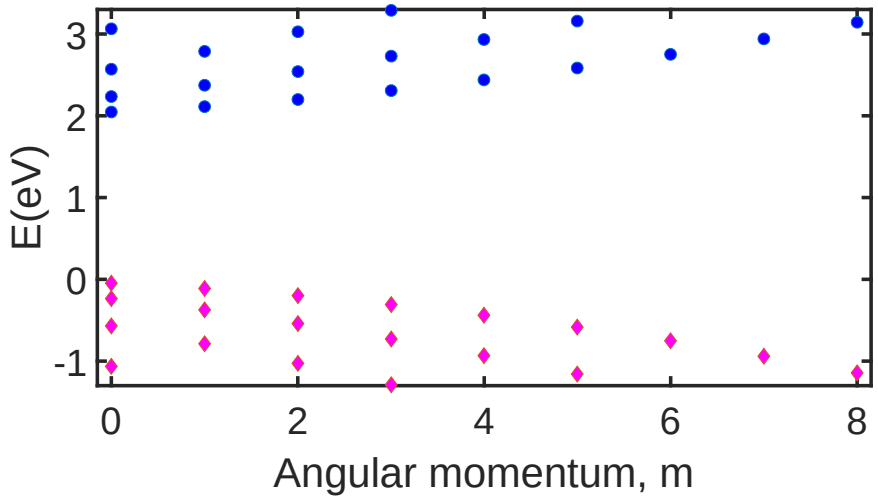

Figure (5.2) Energy spectrum of Hamiltonian $\mathcal{H}_0$ as a function of angular momentum. The positive energies correspond to the CB and the negative energies correspond to the VB.

$$H_{ij}^{vv} = C_i C_j \pi(\nu_v - \eta_v) \int_0^R J_{m_i}(\kappa_i \rho) \left[\frac{m_j}{\rho^2}(1 \pm 1) J_{m_j}(\kappa_j \rho) - \frac{m_j^2}{\rho^2}(1 \pm 1) J_{m_j}(\kappa_j \rho) - \frac{\kappa_{v,j}}{\rho}(1 \mp m) J_{m_j+1}(\kappa_j \rho) + \frac{\kappa_{v,j}^2}{2} J_{m_j}(\kappa_j \rho) \right] \rho \, d\rho. \quad (5.30)$$

Here the $'+'$ sign corresponds to $m_j = m_i + 2$ and the $'-'$ sign corresponds to $m_j = m_i - 2$. The Hamiltonian matrix element, H_{ij}^{vc} is

$$H_{ij}^{vc} = i\gamma\pi C_i C_j \int_0^R J_{m_i}(\kappa_i \rho) \left[\frac{m_j}{\rho}(\mp 1 - 1) J_{m_j}(\kappa_j \rho) + \kappa_{c,j} J_{m_j+1}(\kappa_j \rho) \right] \rho \, d\rho. \quad (5.31)$$

Here the $'-'$ sign corresponds to $m_j = m_i + 1$ and $'+'$ sign corresponds to $m_j = m_i - 1$. By diagonalizing the matrix $\mathcal{H}$, we can obtain the eigenvalues and corresponding eigenfunctions of the full Hamiltonian. Then the corresponding wave functions of an electron in a phosphorene QD is

$$\psi_n = \sum_{j=1}^{20} A_{nj} \varphi_j^c + \sum_{j=21}^{40} A_{nj} \varphi_{j-20}^v, \quad (5.32)$$

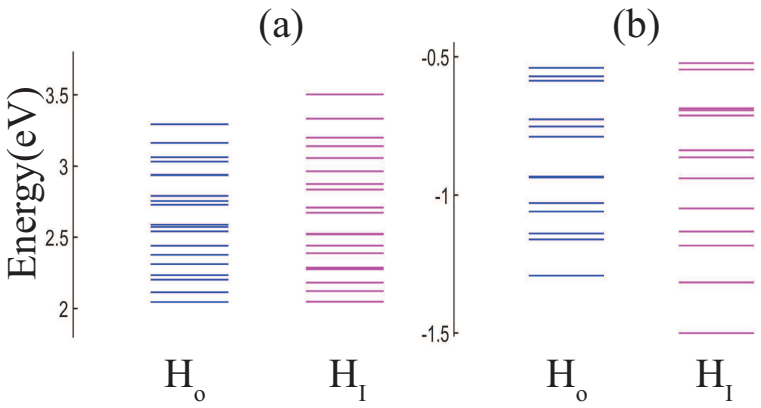

Figure (5.3) Complete energy spectrum of (a) the conduction band and (b) the valance band. Each plot contains energy levels corresponding to Hamiltonian $\mathcal{H}_0$ and total Hamiltonian $\mathcal{H}$.

where A_{nj} is the n-th eigenfunction of the Hamiltonian matrix (5.28). The complete energy spectrum of a phosphorus QD is shown in Fig. 5.3 for R=5 and 10 nm. The energy spectrum of $\mathcal{H}_0$ is also shown in Fig. 5.3. We see that for full Hamiltonian $\mathcal{H}$ the inter-level energy separation is larger than for Hamiltonian $\mathcal{H}_0$.

5.2 Intranband and Interband optical transitions

There are two types of optical transitions in phosphorene quantum dots. The intraband optical transitions correspond to electron transitions between the states of the conduction band. If an electron is excited to conduction band from valance band, the corresponding transition is the interband optical transition. Below we neglect the electron-electron interactions. We calculate optical transitions for x and y polarized light. For y-polarized light, the optical transitions are determined by the matrix elements of the corresponding velocity operator as

$$I_{ij}^{y} = \psi_i \hat{v_y} \psi_j{}^2, \tag{5.33}$$

where

$$\hat{v_y} = \frac{1}{\hbar}\frac{\partial \mathcal{H}}{\partial k_y} \tag{5.34}$$

$$= \frac{2}{\hbar}\begin{pmatrix} \nu_c k_y & \beta k_y \\ \beta k_y & -\nu_v k_y \end{pmatrix} \tag{5.35}$$

$$= -\frac{2}{\hbar}\begin{pmatrix} \nu_c \partial_y & \beta \partial_y \\ \beta \partial_y & -\nu_v \partial_y \end{pmatrix}, \tag{5.36}$$

is the velocity operator. We substitute Eq. (5.32) into Eq. (5.33) and obtain

$$I_{ij}^{y} = \Big| \sum_{k=1}^{20}\sum_{p=1}^{20} A_{ik}^{*}A_{jp}\varphi_k^c \hat{v_y}\varphi_p^c + \sum_{k=1}^{20}\sum_{p=21}^{40} A_{ik}^{*}A_{jp}\varphi_k^c \hat{v_y}\varphi_{p-20}^v + \sum_{k=21}^{40}\sum_{p=1}^{20} A_{ik}^{*}A_{jp}\varphi_{k-20}^v \hat{v_y}\varphi_p^c + \sum_{k=21}^{40}\sum_{p=21}^{40} A_{ik}^{*}A_{jp}\varphi_{k-20}^v \hat{v_y}\varphi_{p-20}^v \Big|^2 . \tag{5.37}$$

With the known basis eigenfunctions φ_i^c and φ_j^v, see Eqs. (5.9) and (5.10), the matrix elements of the velocity operator can be found from the following expressions :

$$\begin{aligned} \varphi_k^c \hat{v_y}\varphi_p^c &= \frac{2\pi}{\hbar}\nu_c C_k C_p \kappa_{pc}\int_0^R J_{m_k}(\kappa_k\rho)J_{m_k}(\kappa_p\rho)\rho\, d\rho, \\ \varphi_k^v \hat{v_y}\varphi_p^v &= -\frac{2\pi}{\hbar}\nu_v C_k C_p \kappa_{pv}\int_0^R J_{m_k}(\kappa_k\rho)J_{m_k}(\kappa_p\rho)\rho\, d\rho, \\ \varphi_k^c \hat{v_y}\varphi_p^v &= \frac{2\pi}{\hbar}\beta C_k C_p \kappa_{pv}\int_0^R J_{m_k}(\kappa_k\rho)J_{m_k}(\kappa_p\rho)\rho\, d\rho. \end{aligned} \tag{5.38}$$

Here $m_p = m_k \pm 1$. In the above expressions we calculated the integral over angle, φ.

For x-polarized light, the optical transitions are calculated as

$$I_{ij}^{x} = \psi_i \hat{v_x} {\psi_j}^2, \tag{5.39}$$

where

$$\hat{v_x} = \frac{1}{\hbar}\frac{\partial \mathcal{H}}{\partial k_x} \tag{5.40}$$

$$= \frac{1}{\hbar}\begin{pmatrix} 2\eta_c k_x & \gamma \\ \gamma & -2\eta_v k_x \end{pmatrix}, \tag{5.41}$$

is the x-component of the velocity operator. We substitute Eq. (5.32) into Eq. (5.39) and obtain

$$I_{ij}^{x} = \Big| \sum_{k=1}^{20}\sum_{p=1}^{20} A_{ik}^{*}A_{jp}\varphi_k^c \hat{v_x}\varphi_p^c + \sum_{k=1}^{20}\sum_{p=21}^{40} A_{ik}^{*}A_{jp}\varphi_k^c \hat{v_x}\varphi_{p-20}^v + \sum_{k=21}^{40}\sum_{p=1}^{20} A_{ik}^{*}A_{jp}\varphi_{k-20}^v \hat{v_x}\varphi_p^c + \sum_{k=21}^{40}\sum_{p=21}^{40} A_{ik}^{*}A_{jp}\varphi_{k-20}^v \hat{v_x}\varphi_{p-20}^v \Big|^2 . \tag{5.42}$$

The matrix elements of the velocity operator between the basis functions are

$$\begin{aligned} \varphi_k^c \hat{v_x}\varphi_p^c &= \mp\frac{2\pi i}{\hbar}\eta_c C_k C_p \kappa_{pc}\int_0^R J_{m_k}(\kappa_k\rho)J_{m_k}(\kappa_p\rho)\rho\, d\rho, \\ \varphi_k^v \hat{v_x}\varphi_p^v &= \pm\frac{2\pi i}{\hbar}\eta_v C_k C_p \kappa_{pv}\int_0^R J_{m_k}(\kappa_k\rho)J_{m_k}(\kappa_p\rho)\rho\, d\rho, \end{aligned} \tag{5.43}$$

where $m_p = m_k \pm 1$, and

$$\varphi_p^v \hat{v_x}\varphi_k^c = \varphi_k^c \hat{v_x}\varphi_p^v = \frac{2\pi}{\hbar}\gamma C_k C_p \int_0^R J_{m_k}(\kappa_k\rho)J_{m_k}(\kappa_p\rho)\rho\, d\rho,$$

where $m_p = m_k$.

The intraband optical transitions exist between the conduction band states only when the conduction band is partially occupied. The intraband optical absorption spectra for the y-polarized light is shown in Fig. 5.4 for quantum dot of radius R= 5 nm (blue lines) and 10 nm (red lines). The spectra have a single peak structure. The intensity of the peak becomes smaller when the size of the dot is increased. The spectrum is also red shifted when we increase the quantum dot size. Figures 5.4 (a), (b), (c), (d) and (e) show intraband optical

spectra for 1, 3, 5, 7 and 9 electrons in the dot, respectively. The number of electrons in the QD is counted by taking into account the Pauli exclusion principle. The frequency of the photon increases till it has 7 electrons and then decreases. The relative intraband optical spectra for x-polarized light is illustrated in Fig. 5.5. Similar to the intraband spectra for y-polarized light, the peak intensity decreases as the quantum dot size increases. Nevertheless we see multipeak structure for intraband spectra for x-polarized light. Due to the highly anisotropic properties of phosphorene, the intraband optical transitions are sensitive to the light polarization. The comparison of the intraband optical transition for x- and y-polarizations is shown in Fig. 5.6. The intensity of optical transitions for x-polarized light is ~ 10 times larger than the corresponding intensity for y-polarized light.

The interband optical transitions from the valence band to the conduction band for different radii of QD are shown in Fig. 5.7. They have a multipeak structure with many allowed transitions. To show such spectra it is convenient to introduce the Lorentzian broadening for each line. The optical spectra in this case are described by the following expression :

$$I(\Delta E) = \Sigma_i I_i \frac{1}{\pi} \frac{\Gamma/2}{(\Delta E - \Delta E_i)^2 + (\Gamma/2)^2}, \tag{5.44}$$

where ΔE is the photon energy, I_i and ΔE_i are intensity and energy corresponding to absorption line i, and Γ is the broadening. We use $\Gamma = 0.01$ and $\Gamma = 0.02$ for x and y polarized light respectively.

The intensity of interband optical transition for x-polarized light is 1000 times higher than the corresponding intensity for y-polarized light. Each plot in Fig. 5.7 is normalized for illustration purposes. The width of optical spectra depends on the size of the QD. As the dot size increases the width decreases - see Fig. 5.7.

Interband optical transitions for x and y polarized light are shown in Fig. 5.8 for R=5 nm. The intensity of interband optical spectrum for x-polarized light is 1000 times larger than the corresponding intensity for y-polarized light. The data also show that the first moment of the absorption spectrum (central frequency of the spectrum) increases when the

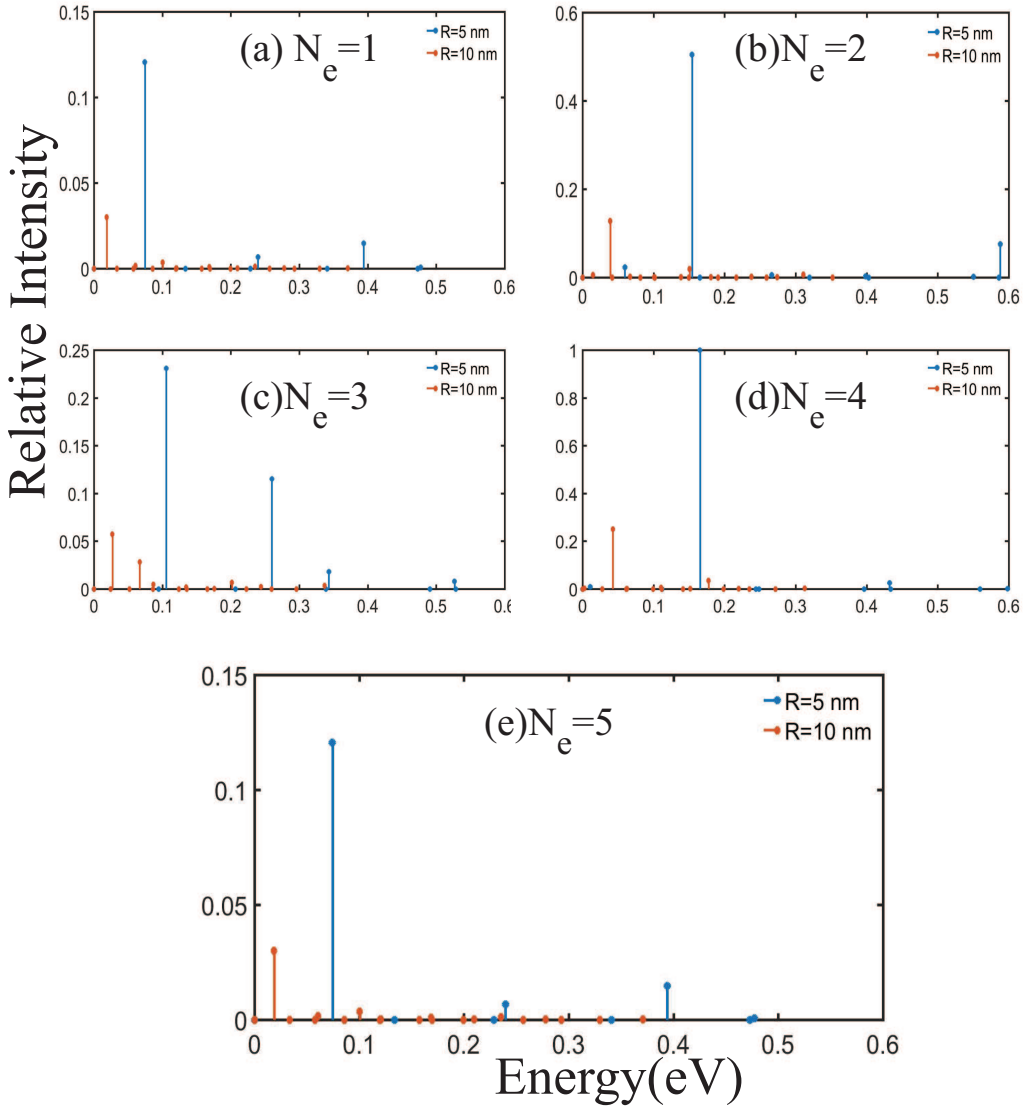

Figure (5.4) Intraband optical transitions for y-polarized light of monolayer black phosphorous quantum dot with radius R=5 nm and 10 nm. The intraband transitions are shown for (a) 1 electron, (b) 2 electrons, (c) 3 electrons, (d) 4 electrons and (5) 5 electrons in the QD. Here N_e is the number of electrons.

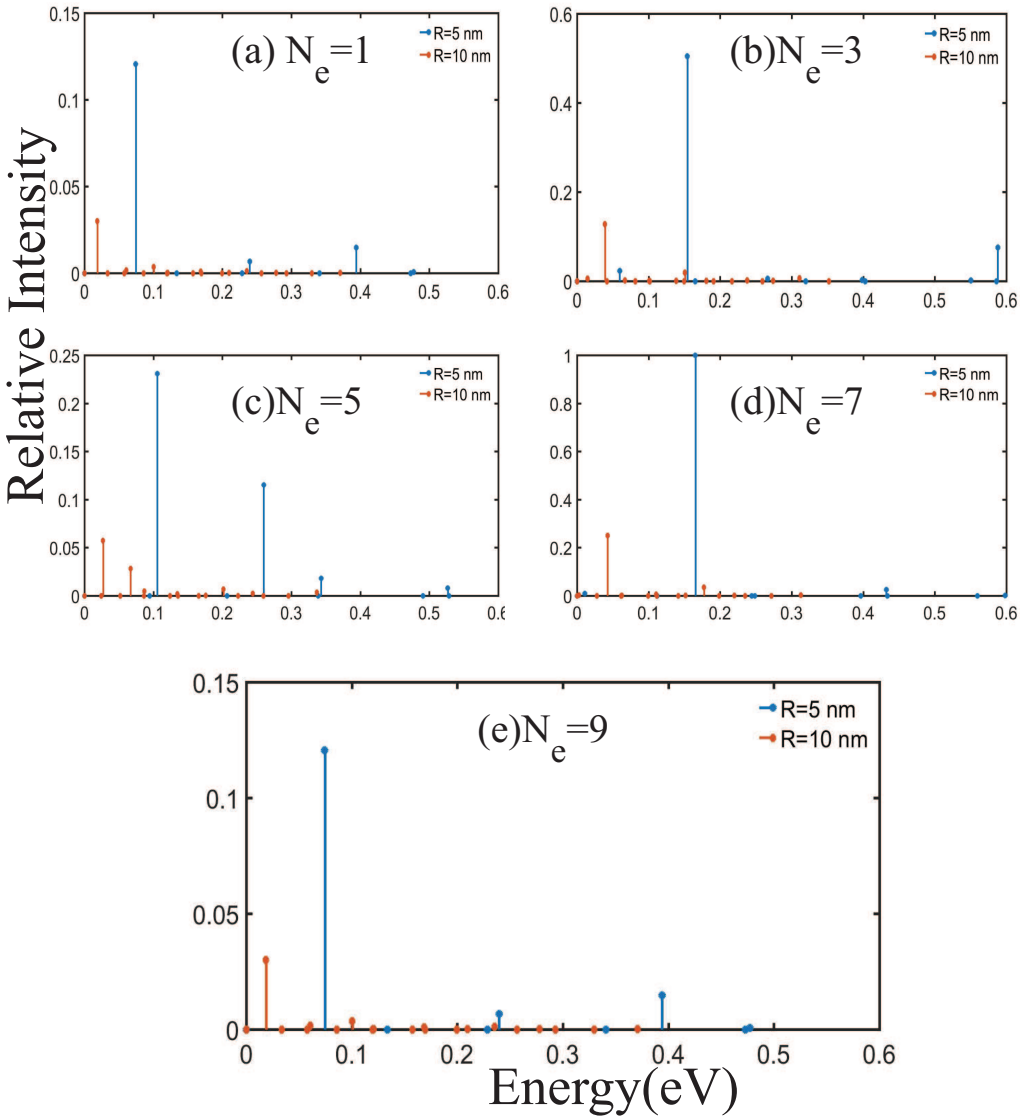

Figure (5.5) Intraband optical transitions for x-polarized light of monolayer black phosphorous quantum dot with radius R=5 nm and 10 nm. The intraband transitions are shown for (a) 1 electron, (b) 2 electrons, (c) 3 electrons, (d) 4 electrons and (e) 5 electrons in the QD. Here N_e is the number of electrons.

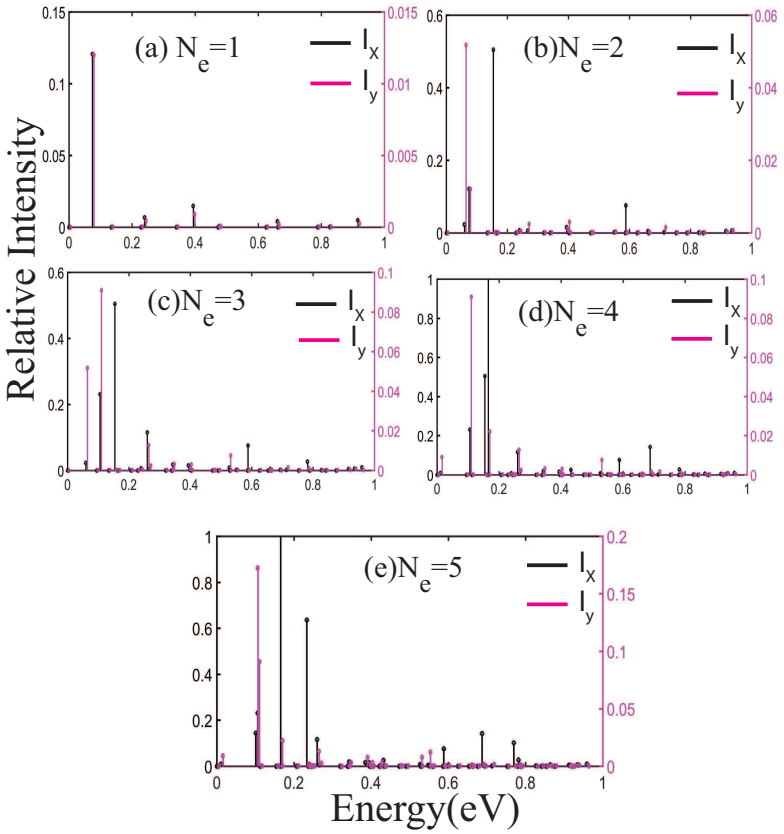

Figure (5.6) Intraband optical transitions of QD for x-polarized light and y-polarized light. The radius of QD is 5nm. The number of electron in QD is (a) 1 electron, (b) 2 electrons, (c) 3 electrons, (d) 4 electrons and (e) 5 electrons.

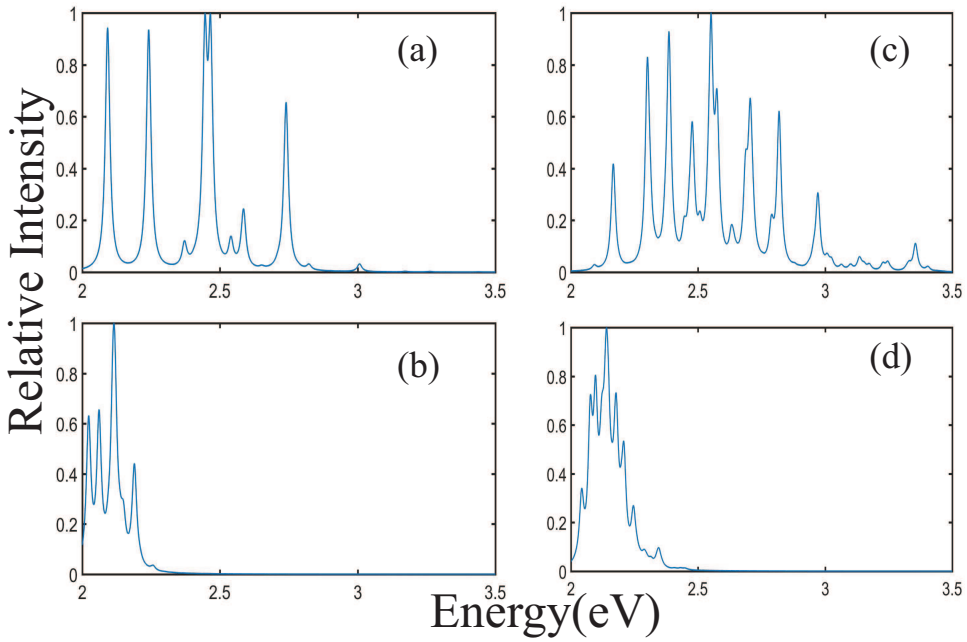

Figure (5.7) Interband optical transitions in phosphorous QD. The spectra are shown for (a) x-polarized light and QD of radius 5 nm, (b) x-polarized light and QD of radius 10 nm, (c) y-polarized light and QD of radius 5 nm, (d) y-polarized light and QD of radius 10 nm.

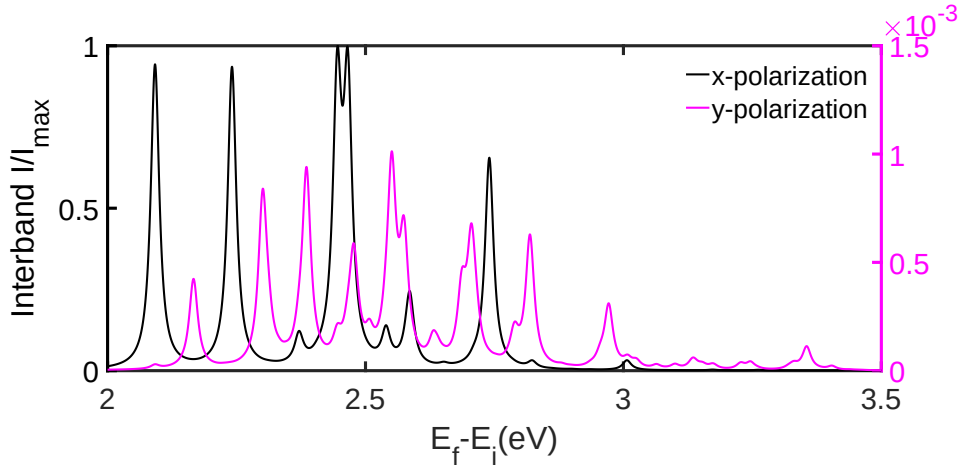

Figure (5.8) Interband optical transitions for x-polarized (black line) and y-polarized (dashed color line) light in a phosphorene QD. The radius of the QD is 5nm.

polarization of light changes from x to y.

CHAPTER 6

CONCLUSIONS

6.1 Conclusions

Scientists have started to pay great attention to two-dimensional materials after significant success in studies of graphene. Graphene has remarkable electronic, mechanical and thermal properties. However, its zero band gap limits its applications in real world devices. Recently, scientists have found a few remarkable 2D materials such as ultrathin topological insulator nanofilm, silicene, germanene and phosphorene. Due to their finite band gap, they are good candidates for quantum dots. The applications of quantum dots range from solar cells, FETs, quantum computing to medical applications. In this thesis, I have studied energy spectra and optical transitions of quantum dots in these 2D materials.

The surfaces of topological insulators are metallic. If the thickness of TI film is in the range of nano-scale, the states at the two surfaces on the opposite sides of the film are coupled, which opens a gap in the energy dispersion, i.e., TI nanofilm has a gapped energy dispersion. The energy band gap depends on the thickness of the nanofilm, as $\Delta_g \sim 1/L^2$. One of the natural defects in TI nanofilm system is a step-like defect, which is characterized by different thicknesses of the nanofilm in different regions. The electron propagating through the step-like defect in a TI nanofilm produces not only transmitted and reflected waves, but also localized modes. Due to these localized modes, there is a high electron density near the boundary of a step like defect. This electron density depends on the parameters of the TI nanofilm and the size of the step like defect. By introducing step-like defects in TI nanofilm, one can manipulate the local electron density at the surface of the nanofilm.

As TI nanofilm is a gapped system, electron confinement is possible. Such confinement can be realized, for example, in a cylindrical quantum dot. The energy levels in such a QD are characterized by z-component of angular momentum, m. I study the energy spectrum

of a TI quantum dot and optical transitions within the QD, both interband and intraband optical transitions. The selection rule for optical transitions is $\Delta m = \pm 1$. The interband optical transitions show multipeak structure, while the intraband transitions show a single peak structure.

The QD can be also introduced in graphene-like materials such as silicene or germanene. They have a buckled structure due to their heavy atoms. The buckled structure creates two sub-lattices, and an external electric field perpendicular to the sheet is able to change the band gap. By applying a spatially dependent electric field, we can create a trapping potential for electrons, i.e., a quantum dot. I studied the energy spectrum and optical transitions in such a quantum dot. The number of energy states linearly depends on the applied electric field and the size of the dot. The interband transitions between the valence band and the conduction band show a triple-peak structure, while the intraband spectra have a double-peak struture. Moreover the optical spectra depend on the number of trapped electrons.

Another type of QD, which has been discussed in the thesis, is a QD in monolayer black phosphorous. Black phosphorous is the most stable allotrope of phosphorus with interesting properties such as a gap of $1.5 - 2$ eV around the Γ point and high carrier mobility, etc. The energy gap depends on the thickness of the phosphorene sheet. Due to finite energy band gap, electron confinement by a piece of phosphorene sheet is possible. I created a QD by considering a cylindrical isolated piece of a monolayer phosphorene of size $\sim$ 10nm. I studied both the energy and optical absorption spectra of such QDs. Due to highly anisotropic properties of phosphorene, the absorption spectra strongly depend on light polarization. The intensities of intraband optical transitions are comparable for x and y polarized light, while the intensity of interband transitions for x-polarized light is 1000 times larger than for y-polarized light. Moreover, interband spectra for x-polarized light show triple-peak structure while the spectra have a single peak for y-polarized light.

REFERENCES

[1] T. M. Herath, P. Hewageegana, and V. Apalkov, "Electron scattering by a steplike defect in topological insulator nanofilms," *Physical Review B*, vol. 87, no. 7, p. 075318, 2013.

[2] ——, "A quantum dot in topological insulator nanofilm," *Journal of Physics: Condensed Matter*, vol. 26, no. 11, p. 115302, 2014.

[3] T. M. Herath and V. Apalkov, "Energy spectra and optical transitions in germanene quantum dots," *Journal of Physics: Condensed Matter*, vol. 28, no. 16, p. 165301, 2016.

[4] A. M. Smith and S. Nie, "Semiconductor nanocrystals: structure, properties, and band gap engineering," *Accounts of chemical research*, vol. 43, no. 2, pp. 190–200, 2009.

[5] T. Chakraborty, *Quantum Dots: A survey of the properties of artificial atoms*. Elsevier, 1999.

[6] J. S. Bunch, Y. Yaish, M. Brink, K. Bolotin, and P. L. McEuen, "Coulomb oscillations and hall effect in quasi-2d graphite quantum dots," *Nano letters*, vol. 5, no. 2, pp. 287–290, 2005.

[7] H.-Y. Chen, V. Apalkov, and T. Chakraborty, "Fock-darwin states of dirac electrons in graphene-based artificial atoms," *Physical review letters*, vol. 98, no. 18, p. 186803, 2007.

[8] P. Hewageegana and V. Apalkov, "Electron localization in graphene quantum dots," *Physical Review B*, vol. 77, no. 24, p. 245426, 2008.

[9] A. C. Neto, F. Guinea, N. M. Peres, K. S. Novoselov, and A. K. Geim, "The electronic properties of graphene," *Reviews of modern physics*, vol. 81, no. 1, p. 109, 2009.

[10] D. Abergel, V. Apalkov, J. Berashevich, K. Ziegler, and T. Chakraborty, "Properties of graphene: a theoretical perspective," *Advances in Physics*, vol. 59, no. 4, pp. 261–482, 2010.

[11] L. Fu and C. L. Kane, "Topological insulators with inversion symmetry," *Physical Review B*, vol. 76, no. 4, p. 045302, 2007.

[12] L. Fu, "L. fu, cl kane, and ej mele, phys. rev. lett. 98, 106803 (2007)." *Phys. Rev. Lett.*, vol. 98, p. 106803, 2007.

[13] D. Hsieh, "D. hsieh, d. qian, l. wray, y. xia, ys hor, rj cava, and mz hasan, nature (london) 452, 970 (2008)." *Nature (London)*, vol. 452, p. 970, 2008.

[14] Y. Chen, "Yl chen, jg analytis, j.-h. chu, zk liu, s.-k. mo, xl qi, hj zhang, dh lu, x. dai, z. fang, sc zhang, ir fisher, z. hussain, and z.-x. shen, science 325, 178 (2009)." *Science*, vol. 325, p. 178, 2009.

[15] Y. Xia, D. Qian, D. Hsieh, L. Wray, A. Pal, H. Lin, A. Bansil, D. Grauer, Y. S. Hor, R. J. Cava *et al.*, "Observation of a large-gap topological-insulator class with a single dirac cone on the surface," *Nature physics*, vol. 5, no. 6, p. 398, 2009.

[16] D. Hsieh, Y. Xia, D. Qian, L. Wray, J. Dil, F. Meier, J. Osterwalder, L. Patthey, J. Checkelsky, N. Ong *et al.*, "A tunable topological insulator in the spin helical dirac transport regime," *Nature*, vol. 460, no. 7259, p. 1101, 2009.

[17] D. Hsieh, Y. Xia, L. Wray, D. Qian, A. Pal, J. Dil, J. Osterwalder, F. Meier, G. Bihlmayer, C. Kane *et al.*, "Observation of unconventional quantum spin textures in topological insulators," *Science*, vol. 323, no. 5916, pp. 919–922, 2009.

[18] T. Xu, H. Wu, J. Si, and P. McCann, "Optical transitions in pb te/ cd te quantum dots," *Physical Review B*, vol. 76, no. 15, p. 155328, 2007.

[19] H. P. Paudel and M. N. Leuenberger, "Three-dimensional topological insulator quantum dot for optically controlled quantum memory and quantum computing," *Physical Review B*, vol. 88, no. 8, p. 085316, 2013.

[20] H.-Z. Lu, W.-Y. Shan, W. Yao, Q. Niu, and S.-Q. Shen, "Massive dirac fermions and spin physics in an ultrathin film of topological insulator," *Physical review B*, vol. 81, no. 11, p. 115407, 2010.

[21] W.-Y. Shan, H.-Z. Lu, and S.-Q. Shen, "Effective continuous model for surface states and thin films of three-dimensional topological insulators," *New Journal of Physics*, vol. 12, no. 4, p. 043048, 2010.

[22] A. Kara, H. Enriquez, A. P. Seitsonen, L. L. Y. Voon, S. Vizzini, B. Aufray, and H. Oughaddou, "A review on silicenenew candidate for electronics," *Surface science reports*, vol. 67, no. 1, pp. 1–18, 2012.

[23] P. Vogt, "P. vogt, p. de padova, c. quaresima, j. avila, e. frantzeskakis, mc asensio, a. resta, b. ealet, and g. le lay, phys. rev. lett. 108, 155501 (2012)." *Phys. Rev. Lett.*, vol. 108, p. 155501, 2012.

[24] A. Fleurence, "A. fleurence, r. friedlein, t. ozaki, h. kawai, y. wang, and y. yamada-takamura, phys. rev. lett. 108, 245501 (2012)." *Phys. Rev. Lett.*, vol. 108, p. 245501, 2012.

[25] L. Chen and C.-C. Liu, "L. chen, c.-c. liu, b. feng, x. he, p. cheng, z. ding, s. meng, y. yao, and k. wu, phys. rev. lett. 109, 056804 (2012)." *Phys. Rev. Lett.*, vol. 109, p. 056804, 2012.

[26] C.-L. Lin, R. Arafune, K. Kawahara, N. Tsukahara, E. Minamitani, Y. Kim, N. Takagi, and M. Kawai, "Structure of silicene grown on ag (111)," *Applied Physics Express*, vol. 5, no. 4, p. 045802, 2012.

[27] L. Meng, "L. meng, y. wang, l. zhang, s. du, r. wu, l. li, y. zhang, g. li, h. zhou, wa hofer, and h.-j. gao, nano lett. 13, 685 (2013)." *Nano Lett.*, vol. 13, p. 685, 2013.

[28] M. Xu, T. Liang, M. Shi, and H. Chen, "Graphene-like two-dimensional materials," *Chemical reviews*, vol. 113, no. 5, pp. 3766–3798, 2013.

[29] M. Dávila, L. Xian, S. Cahangirov, A. Rubio, and G. Le Lay, "Germanene: a novel two-dimensional germanium allotrope akin to graphene and silicene," *New Journal of Physics*, vol. 16, no. 9, p. 095002, 2014.

[30] L. Li, S. Lu, J. Pan, and Z. Qin, "L. li, s.-z. lu, j. pan, z. qin, y.-q. wang, y. wang, g.-y. cao, s. du, and h.-j. gao, adv. mater. 26, 4820 (2014)." *Adv. Mater.*, vol. 26, p. 4820, 2014.

[31] C.-C. Liu, "C.-c. liu, w. feng, and y. yao, phys. rev. lett. 107, 076802 (2011)." *Phys. Rev. Lett.*, vol. 107, p. 076802, 2011.

[32] C.-C. Liu, H. Jiang, and Y. Yao, "Low-energy effective hamiltonian involving spin-orbit coupling in silicene and two-dimensional germanium and tin," *Physical Review B*, vol. 84, no. 19, p. 195430, 2011.

[33] M. Gmitra, "M. gmitra, s. konschuh, c. ertler, c. ambrosch-draxl, and j. fabian, phys. rev. b 80, 235431 (2009)." *Phys. Rev. B*, vol. 80, p. 235431, 2009.

[34] M. Ezawa, "A topological insulator and helical zero mode in silicene under an inhomogeneous electric field," *New Journal of Physics*, vol. 14, no. 3, p. 033003, 2012.

[35] P. Hewageegana, "Theory of electronic and optical properties of nanostructures," 2008.

[36] K. v. Klitzing, G. Dorda, and M. Pepper, "New method for high-accuracy determination of the fine-structure constant based on quantized hall resistance," *Physical Review Letters*, vol. 45, no. 6, p. 494, 1980.

[37] D. J. Thouless, M. Kohmoto, M. P. Nightingale, and M. den Nijs, "Quantized hall conductance in a two-dimensional periodic potential," *Physical Review Letters*, vol. 49, no. 6, p. 405, 1982.

[38] M. Z. Hasan and C. L. Kane, "Colloquium: topological insulators," *Reviews of Modern Physics*, vol. 82, no. 4, p. 3045, 2010.

[39] B. A. Bernevig, "Ba bernevig, tl hughes, and s.-c. zhang, science 314, 1757 (2006)." *Science*, vol. 314, p. 1757, 2006.

[40] M. König, S. Wiedmann, C. Brüne, A. Roth, H. Buhmann, L. W. Molenkamp, X.-L. Qi, and S.-C. Zhang, "Quantum spin hall insulator state in hgte quantum wells," *Science*, vol. 318, no. 5851, pp. 766–770, 2007.

[41] N. Nagaosa, "A new state of quantum matter," *Science*, vol. 318, no. 5851, pp. 758–759, 2007.

[42] C. L. Kane and E. J. Mele, "Physics. a new spin on the insulating state," *Science (New York, NY)*, vol. 314, no. 5806, pp. 1692–3, 2006.

[43] M. König, "M. könig, s. wiedmann, c. brüne, a. roth, h. buhmann, lw molenkamp, x.-l. qi, and s.-c. zhang, science 318, 766 (2007)." *Science*, vol. 318, p. 766, 2007.

[44] P. Roushan and J. Seo, "P. roushan, j. seo, cv parker, ys hor, d. hsieh, d. qian, a. richardella, mz hasan, rj cava, and a. yazdani, nature (london) 460, 1106 (2009)." *Nature (London)*, vol. 460, p. 1106, 2009.

[45] Z. Alpichshev, "Z. alpichshev, jg analytis, j.-h. chu, ir fisher, yl chen, zx shen, a. fang, and a. kapitulnik, phys. rev. lett. 104, 016401 (2010)." *Phys. Rev. Lett.*, vol. 104, p. 016401, 2010.

[46] J. Chen, X. He, K. Wu, Z. Ji, L. Lu, J. Shi, J. Smet, and Y. Li, "Tunable surface conductivity in bi 2 se 3 revealed in diffusive electron transport," *Physical Review B*, vol. 83, no. 24, p. 241304, 2011.

[47] A. Taskin and Y. Ando, "Quantum oscillations in a topological insulator bi 1- x sb x," *Physical Review B*, vol. 80, no. 8, p. 085303, 2009.

[48] H. Peng, K. Lai, D. Kong, S. Meister, Y. Chen, X.-L. Qi, S.-C. Zhang, Z.-X. Shen, and Y. Cui, "Aharonov–bohm interference in topological insulator nanoribbons," *Nature materials*, vol. 9, no. 3, p. 225, 2010.

[49] T. Hanaguri, K. Igarashi, M. Kawamura, H. Takagi, and T. Sasagawa, "Momentum-resolved landau-level spectroscopy of dirac surface state in bi 2 se 3," *Physical Review B*, vol. 82, no. 8, p. 081305, 2010.

[50] P. Cheng, C. Song, T. Zhang, Y. Zhang, Y. Wang, J.-F. Jia, J. Wang, Y. Wang, B.-F. Zhu, X. Chen *et al.*, "Landau quantization of topological surface states in bi 2 se 3," *Physical Review Letters*, vol. 105, no. 7, p. 076801, 2010.

[51] S. A. O. Motlagh, J.-S. Wu, V. Apalkov, and M. I. Stockman, "Fundamentally fastest optical processes at the surface of a topological insulator," *Physical Review B*, vol. 98, no. 12, p. 125410, 2018.

[52] S. A. O. Motlagh, V. Apalkov, and M. I. Stockman, "Interaction of crystalline topological insulator with an ultrashort laser pulse," *Physical Review B*, vol. 95, no. 8, p. 085438, 2017.

[53] C. Brüne and C. Liu, "C. brüne, cx liu, eg novik, em hankiewicz, h. buhmann, yl chen, xl qi, zx shen, sc zhang, and lw molenkamp, phys. rev. lett. 106, 126803 (2011)." *Phys. Rev. Lett.*, vol. 106, p. 126803, 2011.

[54] D. Abergel, "Dsl abergel, v. apalkov, j. berashevich, k. ziegler, and t. chakraborty, adv. phys. 59, 261 (2010)." *Adv. Phys.*, vol. 59, p. 261, 2010.

[55] Z. Yang and J. H. Han, "Landau level states on a topological insulator thin film," *Physical Review B*, vol. 83, no. 4, p. 045415, 2011.

[56] V. M. Apalkov and T. Chakraborty, "Interacting dirac fermions on a topological insulator in a magnetic field," *Physical review letters*, vol. 107, no. 18, p. 186801, 2011.

[57] H. Zhang, C.-X. Liu, X.-L. Qi, X. Dai, Z. Fang, and S.-C. Zhang, "Topological insulators in bi 2 se 3, bi 2 te 3 and sb 2 te 3 with a single dirac cone on the surface," *Nature physics*, vol. 5, no. 6, p. 438, 2009.

[58] C.-X. Liu, X.-L. Qi, H. Zhang, X. Dai, Z. Fang, and S.-C. Zhang, "Model hamiltonian for topological insulators," *Physical Review B*, vol. 82, no. 4, p. 045122, 2010.

[59] S.-Q. Shen, *Topological insulators*. Springer, 2012, vol. 174.

[60] M. Houssa, A. Dimoulas, and A. Molle, "Silicene: a review of recent experimental and theoretical investigations," *Journal of Physics: Condensed Matter*, vol. 27, no. 25, p. 253002, 2015.

[61] C.-C. Liu, W. Feng, and Y. Yao, "Quantum spin hall effect in silicene and two-dimensional germanium," *Physical review letters*, vol. 107, no. 7, p. 076802, 2011.

[62] A. Acun, L. Zhang, P. Bampoulis, M. Farmanbar, A. van Houselt, A. Rudenko, M. Lingenfelder, G. Brocks, B. Poelsema, M. Katsnelson *et al.*, "Germanene: the germanium analogue of graphene," *Journal of physics: Condensed matter*, vol. 27, no. 44, p. 443002, 2015.

[63] J.-W. Jiang and H. S. Park, "Mechanical properties of single-layer black phosphorus," *Journal of Physics D: Applied Physics*, vol. 47, no. 38, p. 385304, 2014.

[64] G. Qin, Q.-B. Yan, Z. Qin, S.-Y. Yue, M. Hu, and G. Su, "Anisotropic intrinsic lattice thermal conductivity of phosphorene from first principles," *Physical Chemistry Chemical Physics*, vol. 17, no. 7, pp. 4854–4858, 2015.

[65] L. Li, Y. Yu, G. J. Ye, Q. Ge, X. Ou, H. Wu, D. Feng, X. H. Chen, and Y. Zhang, "Black phosphorus field-effect transistors," *Nature nanotechnology*, vol. 9, no. 5, p. 372, 2014.

[66] X. Zhang, H. Xie, Z. Liu, C. Tan, Z. Luo, H. Li, J. Lin, L. Sun, W. Chen, Z. Xu *et al.*, "Black phosphorus quantum dots," *Angewandte chemie international edition*, vol. 54, no. 12, pp. 3653–3657, 2015.

[67] H. Liu, A. T. Neal, Z. Zhu, Z. Luo, X. Xu, D. Tománek, and P. D. Ye, "Phosphorene: an unexplored 2d semiconductor with a high hole mobility," *ACS nano*, vol. 8, no. 4, pp. 4033–4041, 2014.

[68] F. Nematollahi, V. Apalkov, and M. I. Stockman, "Phosphorene in ultrafast laser field," *Physical Review B*, vol. 97, no. 3, p. 035407, 2018.

[69] A. Rodin, A. Carvalho, and A. C. Neto, "Strain-induced gap modification in black phosphorus," *Physical review letters*, vol. 112, no. 17, p. 176801, 2014.

[70] H. Du, X. Lin, Z. Xu, and D. Chu, "Recent developments in black phosphorus transistors," *Journal of Materials Chemistry C*, vol. 3, no. 34, pp. 8760–8775, 2015.

[71] V. Tran, R. Soklaski, Y. Liang, and L. Yang, "Layer-controlled band gap and anisotropic excitons in few-layer black phosphorus," *Physical Review B*, vol. 89, no. 23, p. 235319, 2014.

[72] T. Low, R. Roldán, H. Wang, F. Xia, P. Avouris, L. M. Moreno, and F. Guinea, "Plasmons and screening in monolayer and multilayer black phosphorus," *Physical review letters*, vol. 113, no. 10, p. 106802, 2014.

[73] R. R. Biswas and A. V. Balatsky, "Scattering from surface step edges in strong topological insulators," *Physical Review B*, vol. 83, no. 7, p. 075439, 2011.

[74] D. Zhang and C. Ting, "Impact of step defects on surface states of topological insulators," *Physical Review B*, vol. 85, no. 11, p. 115434, 2012.

[75] K. Kobayashi, "Electron transmission through atomic steps of bi 2 se 3 and bi 2 te 3 surfaces," *Physical Review B*, vol. 84, no. 20, p. 205424, 2011.

[76] P. Rakyta, A. Pályi, and J. Cserti, "Electronic standing waves on the surface of the topological insulator bi 2 te 3," *Physical Review B*, vol. 86, no. 8, p. 085456, 2012.

[77] J. An and C. Ting, "Surface states scattering from a step defect in the topological insulator bi 2 te 3," *Physical Review B*, vol. 86, no. 16, p. 165313, 2012.

[78] M. Governale, "Quantum dots with rashba spin-orbit coupling," *Physical review letters*, vol. 89, no. 20, p. 206802, 2002.

[79] P. Lucignano, B. Jouault, and A. Tagliacozzo, "Spin exciton in a quantum dot with spin-orbit coupling at high magnetic field," *Physical Review B*, vol. 69, no. 4, p. 045314, 2004.

[80] J. Lee, Z. M. Wang, E. Kim, N. Kim, S. Park, and G. Salamo, "Various quantum-and nano-structures by iii–v droplet epitaxy on gaas substrates," *Nanoscale research letters*, vol. 5, no. 2, p. 308, 2010.

APPENDIX

APPENDIX

Mathematica code for evaluating reflectance in Chapter 2

```
Clear[A2, B1, B2, D1, D2, F1, F11, F2, F21, N1, N2, M, M1, k, k1, kx, kx1, ky, En, λ, λ1, λb, λb1, L1, L2, c1, φ, r]

p0 := -I * A2 (kx - I * ky) * (λb - I * kx)
p1 := (λb + I * kx) * (-I * A2 (-kx - I * ky))
p3 := (λb - I * kx1) * (-I * A2 (kx1 - I * ky))
p4 := (λb + λb1) * (-I * A2 (I λb1 - I * ky))

s0 := (F1 + N1 (k^2) - En) * (λb - I * kx)
s1 := (λb + I * kx) * (F1 + N1 (k^2) - En)
s3 := (λb - I * kx1) * (F11 + N1 (k1^2) - En)
s4 := (λb + λb1) * (F11 - N1 (λ1^2) - En)

f0 := I kx ((-I * A2 (kx - I * ky)) * (F1 - N1 (λ^2) - En) - (F1 + N1 (k^2) - En) * (-I * A2 (-I λb - I * ky)))
f1 := -I kx ((-I * A2 (-kx - I * ky)) * (F1 - N1 (λ^2) - En) - (F1 + N1 (k^2) - En) * (-I * A2 (-I λb - I * ky)))
f3 := I kx1 ((-I * A2 (kx1 - I * ky)) * (F1 - N1 (λ^2) - En) - (F11 + N1 (k1^2) - En) * (-I * A2 (-I λb - I * ky)))
f4 := -λb1 ((-I * A2 (I λb1 - I * ky)) * (F1 - N1 (λ^2) - En) - (F11 - N1 (λ1^2) - En) * (-I * A2 (-I λb - I * ky)))


c1 =
 Function[{p0, p1, p3, p4, s0, s1, s3, s4, f0, f1, f3, f4},
   {{{{(p0 * f4) - (f0 * p4)) ((s3 * f4) - (f3 * s4))) - ((s0 * f4) - (f0 * s4)) ((p3 * f4) - (f3 * p4))) /
      (((s1 * f4) - (f1 * s4)) ((p3 * f4) - (f3 * p4)) - ((p1 * f4) - (f1 * p4)) ((s3 * f4) - (f3 * s4)))}][
  (-I * A2 (kx - I * ky) * (λb - I * kx)), (λb + I * kx) * (-I * A2 (-kx - I * ky)), (λb - I * kx1) * (-I * A2 (kx1 - I * ky)),
  (λb + λb1) * (-I * A2 (I λb1 - I * ky)), (F1 + N1 (k^2) - En) * (λb - I * kx), (λb + I * kx) * (F1 + N1 (k^2) - En),
  (λb - I * kx1) * (F11 + N1 (k1^2) - En), (λb + λb1) * (F11 - N1 (λ1^2) - En),
  I kx ((-I * A2 (kx - I * ky)) * (F1 - N1 (λ^2) - En) - (F1 + N1 (k^2) - En) * (-I * A2 (-I λb - I * ky))),
  -I kx ((-I * A2 (-kx - I * ky)) * (F1 - N1 (λ^2) - En) - (F1 + N1 (k^2) - En) * (-I * A2 (-I λb - I * ky))),
  I kx1 ((-I * A2 (kx1 - I * ky)) * (F1 - N1 (λ^2) - En) - (F11 + N1 (k1^2) - En) * (-I * A2 (-I λb - I * ky))),
  -λb1 ((-I * A2 (I λb1 - I * ky)) * (F1 - N1 (λ^2) - En) - (F11 - N1 (λ1^2) - En) * (-I * A2 (-I λb - I * ky)))]


A2 := 4.1
B1 := 10
B2 := 56.6
D1 := 1.3
D2 := 19.6
M := 0.28
M1 := 0.28

L1 = 40
φ = 0

k = {0.01, 0.02, .04, .06, .08, .1}
En = (D1 * Pi^2 / L1^2) + (D2 * k^2) + Sqrt[((B1 * Pi^2 / L1^2) + (B2 * k^2))^2 + A2^2 * k^2]


F1 := (D1 + B1) * (Pi^2) / L1^2
F11 := (D1 + B1) * (Pi^2) / L2^2
F2 := (D1 - B1) * (Pi^2) / L1^2
F21 := (D1 - B1) * (Pi^2) / L2^2
N1 := D2 + B2
N2 := D2 - B2
α := (D2^2) - (B2^2)
α1 := (D2^2) - (B2^2)
β := (2 Pi^2 / L1^2) (D1 D2 - B1 B2) - (2 En D2) - (A2^2)
β1 := (2 Pi^2 / L2^2) (D1 D2 - B1 B2) - (2 En D2) - (A2^2)
γ := En (En - (2 D1 Pi^2 / L1^2)) + F1 F2
γ1 := En (En - (2 D1 Pi^2 / L2^2)) + F11 * F21


ky = k * Sin[φ]
λ = -I * Sqrt[(-β + Sqrt[(β^2) - 4 α γ]) / (2 α)]
λ1 = -I * Sqrt[(-β1 + Sqrt[(β1^2) - 4 α1 γ1]) / (2 α1)]
λb = -I * Sqrt[-λ^2 - ky^2]
λb1 = -I * Sqrt[-λ1^2 - ky^2]
ko = Sqrt[(-β - Sqrt[(β^2) - 4 α γ]) / (2 α)]
k1 = Sqrt[(-β1 - Sqrt[(β1^2) - 4 α1 γ1]) / (2 α1)]
kx = k * Cos[φ]
kx1 = Sqrt[k1^2 - ky^2]
```

Mathematica code to evaluate charge density in Chapter 3

```
Clear[F1, F2, E1, L1, L2, β, φ, γ, κ0, κ01, q, q1, q2, M1, M2, P1, P2, m, R, ρ, a1, a2, a3, b1, b2, b3, c1, c2, c3,
 d1, d2, d3, p1, p2, p3, p4, Rρ, Rρ1, N, N1]

(*All in A and eV*)
L1 = 40; L2 = 20; A2 = 4.1; D1 = 1.3; B1 = 10; D2 = 19.6; B2 = 56.6; N1 = D2 + B2; N2 = D2 - B2; A21 = 4.1;
F1 = D1 π^2 / L^2 + B1 π^2 / L^2;
F11 = F1 /. L → L2;
F2 = D1 π^2 / L^2 - B1 π^2 / L^2;
α = D2^2 - B2^2;
β = (2 π^2 / L^2 (D1 D2 - B1 B2) - 2 E1 D2 - A2^2) / α;
γ = (E1 (E1 - 2 D1 π^2 / L^2) + F1 F2) / α;
φ = π / 180 × (0); (* input angle in deg*)

κp2 = (-β + √(β^2 - 4 γ)) / 2;
κm2 = (-β - √(β^2 - 4 γ)) / 2;
κ0 = √(κp2 /. L → L1);
κ01 = √(-κp2 /. L → L1);
q = √(-κm2 /. L → L1);
q1 = √(-κp2 /. L → L2);

q2 = √(-κm2 /. L → L2);

(*----------Electron density R(ρ) :---------- *)
Rρ = N^2 (p1 * Q1 * BesselJ[m, κ0 * ρ] + p2 * l1 * BesselI[m, q * ρ])^2 + N^2 (p1 * Q2 BesselJ[m + 1, κ0 * ρ] + p2 * l2 * BesselI[m + 1, q * ρ])^2;
(*ρ<R*)

Rρ1 = N^2 (p3 * A1 * BesselK[m, q1 * ρ] + p4 * β1 * BesselK[m, q2 * ρ])^2 + N^2 (p3 * A2 * BesselK[m + 1, q1 * ρ] + p4 * β2 * BesselK[m + 1, q2 * ρ])^2;
(*ρ>R*)



p1 = -(-b3 c2 d1 + b2 c3 d1 + a3 c2 d2 - a2 c3 d2 - a3 b2 d3 + a2 b3 d3) / (a3 b2 c1 - a2 b3 c1 - a3 b1 c2 + a1 b3 c2 + a2 b1 c3 - a1 b2 c3);
p2 = -(b3 c1 d1 - b1 c3 d1 - a3 c1 d2 + a1 c3 d2 + a3 b1 d3 - a1 b3 d3) / (a3 b2 c1 - a2 b3 c1 - a3 b1 c2 + a1 b3 c2 + a2 b1 c3 - a1 b2 c3);
p3 = -(-b2 c1 d1 + b1 c2 d1 + a2 c1 d2 - a1 c2 d2 - a2 b1 d3 + a1 b2 d3) / (a3 b2 c1 - a2 b3 c1 - a3 b1 c2 + a1 b3 c2 + a2 b1 c3 - a1 b2 c3);
p4 = 1;


a1 = κ0 BesselJ[m, κ0 R];
a2 = q BesselI[m, q R];
a3 = q1 BesselK[m, q1 R];

b1 = ((F1 /. L → L1) - E1 + N1 κ0^2) BesselJ[m + 1, κ0 R];
b2 = ((F1 /. L → L1) - E1 - N1 q^2) BesselI[m + 1, q R];
b3 = -(F11 - E1 - N1 q1^2) BesselK[m + 1, q1 R];

c1 = κ0^2 BesselJ[m + 1, κ0 R];
c2 = -q^2 BesselI[m + 1, q R];
c3 = q1^2 BesselK[m + 1, q1 R];

d1 = -q2 BesselK[m, q2 R];
d2 = (F11 - E1 - N1 q2^2) BesselK[m + 1, q2 R];
d3 = -q2^2 BesselK[m + 1, q2 R];
```

```
(*------------Normalization constant---------------*)

N = Sqrt[ 1 / (2 Pi N1) ]; (* 1/(N^2 2 Pi) = N1 *)

N1 = (p1^2 * Q1^2 * SJJ[m, κ0]) + (2 * p1 * Q1 * p2 * l1 * SJI[m, κ0, q]) + (p2^2 * l1^2 * SII[m, q]) + (p1^2 * Q2^2 * SJJ[m + 1, κ0]) +
    (2 * p1 * p2 * Q2 * l2 * SJI[m + 1, κ0, q]) + (p2^2 * l2^2 * SII[m + 1, q]) + (p3^2 * Λ1^2 * SKK[m, q1]) + (2 * p3 * p4 * Λ1 * β1 * SKKab[m, q1, q2]) +
    (p4^2 * β1^2 * SKK[m, q2]) + (p3^2 * Λ2^2 * SKK[m + 1, q1]) + (2 * p3 * p4 * Λ2 * β2 * SKKab[m + 1, q1, q2]) + (p4^2 * β2^2 * SKK[m + 1, q2]);


Q1 = -A2 κ0;
Q2 = (F1 /. L → L1) - E1 + N1 κ0^2;

l1 = -A2 q;
l2 = (F1 /. L → L1) - E1 - N1 q^2;

Λ1 = A2 q1;
Λ2 = F11 - E1 - N1 q1^2;

β1 = A2 q2;
β2 = F11 - E1 - N1 q2^2;


(*----------Defining the notations----------------*)

SJJ[m_, a_] := 1/2 R^2 (BesselJ[m, a R]^2 - BesselJ[-1 + m, a R] BesselJ[m + 1, a R])

SJJab[m_, a_, b_] := 1/(b^2 - a^2) (a R BesselJ[m, b R] BesselJ[m - 1, a R] - b R BesselJ[m - 1, b R] BesselJ[m, a R])

SJI[m_, a_, b_] := 1/(b^2 + a^2) (-a R BesselI[m, b R] BesselJ[m - 1, a R] + b R BesselI[m - 1, b R] BesselJ[m, a R])

SII[m_, a_] := 1/2 R^2 (BesselI[m, a R]^2 - BesselI[m - 1, a R] BesselI[m + 1, a R])

SIIab[m_, a_, b_] := 1/(b^2 - a^2) (-a R BesselI[m, b R] BesselI[m - 1, a R] + b R BesselI[m - 1, b R] BesselI[m, a R])

SKK[m_, a_] := -1/2 R^2 (BesselK[m, a R]^2 - BesselK[m - 1, a R] BesselK[m + 1, a R])

SKKab[m_, a_, b_] := -1/(a^2 - b^2) (b R BesselK[m, a R] BesselK[m - 1, b R] - a R BesselK[m - 1, a R] BesselK[m, b R])

SJJ[m, κ0];
SJI[m, κ0, q];
SII[m, q];

SJJ[m + 1, κ0];
SJI[m + 1, κ0, q];
SII[m + 1, q];
```

Mathematica code to evaluate energies in Chapter 4

```
Clear[λso, Ez, Ezi, Ezo, En, v , κ, a, λ, l, a1, a2, a3, b1, b2, b3, g1, g2, g3, h1, h2, h3, m]

M1 = {{-λso + l Ez - En , I v κ, a λ κ, 0}, {-I v κ, λso - l Ez - En , 0, -a λ κ}, {a λ κ, 0, λso + l Ez - En, I v κ},
   {0, -a λ κ, -I v κ, -(λso + l Ez + En)}};
MatrixForm[M1];
(*λso= λ spin orbit
   λ =λR Rashba spin orbit coupling
    En= Energy
     Ez= Electric field perpendicular to the plane
      v= Fermi velocity
       l= separated distance of two sublattice planes
        a= lattice constant
*)
Det[M1];
(*En^4-2 En^2 Ez^2 l^2+Ez^4 l^4-2 En^2 v^2 κ^2+2 Ez^2 l^2 v^2 κ^2+v^4 κ^4-2 a^2 En^2 κ^2 λ^2-2 a^2 Ez^2 l^2 κ^2 λ^2+2 a^2 v^2 κ^4 λ^2+a^4 κ^4 λ^4-
 2 En^2 λso^2-2 Ez^2 l^2 λso^2+2 v^2 κ^2 λso^2+2 a^2 κ^2 λ^2 λso^2+λso^4 *)
κ4i = Solve[Det[M1] == 0, κ][[1]] /. {Ez -> Ezi};
κ3i = Solve[Det[M1] == 0, κ][[2]] /. Ez -> Ezi;
κ2i = Solve[Det[M1] == 0, κ][[3]] /. Ez -> Ezi;
κ1i = Solve[Det[M1] == 0, κ][[4]] /. Ez -> Ezi;

κ1i =
  √((En^2 v^2)/(v^4 + 2 a^2 v^2 λ^2 + a^4 λ^4) - (Ezi^2 l^2 v^2)/(v^4 + 2 a^2 v^2 λ^2 + a^4 λ^4) + (a^2 En^2 λ^2)/(v^4 + 2 a^2 v^2 λ^2 + a^4 λ^4) + (a^2 Ezi^2 l^2 λ^2)/(v^4 + 2 a^2 v^2 λ^2 + a^4 λ^4) - (v^2 λso^2)/(v^4 + 2 a^2 v^2 λ^2 + a^4 λ^4) -
    (a^2 λ^2 λso^2)/(v^4 + 2 a^2 v^2 λ^2 + a^4 λ^4) + (2 √(a^2 En^2 Ezi^2 l^2 v^2 λ^2 - a^2 Ezi^4 l^4 v^2 λ^2 + a^4 En^2 Ezi^2 l^2 λ^4 + Ezi^2 l^2 v^4 λso^2 + a^2 Ezi^2 l^2 v^2 λ^2 λso^2)) /
     (v^4 + 2 a^2 v^2 λ^2 + a^4 λ^4)) ;(*Real*)

κ3i =
  √((En^2 v^2)/(v^4 + 2 a^2 v^2 λ^2 + a^4 λ^4) - (Ezi^2 l^2 v^2)/(v^4 + 2 a^2 v^2 λ^2 + a^4 λ^4) + (a^2 En^2 λ^2)/(v^4 + 2 a^2 v^2 λ^2 + a^4 λ^4) + (a^2 Ezi^2 l^2 λ^2)/(v^4 + 2 a^2 v^2 λ^2 + a^4 λ^4) - (v^2 λso^2)/(v^4 + 2 a^2 v^2 λ^2 + a^4 λ^4) -
    (a^2 λ^2 λso^2)/(v^4 + 2 a^2 v^2 λ^2 + a^4 λ^4) - (2 √(a^2 En^2 Ezi^2 l^2 v^2 λ^2 - a^2 Ezi^4 l^4 v^2 λ^2 + a^4 En^2 Ezi^2 l^2 λ^4 + Ezi^2 l^2 v^4 λso^2 + a^2 Ezi^2 l^2 v^2 λ^2 λso^2)) /
     (v^4 + 2 a^2 v^2 λ^2 + a^4 λ^4)) ;(*Imaginary*)


κ4o = Solve[Det[M1] == 0, κ][[1]] /. {Ez -> Ezo};
κ3o = Solve[Det[M1] == 0, κ][[2]] /. Ez -> Ezo;
κ2o = Solve[Det[M1] == 0, κ][[3]] /. Ez -> Ezo;
κ1o = Solve[Det[M1] == 0, κ][[4]] /. Ez -> Ezo;

κ1o =
  √((En^2 v^2)/(v^4 + 2 a^2 v^2 λ^2 + a^4 λ^4) - (Ezo^2 l^2 v^2)/(v^4 + 2 a^2 v^2 λ^2 + a^4 λ^4) + (a^2 En^2 λ^2)/(v^4 + 2 a^2 v^2 λ^2 + a^4 λ^4) + (a^2 Ezo^2 l^2 λ^2)/(v^4 + 2 a^2 v^2 λ^2 + a^4 λ^4) - (v^2 λso^2)/(v^4 + 2 a^2 v^2 λ^2 + a^4 λ^4) -
    (a^2 λ^2 λso^2)/(v^4 + 2 a^2 v^2 λ^2 + a^4 λ^4) + (2 √(a^2 En^2 Ezo^2 l^2 v^2 λ^2 - a^2 Ezo^4 l^4 v^2 λ^2 + a^4 En^2 Ezo^2 l^2 λ^4 + Ezo^2 l^2 v^4 λso^2 + a^2 Ezo^2 l^2 v^2 λ^2 λso^2)) /
     (v^4 + 2 a^2 v^2 λ^2 + a^4 λ^4)) ;(*Imaginary*)
```

```
κ3o =
 √( En^2 v^2/(v^4 + 2 a^2 v^2 λ^2 + a^4 λ^4) - Ezo^2 l^2 v^2/(v^4 + 2 a^2 v^2 λ^2 + a^4 λ^4) + a^2 En^2 λ^2/(v^4 + 2 a^2 v^2 λ^2 + a^4 λ^4) + a^2 Ezo^2 l^2 λ^2/(v^4 + 2 a^2 v^2 λ^2 + a^4 λ^4) - v^2 λso^2/(v^4 + 2 a^2 v^2 λ^2 + a^4 λ^4) -
    a^2 λ^2 λso^2/(v^4 + 2 a^2 v^2 λ^2 + a^4 λ^4) - (2 √(a^2 En^2 Ezo^2 l^2 v^2 λ^2 - a^2 Ezo^4 l^4 v^2 λ^2 + a^4 En^2 Ezo^2 l^2 λ^4 + Ezo^2 l^2 v^4 λso^2 + a^2 Ezo^2 l^2 v^2 λ^2 λso^2)) /
     (v^4 + 2 a^2 v^2 λ^2 + a^4 λ^4) ); (*Imaginary*)

a1 = (-En + Ez l - λso);
a2 = I v κ;
a3 = a κ λ ;
b1 = -I v κ;
b2 = (-Ez l + λso - En);
b3 = -a κ λ;
g1 = a κ λ;
g2 = (Ez l + λso - En);
g3 = I v κ;
h1 = -a κ λ ;
h2 = -I v κ;
h3 = (-Ez l - λso - En);


(*Germanene*)
l = 0.33; (*Å*)
a = 4.13; (*Å*)
t = 1.3*10^3; (*meV*)
v = (√3 / 2) * a * t;(* meVA,Fermi velocity*)

I
c1 = -(a2 b3 g2) + (a3 b2 g3) / (a3 b2 g1) + (a2 b1 g2) - (a1 b2 g2);
c2 = -(a3 b3 g1) - (a1 b3 g2) - (a3 b1 g3) / (a3 b2 g1) + (a2 b1 g2) - (a1 b2 g2);
c3 = -(a2 b3 g1) - (a2 b1 g3) + (a1 b2 g3) / (-a3 b2 g1) - (a2 b1 g2) + (a1 b2 g2);
c4 = 1;
```